MAX-PLANCK-INSTITUT FÜR METEOROLOGIE

UMWELTFORSCHUNGSPLAN

DES BUNDESMINISTERS DES INNEREN

ENTWICKLUNG VON KLIMAMODELLEN

FORSCHUNGSBERICHT 104 02 612

EIN MODELL DER OZEANISCHEN ZIRKULATION ZUR UNTERSUCHUNG VON KLIMASCHWANKUNGEN

BAND 2

IM AUFTRAG

DES UMWELTBUNDESAMTES

SEPTEMBER 1982

MAX-PLANCK-INSTITUT FÜR METEOROLOGIE

An ocean circulation model for climate variability studies

E. Maier-Reimer
D. Müller
D. Olbers
J. Willebrand
K. Hasselmann

Max-Planck-Institut für Meteorologie, Hamburg

Status report

September 1982

Contents

1. Introduction

Numerical ocean circulation models have been designed traditionally to study the mean steady state ocean circulation. The model presented in this report is designed for the more general problem of investigating the global response of the ocean to variable forcing over a wide range of space and time scales relevant for climate studies. In contrast to the mean circulation problem, for which a single numerical simulation with an appropriately tuned model can be sufficient for many purposes, the application of an ocean circulation model in systematic climate studies requires an extensive sequence of response experiments. Computational efficiency of the model is therefore a prime concern.

The present model is more than one order of magnitude faster than traditional circulation models based on the primitive equations. This is achieved by filtering out fast gravity modes, which are irrelevant for climate response studies on time modes longer than about a month, and by simplifying the remaining equations for the barotropic and baroclinic Rossby modes. Since the barotropic response time of the ocean is generally small compared with climatic time scales of interest, the barotropic component of the ocean circulation can be treated in the asymptotic two time-scale limit as the steady-state equilibrium response to the instantaneous forcing field. The baroclinic equations can be simplified by noting that, away from the equator, the resolvable space modes are large compared with the baroclinic Rossby radius of deformation. This implies that the baroclinic velocity field can be regarded as geostrophic, and the baroclinic quasi-geostrophic vorticity equation reduces to the prognostic equations for the salinity and temperature fields, which are simply advected by the geostrophic currents.

These approximations break down near the equator, the western and eastern boundaries, along the sea ice margin, and in the upper seasonal layer of the ocean. Ultimately, a global ocean circulation model is planned in which these dynamically and climatically important special regions are modelled separately and together and coupled to the interior geostrophic regime through appropriate, mutually matching boundary conditions. The present report

describes only the interior ocean model and preliminary tests with the seasonal layer model. Tests with a coupled interior ocean and seasonal layer model have not yet been carried out, and models for the equatorial, coastal boundary and sea-ice margins are still in the process of development. Nevertheless, it is felt that the global interior ocean circulation model in itself already incorporates many of the important features of the role of the oceans in climate dynamics, and that several preliminary experiments with this preliminary version of the model could therefore be usefully carried out. The lacking non-linear regional models are replaced in the preliminary model by linear frictional regimes. In this respect the model is similar to earlier strongly frictional global circulation models based on the primitive equations, and the general features of the mean circulation obtained with the present more efficient model also resembles the earlier model results (cf. Section 5). The geographical distribution and bathymetry of the world oceans ar fully included in the model, within the limitation of the prese 500 km resolution (the vertical structure is described by five layers). Included in the model is a tracer advection scheme. Apart from investigating the distribution of tracers (Tritium, C^{14}) it is intended to apply these calculations to study the storage of CO_2 in the oceans.

Detailed experiments are not presented; the purpose of this report is to document the basic philosophy and present status of the model.

2. The model for the interior ocean

In this section, we briefly report the derivation of the filtered model equations. Further details are given by Hasselmann (1982).

We assume that for global climatic studies the time and horizontal space resolution of the ocean model may be limited in the interior ocean, away from lateral boundaries and excluding a narrow equatorial strip, to 1 month and 500 km, respectively. The one month time resolution corresponds to the generally accepted definition of the lower time scale limit of climatic variability. The spatial resolution of 500 km may be related through the time resolution to a maximum advection velocity of 500 km/month ≈ 20 cm/sec. The rather arbitrary choice of 500 km is not critical. We shall require in the following mainly that the spatial resolution is large compared with the internal Rossby deformation radius, which is typically of the order of 50 km.

Under these conditions, the full equations for the ocean can be strongly simplified. Applying the usual hydrostatic and Boussinesque approximations, the complete set of prognostic equations are given by

$$\partial_t \underline{u} - f \underline{u}^{\perp} + \underline{\nabla} p = \underline{q} \qquad (2.1)$$

$$\partial_t \zeta - w_0 = q_\zeta \approx 0 \qquad (2.2)$$

$$\partial_t \begin{Bmatrix} T \\ S \end{Bmatrix} + \left[\underline{u} \underline{\nabla} + w \partial_z \right] \begin{Bmatrix} T \\ S \end{Bmatrix} = \begin{Bmatrix} q_T \\ q_S \end{Bmatrix} \qquad (2.3)$$

where the horizontal velocity $\underline{u} = (u,v)$, surface elevation salinity S and temperature T define the components of the basic system state vector $\underset{\sim}{\psi} = (\underline{u}, \zeta, T, S)$.

$\underline{u}_\perp = (v,-u) = R\underline{u}$ represents the vector $\underline{u}$ after applying a 90^o right rotation R (the notation $\underline{a}_\perp = R\underline{a}$ will be used generally for a rotation R of any horizontal vector $\underline{a}$),

f is the (latitude dependent) Coriolis parameter,

$\underline{\nabla} = \left\{(a\cos\theta)^{-1}\frac{\partial}{\partial\lambda}, a^{-1}\frac{\partial}{\partial\theta}\right\}$ is the gradient operator in spherical coordinates (λ = longitude, θ = latidude, a = radius of earth) - we note that the contravariant gradient operator must be distinguished from the covariant divergence operator,

$\underline{\nabla} = \left\{(a\cos\theta)^{-1}\frac{\partial}{\partial\lambda}, (a\cos\theta)^{-1}\frac{\partial}{\partial\theta}\cos\theta\right\}$, appearing later in equation (2.5) -

w is the vertical velocity, with w_o the value of w at the surface $z = \zeta$,

z is the vertical coordinate, taken positive upwards, and

p is the kinematic pressure, defined in terms of a constant reference density $\tilde{\rho}_o$ and pressure deviation $\tilde{p}_1$ as

$$p = \tilde{p}_1 / \tilde{\rho}_o$$

where the total pressure $\tilde{p} = \tilde{p}_o + \tilde{p}_1$ is represented as the sum of the hydrostatic reference pressure $p_o = g\rho_o z$ and the pressure deviation $\tilde{p}_1$.

For the large horizontal scales of interest here, p can be determined hydrostatically from the anomaly $\tilde{\rho}_1$ of the density field $\tilde{\rho} = \tilde{\rho}_o + \tilde{\rho}_1$ relative to the reference density $\tilde{\rho}_o$

$$p = g\zeta + g\int_z^0 \rho\, dz \qquad (2.4)$$

where $\rho = \tilde{\rho}_1 / \tilde{\rho}_o$.

The forcing terms on the right-hand side of equations (2.1) and (2.3) represent the sum of turbulent eddy transport terms and, in the case of eq.(2.1), nonlinear advection (the important advection terms in (2.3) are included explicitly in the left-hand side of the equation). The forcing term on the right-hand side of (2.2) represents the sum of the mass flux due to precipitation or evaporation and the nonlinear slope corrections in the expression for the normal surface velocity. It is generally very small and will be neglected in the following.

The fields w and p represent non-prognostic variables which are related to the components of the state vector $\underset{\sim}{\psi}$ through the diagnostic hydrostatic equation (2.4), the equation of state of sea water, which defines ρ as a function of T, S and z(or, equivalently, the reference pressure $\tilde{p}_o = g\tilde{\rho}_o z$), and the equation of continuity,

$$w = -\underline{\nabla}\int_{-h}^{z} \underline{u}\, dz \qquad (2.5)$$

where h(x,y) denotes the ocean depth.

To close the system of equations, the turbulent mixing terms in the source functions need to be expressed in terms of $\underset{\sim}{\psi}$. Furthermore, boundary conditions must be specified. The choice of parameterization generally affects also the appropriate form of the boundary conditions. These questions will be considered later in this section.

The system of equations (2.1)-(2.5) contains various classes of solutions characterised by different space and time scales. Thus motions coupled to displacements of the free surface are generally associated with significantly shorter time scales

than motions governed only by internal displacements of density surfaces. To separate out these two forms of motion it is customary to divide the system $\underset{\sim}{\varphi}$ into a barotropic subsystem $\hat{\underset{\sim}{\varphi}} = (\hat{\underline{u}}, J)$ and a baroclinic subsystem $\underset{\sim}{\varphi}' = (\underline{u}', T, S)$ where the barotropic velocity

$$\hat{\underline{u}} = \frac{1}{h} \int_{-h}^{0} \underline{u} \, dz \tag{2.6}$$

is defined as the vertically averaged horizontal velocity and the baroclinic velocity as the residual field $\underline{u}' = \underline{u} - \hat{\underline{u}}$.

The associated barotropic and baroclinic components of the vertical velocity

$$w = \hat{w} + w' \tag{2.7}$$

are then defined in terms of the individual continuity relations

$$\begin{Bmatrix} \hat{w} \\ w' \end{Bmatrix} = - \nabla \int_{-h}^{z} \begin{Bmatrix} \hat{\underline{u}} \\ \underline{u}' \end{Bmatrix} dz \tag{2.8}$$

Introducing also barotropic and baroclinic components of the pressure field,

$$p = \hat{p} + p' \tag{2.9}$$

where

$$\hat{p} = g J \tag{2.10}$$

and

$$p' = g \int_{z}^{0} \rho \, dz \tag{2.11}$$

the system of equations (2.1)-(2.3) can be separated into the two (coupled) subsystems:

<u>barotropic system</u>

$$\partial_t \hat{\underline{u}} - f \hat{\underline{u}}^{\perp} + \underline{\nabla} \hat{p} + \frac{1}{h} \int_{-h}^{0} \underline{\nabla} p' \, dz = \hat{\underline{q}} \tag{2.12}$$

$$\partial_t J - w_0 = 0 \tag{2.13}$$

where $$\hat{\underline{q}} = \frac{1}{h} \int_{-h}^{0} \underline{q} \, dz \tag{2.14}$$

<u>baroclinic system</u>

$$\partial_t \underline{u}' - f \underline{u}'^{\perp} + \underline{\nabla} p' - \frac{1}{h} \int_{-h}^{0} \underline{\nabla} p' \, dz = \underline{q}' \tag{2.15}$$

$$\partial_t \begin{Bmatrix} T \\ S \end{Bmatrix} + \left[(\underline{u}' + [\hat{\underline{u}}]) \underline{\nabla} + (w' + [\hat{w}]) \partial_z \right] \begin{Bmatrix} T \\ S \end{Bmatrix} = \begin{Bmatrix} q_T \\ q_S \end{Bmatrix} \tag{2.16}$$

where $$\underline{q}' = \underline{q} - \hat{\underline{q}} \tag{2.17}$$

The interaction between the two systems occurs through the terms in square parentheses, the vertically averaged baroclinic pressure gradient in (2.12) and the advection of the density field by the barotropic current in (2.16). (The source function on the right-hand sides may also provide some coupling.)

2.1 The barotropic system

The quasi-stationary barotropic velocity field $\hat{\underline{u}}$ is determined by the time independent form of eqs. (2.12) and (2.13). The solution of these equations for the steady, vertically integrat ocean transport in the presence of a variable bottom topography and density field have been discussed extensively in the literature. The vertically integrated continuity condition (2.1

$$W_0 = -\nabla(h\hat{\underline{u}}) = 0 \qquad (2.18)$$

is normally used either to eliminate $\hat{\underline{u}}$ from eq. (2.12), thereby deriving a field equation for $\hat{p}$, or, alternatively, to express $\hat{\underline{u}}$ in terms of a scalar stream function ψ,

$$\hat{\underline{u}} = \frac{1}{h}\underline{\nabla}\psi \qquad (2.19)$$

thereafter eliminating $\hat{p}$. This is normally preferred, as the boundary conditions for ψ are a little simpler than for $\hat{p}$.

Applying the operator $\underline{\nabla}$ to eq. (2.12), one obtains as governing equation for ψ

$$\underline{\nabla}(f/h)\cdot\nabla\psi = \underline{\nabla}\hat{\underline{q}} - \underline{\nabla}\left(\frac{1}{h}\int_{-h}^{0}\underline{\nabla}p'\,dz\right) \qquad (2.20)$$

(It should be noted in eqs.(2.19), (2.20) that, in spherical coordinates, the relations div curl = 0 and curl grad = 0 become $\underline{\nabla}\underline{\nabla} = 0$ and $\underline{\nabla}\underline{\nabla} = 0$, with two different curl operators $\underline{\nabla}$ and $\underline{\nabla}$ corresponding to the co- and contragradient operators $\underline{\nabla}$, $\underline{\nabla}$).

The order of the differential equation (2.20) and therefore also the required form of the boundary conditions, depends on the form assumed for the barotropic forcing $\hat{\underline{q}}$. In the interior ocean the (grid-scale) nonlinear momentum advection terms are negligible, so that $\underline{q}$ is determined by the(subgrid-scale) turbulent momentum fluxes. Assuming the usual anisotropic turbulent friction expression

$$\underline{q} = \nu_v\,\partial_z^2\,\underline{u} + \nu_H\,\Delta\,\underline{u} \qquad (2.21)$$

where $\Delta = \underline{\nabla}\underline{\nabla}$ denotes the Laplacian operator and ν_v, ν_H represent vertical and horizontal eddy viscosity coefficients, one finds

$$\underline{\nabla}\hat{\underline{q}} \approx \underline{\nabla}(\underline{\tau}/h) - \left(\frac{f\,\nu_v}{2h^2}\right)^{1/2}\Delta\psi + \nu_H\Delta^2\psi + L(\underline{u}') \qquad (2.22)$$

where $\underline{\tau}$ is the surface (wind) stress and L is a linear operator acting on the baroclinic velocity field $\underline{u}'$. The exact form of L is irrelevant for the following; it

yields baroclinic friction terms analogous to the barotropic contributions in the second and third terms on the right-hand side of (2.22).

The horizontal and bottom friction terms represent the highest spatial derivatives in (2.22) and therefore determine the structure of the differential equation (2.20) and the boundary conditions of the problem. However, estimates of the orders of magnitude of these terms for friction coefficients ν_V, ν_H typically used in ocean models show that they are generally negligible in the interior of the ocean. The higher derivatives become important only in regions of high gradients near lateral boundaries and the equator. Ultimately these regions will have to be modelled separately. However, for the preliminary version of the model described here these regions are treated diffusively. For this purpose, it is sufficient to retain the bottom friction term in (2.22). Hence, the final equation for the barotropic system is

$$\frac{A}{h}\,\Delta\Psi + \underline{\nabla}\left(\frac{f}{h}\right)\cdot\nabla\Psi = \underline{\nabla}\left(\frac{\underline{\tau}}{h}\right) - \underline{\nabla}\left[\frac{1}{h}\int_{-h}^{0}\underline{\nabla}p'\,dz\right] \qquad (2.23)$$

where A is the bottom friction coefficient. Its value will be discussed in Section 4. The barotropic velocity $(\hat{u}, \hat{w})$ is then calculated from (2.19) resp. (2.8).

The boundary condition appropriate to (2.23) is a no-flux condition, i.e. Ψ = constant along lateral boundaries. In a simply connected domain, the value of that constant may arbitrarily be set to zero. In a multiply connected domain as the world ocean, however, that value is arbitrary along one coastline only. At other closed coastlines, it can be found as follows. Let Γ_i, i=1...N, denote the coastlines of all islands. The vorticity balance (2.23) may be written as

$$D[\Psi] = Q \qquad (2.24)$$

where Q denotes the right-hand side of (2.23). We define $\Psi_j(\underline{x})$ by

$$D[\Psi_0] = Q \quad , \quad \Psi_0 = 0 \text{ at all } \Gamma_i$$

$$D[\Psi_j] = 0 \quad , \quad \Psi_j = \delta_{ij} \text{ at } \Gamma_i$$

It is obvious that a solution to (2.24) is given by

$$\Psi = \Psi_0 + \sum_{j=1}^{N} \gamma_j \Psi_j \qquad (2.25)$$

The solution (2.25) has the value $\Psi = \gamma_i$ at the coastline Γ_i. The constants γ_j are determined according to Bryan & Cox (1972) by considering the barotropic momentum equation (2.12) which is rewritten as

$$-f\hat{\underline{u}} + \frac{1}{h}\int_{-h}^{0}\underline{\nabla}p'\,dz - \hat{\underline{q}} = -\underline{\nabla}\hat{p} \qquad (2.26)$$

Inserting the particular stream function (2.25) and integrating along the coastline Γ_i, the right-hand side of (2.26) drops out. Denoting the value of the integral of the left hand side for $\Psi = \Psi_j$ by I_{ij}, we obtain a system of equations for the γ_j

$$I_{i0} + \sum_{j=1}^{N} I_{ij}\,\gamma_j = 0 \qquad (2.27)$$

The system (2.27) is well-conditioned and can easily be solved. Effectively, in a model with 5° horizontal resolution there is only one island, Antarctica, as the barotropic transport between Australia and Asia is negligibly small.

2.2 The baroclinic system

The baroclinic velocity $\underline{u}'$ is obtained from the time-independent form of (2.15). In the interior ocean, we can neglect all nonlinear terms in the forcing $\underline{q}'$. However, for consistence with the barotropic system at least the vertical friction term has to be retained. In order to facilitate the evaluation of lateral boundary conditions, we also retain horizontal friction in $\underline{q}'$, yielding

$$\underline{q}' = \nu_V \partial_z^2 \underline{u}' + \nu_H \Delta \underline{u}' - \underline{\tau}/h \qquad (2.28)$$

Solving (2.15) for $\underline{u}'$ we obtain

$$\underline{u}' = \frac{1}{f}\left\{ -\nabla_\eta p' + \frac{1}{h}\int_{-h}^{0} \nabla_\eta p'\,dz + \nu_V \frac{\partial^2 \underline{u}'}{\partial z^2} + \nu_H \Delta_\eta \underline{u}' - \frac{\underline{\tau}}{h} \right\} \qquad (2.29)$$

Generally, the last three terms in the curled bracket of (2.29) will be small, resulting in a strictly geostrophic velocity field. Only near lateral and vertical boundaries, the friction terms give a significant contribution.

Boundary conditions for (2.29) are

$$\nu_V \partial_z \underline{u}' = \begin{cases} \underline{\tau} & \text{at } z = 0 \\ 0 & \text{at } z = -h \end{cases} \qquad (2.30)$$

and no-slip at lateral boundaries. In practice, the condition at z = -h is omitted, and ν_V is taken nonzero only at the uppermost level of computation. Its actual value is then irrelevant for the numerical computations.

The prognostic equations (2.16) for heat and salt do not require further simplifications, except for the specification of the turbulent fluxes q_T, q_S. Below the seasonal boundary layer, consisting of the surface mixed layer and the seasonal thermocline, the turbulent fluxes are neglected altogether.

The integration of the advective density equations (2.16) for the abyssal ocean is mathematically straightforward, once $\underline{u}'$, w' have been determined by (2.29), (2.8) and the barotropic velocities $\hat{\underline{u}}$, $\hat{w}$ by the diagnostic equations (2.23), (2.19) and (2.8). As boundary conditions T and S must be specified on all boundary surfaces with inflow; on the outflow boundary surfaces T and S are determined internally by the integration of the advection equations.

In the seasonal boundary layer a specific model has been developed which describes the turbulent fluxes in that layer and the thermohaline coupling to the atmosphere. This model is discussed in Section 7. In the present version of the circulation model the coupling of the seasonal layer to the deep ocean has been implemented as described in Section 3.1.

2.3 Wave properties

In order to understand the physics contained in the filtered set of equations (2.23, 2.19, 2.19), we consider the linearized form of those equations. The basic state is at rest wi a mean stratification $N^2(z) = -g\,\partial_z \bar{\rho}$. The bottom topography is linearized around a mean depth H_o according to

$$h(\underline{x}) = H_o + \underline{\alpha}\cdot\underline{x} \qquad (2.31)$$

with sufficiently small slope $\underline{\alpha}$. Furthermore, the ß-plane approximation is used, and a linearized equation of state is assumed such that equations (2.3) can be replaced by the corresponding equation for the density. Neglecting all turbulent fluxes, we obtain for the barotropic system

$$\left(\beta + \frac{f}{H_o}\alpha_2\right)\partial_1\psi - \frac{f}{H_o}\alpha_1\,\partial_2\psi = 0 \qquad (2.32)$$

and for the baroclinic system

$$-f\,\underline{u}' + \underline{\nabla}p' = 0 \qquad (2.33a)$$

$$\partial_t \rho + (\hat{w} + w')\,\partial_z \bar{\rho} = 0 \qquad (2.33b)$$

in conjunction with the hydrostatic relation (2.11) and the baroclinic part of the continuity equation (2.8). Although w in (2.33b) does not in general vanish, it is normally small compared to the baroclinic velocity w' and is therefore neglected.

From (2.32) it is seen that, in this approximation, there is no wave propagation in the barotropic field, neither from the planetary nor from the topographic restoring force. Thus, the fast time scales associated with these wave processes are indeed filtered out, as intended by the neglect of time rate of change of the relative vorticity in (2.32).

For the baroclinic system, from (2.15), (2.16) and (2.8) an equation for the pressure is readily derived

$$\partial_t \partial_z \left(\frac{\partial_z p'}{N^2}\right) + \frac{\beta}{f^2}\,\partial_1 p' = 0 \qquad (2.34)$$

with the boundary conditions

$$\partial_t \partial_z p' = \begin{cases} 0 & \text{at } z = 0 \\ -\dfrac{N^2}{f}\,\underline{\alpha}\,\underline{\nabla}p' & \text{at } z = -H_o \end{cases} \qquad (2.35)$$

Eq. (2.34) has plane-wave solutions

$$p' \sim \varphi_m(z)\, e^{i(\underline{k}\cdot\underline{x} - \omega t)} \qquad (2.36)$$

The vertical structure is given by the eigenvalue problem

$$\partial_z \left(\frac{\partial_z \varphi_n}{N^2} \right) + \frac{1}{g h_n'} \varphi_n = 0 \qquad (2.37)$$

$$\partial_z \varphi_n = \begin{cases} 0 \,, & z = 0 \\ N^2 \frac{\omega}{f} \underline{\alpha} \cdot \underline{k} \,, & z = -H_0 \end{cases}$$

The frequency is related to the eigenvalue $1/gh_n'$ by the familiar dispersion formula for long nondispersive Rossby waves

$$\omega = - \frac{\beta k_1}{f^2 / g h_n'} \qquad (2.38)$$

The equivalent depth, h_n', is typically o(1m) for the gravest modes. Its value is only very weakly dependent on the bottom slope $\underline{\alpha}$.

As the step from (2.33) to (2.34) does not require any additional approximations, it follows that planetary waves characterized by (2.38) are the only type of waves contained in the filtered equations of motion. Specifically, short

Rossby waves with eastward group velocities, and bottom trapped topographic waves (termed "fast baroclinic" by Rhines (1977)) are filtered out, as are all gravity waves and all barotropic planetary waves. At the equator, Kelvin- and Yanai-waves are filtered out, and only the (singular) limit $f \to 0$ of (2.38) is retained. The system does not support trapped equatorial modes.

East-west phase velocities based on (2.38) are given in Table 2.1 for several latitudes. The phase velocity is infinitely large at the equator and exceeds the maximum resolvable speed of 10 cm/s within a strip of approximately $\pm 20^o$. This singularity is a consequence of the perfect geostrophy in (2.33a). Retaining the time derivative in (2.33a) would remove the singularity and yield finite velocities of O(1 m/s) at the equator. However, that value still is too large to be resolved by our finite space-time grid. It is hence clear that a specific model for the equatorial region, is ultimately required. Presently, the time buffering as described below is essential in order to prevent numerical instabilities arising from the violation of the Courant-Friedrichs-Levy-criterion.

Table 2.1: Phase velocity $c = \beta g h_n' / f^2$ for $h_n' = 1$ m at various latitudes

Latitude	c [cm/s]
30^o	3.8
25^o	5.5
20^o	8.8
15^o	15.7
10^o	35.5
5^o	142

3. Present closure of the model in the boundary layers

The approximations leading to the model equations of the interior regime described in Section 2 are inappropriate in the boundary layers of the ocean, i.e. at the western and eastern boundaries of the oceanic basins, in the equatorial zone, in the upper seasonal layer of the ocean, and along the sea ice margin. It is planned to set up separate models for these climatologically important regions and patch together these models with the interior regime in a multi-regional global circulation model. As a first step a model for the seasonal layer has been constructed (cf. Section 7) but is has not yet been implemented in the simulations discussed in this report. So far the model has been closed in the boundary layers by frictional or diffusive parameterizations. The closure of the barotropic system is achieved by a frictional Stommel layer as explained in Section 2.1. The baroclinic system is also closed by friction at lateral boundaries. Since details depend on the discretization used for the numerical solution we will discuss this problem below in Section 4.2. The closures for the seasonal layer and the equatorial zone presently in the model are described below.

3.1 The seasonal layer

The seasonal layer has been coupled to the deep ocean model by a diffusive-corrective approximation of the turbulent fluxes

$$q_T = \partial_z \varkappa_v \partial_z T + \nabla \varkappa_H \nabla T + q_T^c$$

$$q_S = \partial_z \varkappa_v \partial_z S + \nabla \varkappa_H \nabla S + q_S^c \qquad (3.1)$$

and boundary conditions of the form

$$\varkappa_v \partial_z T = \alpha (T_o - T)$$

$$\varkappa_v \partial_z S = \alpha (S_o - S) \qquad (3.2)$$

at z = 0. Here T_o, S_o is observed surface temperature resp. salinity. The vertical diffusivity $\varkappa_v$ is assumed to vanish outside the surface layer so that there is no corresponding boundary condition at the bottom. The constant α is chosen such that $\alpha/d_1 = (3 \text{ months})^{-1}$, where $d_1 = 112$ m is the thickness of the uppermost layer of the model.

The horizontal diffusivity $\varkappa_H$ is nonzero only in an equatorial strip ($\pm$ 15°) and in the Arctic basin where it reaches maximum values of 2.5×10^4 $m^2 s^{-1}$. There is no heat- or saltflux through the lateral boundaries.

The convective flux divergences q_T^c, q_S^c are zero as long as the density stratification is statically stable. If an unstable stratification develops during the course of integration, q_T^c and q_S^c are chosen such that the temperatures and salinities of the respective layers are perfectly mixed while total heat and salt contents are conserved.

3.2 The equatorial time buffer

Approaching the equator the geostrophic approximation of the interior regime becomes invalid. Even if the singularity of the geostrophic relation is avoided by placing the grid points for the pressure field not directly on the equator, the phase speed of baroclinic Rossby waves becomes too large to be

resolved (Table 2.1 indicates that the phase speed c becomes larger than $\Delta x/\Delta t \approx 10$ cm/sec at latitudes less than about 15° from the equator). A usual technique to avoid the resulting numerical instability is to incorporate diffusion in the heat and salt equations as expressed in (3.1). However, the values of diffusivity necessary to cope with the numerically unstable waves would be rather high and thus this technique has the disadvantage of modifying the solution. To keep the diffusivity as low as possible we intr duced a time buffering procedure in the equatorial band (from 8.5° to -8.5°) which changes the wave solutions in this band (the singularity in the phase speed is removed) but leaves the steady state solution unchanged. The basic performance of the time buffer is described below. We should point out, however, that the buffering procedure in the numerical discretization does not follow exactly the differe version given below because of the intermediate step in the baroclinic part as described in Section 4.2.

Let the baroclinic velocity defined by (2.29) be denoted by $\underline{u}'_g$. Instead of (2.29) we introduce the coupled set of equations

$$\underline{u}' = \epsilon(\underline{u}'_g + \underline{U}) \tag{3.3a}$$

$$\partial_t \underline{U} = \gamma[(1-\epsilon)\underline{u}'_g - \epsilon \underline{U}] \tag{3.3b}$$

with the initial condition $\underline{U}(t=0) = 0$. Here γ is a time constant and $\epsilon = \epsilon(\theta)$ a prescribed function of latitude. Presently the values $\gamma = (\Delta t)^{-1}$ and

$$\epsilon(\theta) = \begin{cases} (\sin\theta/\sin\theta_0)^2, & |\theta| < \theta_0 \\ 1, & |\theta| > \theta_0 \end{cases} \tag{3.4}$$

are assigned, with $\Delta t = 2$ months being the time step of the numerical integration, and $\theta_0 = 8.5^{\circ}$ a reference latitude defining an equational strip. Outside that strip, (3.3) is identical to (2.29). Inside that strip, it is identical to (2.29) only in the steady-state limit.

Integration of (3.3b) yields

$$\underline{U} = \gamma(1-\epsilon)\int_0^t dt' \, \underline{u}'_g(t') \, e^{-\gamma\epsilon(t-t')} \tag{3.5}$$

showing that (up to a factor $\epsilon(1-\epsilon)^{-1}$) the velocity $\underline{U}$ may be identified as a (weighted) backward average over the geostrophic velocity $\underline{u}'_g$ with an averaging time scale $(\gamma\epsilon)^{-1}$.

The wave-guide properties of the modified system (3.3) are obtained by considering the linearized density equation

$$\partial_t \partial_z \left(\frac{\partial_z p}{N^2}\right) - \nabla\left(\epsilon[\underline{u}'_g + \underline{U}]\right) = 0 \tag{3.6}$$

Upon elimination of $\underline{u}'_g$ and assuming a wave structure $\exp i(k_1 x - \omega t)$ for all variables, we obtain

$$\begin{aligned} (-i\omega + \gamma\epsilon)U &= -\frac{\gamma}{f}(1-\epsilon)p_y \\ (-i\omega + \gamma\epsilon)V &= ik_1\frac{\gamma}{f}(1-\epsilon)p \\ \frac{\omega}{gh_n}p + \frac{\beta k_1}{f^2}\epsilon p - k_1\left(\epsilon_y\frac{p}{f} + \epsilon U\right) + i(\epsilon V)_y &= 0 \end{aligned} \tag{3.7}$$

This system has three eigensolutions one of which is immediately obvious: it has an eigenfrequency $\omega = \omega_1 = -i\gamma\epsilon$ and an eigenvector given by $p = 0$ and $\nabla \epsilon \underline{u} = 0$ which determines V(y) for arbitrary U(y). The other two modes are found by elimination of U and V which yields the relation

$$\left\{ \frac{\omega}{g h_n'} + \epsilon \frac{\beta k_1}{f^2} - \epsilon_y \frac{k_1}{f} + \gamma k_1 \left[\frac{\epsilon(1-\epsilon)}{f(i\omega - \gamma\epsilon)} \right]_y \right\} p = 0 \quad (3$$

Thus p(y) is arbitrary for these modes and U, V follow from (3.7). If we approximate the last term in the curly brackets by its value at the equator we find the eigenvalues from

$$\omega^2 + \omega\omega_0 + i\gamma\omega_0 = 0 \qquad (3.9)$$

with $\omega_0 = -\beta k_1 g h_n' / f_0^2$ where f_0 is the Coriolis frequency at the latitude θ_0. For the case $\gamma/\omega_0 \ll 1$, the approximate solutions of (3.9) are given by

$$\omega = \omega_2 = -i\gamma$$
$$\omega = \omega_3 = -\omega_0 + i\gamma \qquad (3.10)$$

Thus the buffer system possesses two damped zero-frequency modes (ω_1 and ω_2) and one weakly unstable wave mode (ω_3). This latter mode propagates eastward (in contrast to Rossby waves outside the buffer) with the constant phase speed $\beta g h_n' / f_0^2$. The reversal of the propagation direction is

an artifact caused by the modification of the geostrophic balance (essentially 1/f is replaced by f in the equatorial strip as can be seen from (3.3)).

To summarize: the time buffer replaces the highly numerically unstable Rossby waves in the equatorial zone by a mode system which is slightly kinematically unstable. This instability as well as the remaining numerical instability in the transition zone between the time buffer and the stability boundary of the Rossby waves (i.e. between 8.5° and 15°) is handled by an explicit diffusivity.

4. Numerical solution techniques

For the horizontal discretization of the equations we use a grid staggering technique, which fits the structure of the equations as close as possible. In Arakawa's terminology it has the notation E (Arakawa and Lamb, 1976). For time dependent solutions of shallow water equations, the E-type staggering has the tendency to separate into two disjunct grids. For that reason it is very seldom used. However, for our purposes, where perpendicular gradients for geostrophic current and advection of water properties are involved, it seems to be ideal.

The arrangement of gridpoints is

```
+  X  +  X  +  X
X  +  X  +  X  +
+  X  +  X  +  X
X  +  X  +  X  +
```

The points denoted by "X" are vector points where the components of u and v are evaluated, and the "+"-points are scala points where S, T, w, and p are evaluated. The distance between corresponding points is 5^{o} in both directions.

For the discretization of the topography, we took the bathymetry as used in Bryan's 1^{o}-model. For the reduction on our coarser grid, we averaged the corresponding neighbour points of the finer grid. After that step, an inspection showed the need for only minor corrections. The final topography is shown in Fig. 4.1, together with the lines of constant f/h. For our grid staggering, the topography is thought to be given in vector points, the depth at the scalar points is assumed as the maximum of the four surrounding vectorpoints. By this assumption, it is ensured that in any equation sensible values at the neighbourpoints are present. If, for instance, at a u-point the depth is greater than the actual level of computation, the four surrounding p-points have greater depths too. If, at a p-point, in the advection equati for a "wet" point information should be needed from a neighbouring "dry" point, the corresponding advection velocit using upwind differences, is zero.

Vertically there are 5 levels of computation, at 75, 150, 300, 1000, and 3000 m. As the topography does not fit the levels of computation, additional information must be kept about the transport depth accorded to a given vector point, in order to achieve mass continuity.

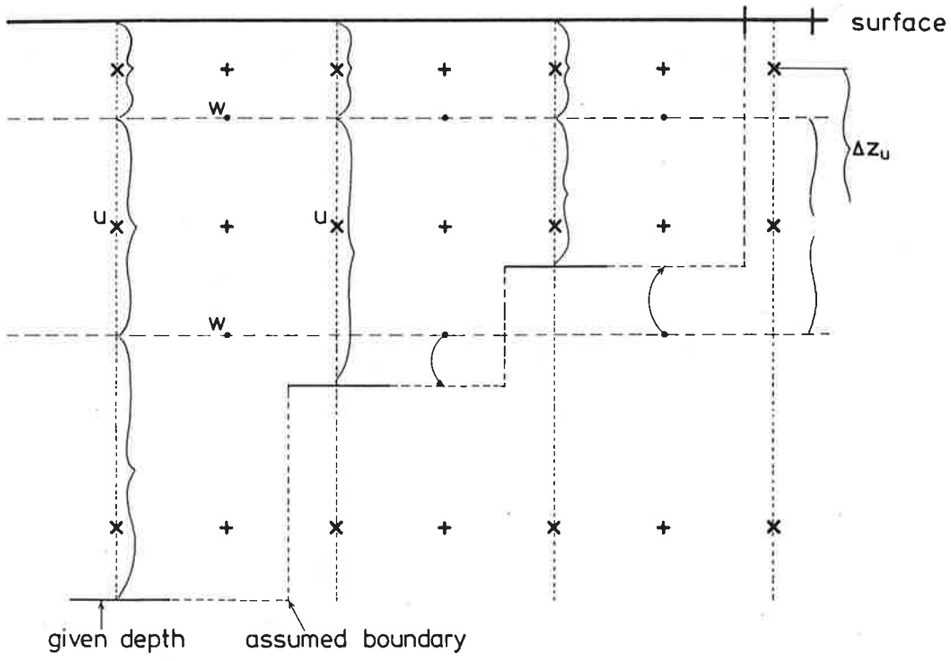

As an example, an x-z-section is sketched in the diagram. The computed vertical components w in the fixed levels have a meaning when the underlying cell is wet. For the nearest bottom cell, one must take into account that the physical depth, where w = 0 does not in general fall on a level. It is obvious that the value of w at the upper side of the bottom cell obeys the kinematic boundary condition $w = -uH_x$.

4.1 The barotropic part

Equation (2.23) for the mass-transport stream function is formally a second-order equation due to the inclusion of bottom friction. However, the friction coefficient A normally is chosen rather small so that in the interior ocean (2.23)

essentially behaves like a first-order equation. In a coarse grid like that of our model, this yields the well-known prob of the advection equation (e.g. Grotjahn & O'Brien, 1976, Ma Reimer, 1973). We assume that the explicit value of A is smaller than the friction introduced by the numerical scheme as discussed below so that the first term in (2.23) can be neglected.

To prevent the structure of "chessboard solutions", we use a modified version of the "vector-upstream" method. Let us consider an elementary cell of the grid:

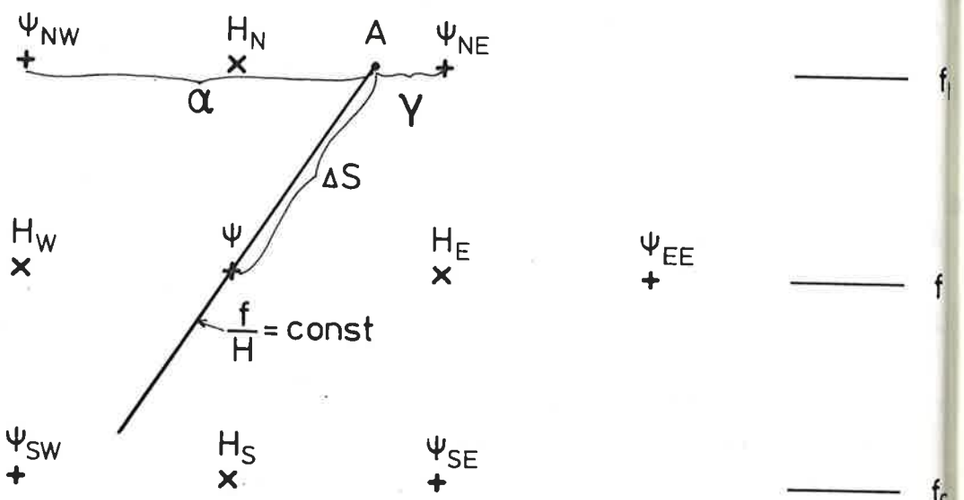

Equation (2.23) may be written as

$$\nabla\left(\frac{f}{h}\right)\cdot\nabla\Psi \quad = \quad C \qquad (4.1)$$

or explicitly as

$$f\left[\left(\frac{1}{H}\right)_y \Psi_x - \left(\frac{1}{H}\right)_x \Psi_y\right] + \frac{\beta}{H}\Psi_x = C \qquad (4.2)$$

the indices x, y denoting partial derivatives. The data points for the water depth are given at "X"-points. The direction of the f/H characteristic at the center of the cell is extrapolated up to the dissection with the sides of the cell. In the above example, the characteristic dissects the sides of the rectangle at point A which is not a grid point. Between point A and the center, we evaluate the effective gradient G and compute the change in Ψ by

$$\Delta\Psi \quad = \quad C\,\Delta S / G \qquad (4.3)$$

In this procedure it is quite easy to incorporate boundary conditions for Ψ.

For the planetary part, i.e. the β-term, we take the difference between Ψ and Ψ_{EE}

$$\frac{\beta}{H}\Psi_x \approx \frac{\beta}{H_E \Delta x}\left(\Psi_{EE} - \Psi\right) \qquad (4.4)$$

Summing up both contributions, we obtain

$$\frac{G}{\Delta S}\left[\alpha\Psi_{NE} + \gamma\Psi_{NW} - \Psi\right] + \frac{\beta}{H_E \Delta x}\left(\Psi_{EE} - \Psi\right) = C \qquad (4.5)$$

or

$$\Psi\left[\frac{G}{\Delta S} + \frac{\beta}{H_E \Delta x}\right] = \frac{G}{\Delta S}\left[\alpha\Psi_{NE} + \gamma\Psi_{NW}\right] + \frac{\beta}{H_E \Delta x}\Psi_{EE} - C \qquad (4.6)$$

From (4.6) the new ψ-value is computed.

The formulation of upstream differences introduces a mutual nivellation of the results which can be identified with a phys friction. This friction has just the amount that would be required in a formulation with - a priori more accurate - cent differences in order to avoid chessboard solutions (independen of the grid staggering type). It corresponds to a bottom fricti coefficient of the order $A \approx f\,\delta(f/h)/(f/h)$ where $\delta(f/h)$ is th change of f/h between neighbouring grid points. That value assures that the western boundary current is always confined t the continental slope. The upwind formulation has the advantag that the enormous friction coefficients appearing in numerical ocean models are used only in limited parts of the ocean where they really are needed for numerical reasons. Our method of ve upstream differences has the additional advantage that the numerical friction acts more along rather than normal to the characteristics.

With a grid resolution of 5^{o}, the neighbourhood relations (4. yield a system of 3382 linear equations for the values of at the grid points. A naive application of direct solution procedures would involve the complete inversion of a matrix of order 3000. That procedure would require an unreasonable amount of computertime, despite accuracy problems. Iterative procedures seem to be much more appropriate. Their applicability is, however, limited; the convergence depends on the relation of the diagonal elements of the matrix to the non-diagonal ones. Even for a genuine elliptic system, taking the result of the previous time step as guess, a considerable number of sweeps must be carried out for a sufficient accurac For our system which still reflects the first order character of the differential equations, including the singularities of closed f/H lines and equatorial coastal points, a much worse behaviour must be expected.

In our solution of the system, we take advantage of some specific properties of the matrix:

1) The matrix has a band structure. Taking an appropriate ordering of the grid points along latitude circles, starting at each circle at the point south-west from the more northern starting point, it turns out that neighbour points are separated by not more than 73 numbers from each other; all non-zero elements of the matrix lie in a band of width 73 around the diagonal.

2) The matrix is sparse, the maximal elements of a line are at the diagonal. During the elimination procedure, elimination factors greater than unity appear frequently. In general, this yields a dramatic increase of round-off errors which must be avoided by pivoting, thus abandoning the band structure. In our matrix, there are so many small elements that the occasional increase of errors is compensated by many subsequent decreases. In fact, an a-posteriori test showed that the solution obtained by elimination fullfilled the difference equations up to an accuracy of 10^{-10} (on our 60-bit-word computer which has a single operation accuracy of 10^{-13}).

These two properties allow for an elimination procedure without pivoting within the band. There is no need to held the whole band - it contains about 5×10^{5} elements - in the core memory. During the triangularisation only a rhomboid section of the matrix is needed, in our matrix a section of 74x147 elements. The procedure may be illustrated by an example of bandwith 4:

Assume that, at a given state of the triangularisation, all subdiagonal elements up to an index m are zero (denote zero elements by O, nonzero elements by e, diagonals by D).

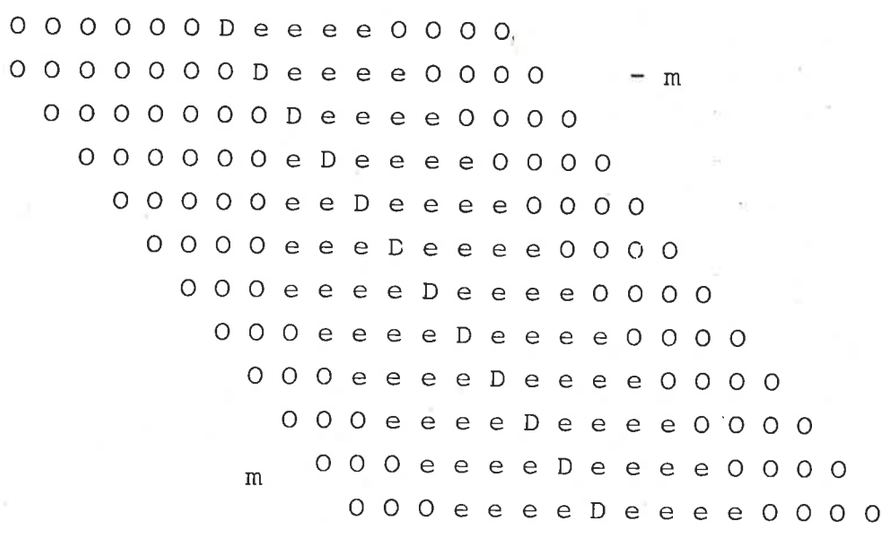

To obtain this state for m+1, it is obviously sufficient to perform operations within the indicated rhombus. During the elimination, the remaining upper diagonal lines and the elimination factors are stored on disc. This rather time consuming job of triangularisation has to be performed only once; during the genuine model run, the matrix remains the same, only the right-hand side of the equation changes. Using the stored lines and elimination factors, the solution at each timestep reduces to a very limited munber of simple arithmetic operations.

4.2 The baroclinic part

Whereas in the barotropic part it is possible to match local relationships globally together, the situation is different for the baroclinic part. It should be possible, in principle, to introduce "implicit" procedures, that is, to insert into the difference approximations at each time step the unknown neighbour values at the new time step. The evaluation at the new timestep then involves a large system of algebraic equatio Such procedures are well suited for the shallow water equation

For our baroclinic system, such a method seems to be less appropriate. Firstly, in the main part of the oceans, the remaining waves are so slow that we want to resolve them explicitly; secondly, as they stem from a nonlinearly coupled system of equations, the resulting matrix system would be a nonlinear one with coefficients changing at each time step. The iteration procedure would be very time consuming, cancelling out the main advantage of the large time step.

In our model, we use a rather simple quasi-explicit method which well describes Rossby waves outside the equatorial region over flat topography. Near the equator we use a time buffer as described above in order to damp out fast oscillations. As fast oscillations are combined with small displacements, we believe that such a modification, acting only at places where it is really needed, is justified.

For a description of the discretization of the full set of equations, we omit the index handling as far as possible. The continuity equation is already lined out. In the momentum equation direct pressure gradients between the neighbouring pressure points are taken. For the hydrostatic relation, the uppermost density is extrapolated up to the real surface; the integral $\int \varrho \, dz$ is evaluated by the trapezoidal rule. The equation of state is evaluated according to a modification of Eckart's formula, given by Friedrich and Levitus (1972).

For the advection of T and S, a modified upwind scheme is used. The content of a cell at the new time step is taken as the weighted average of the content at the old time step and the neighboured contents entering the cell. In two dimensions this can be written as

$$T^{t+\tau} = \frac{T^t + \tau\,(u_W^* T_W + u_E^* T_E + u_N^* T_N + u_S^* T_S)}{1 + \tau\,(u_W^* + u_E^* + v_N^* + v_S^*)}$$

where τ is the time step.

The symbols are explained in the following diagram.

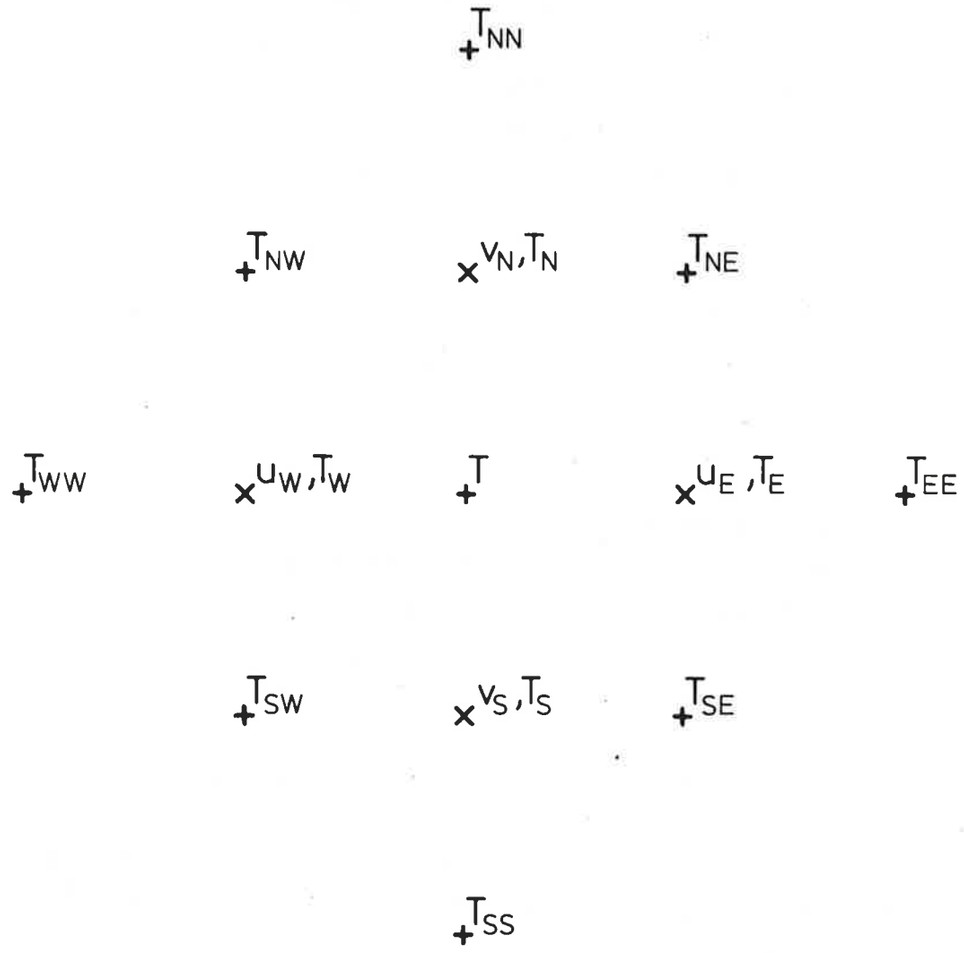

The quantities u_W, u_E, u_N, u_S are defined as the inflow velocities divided by the corresponding grid interval; they vanish for outflow conditions.

In three dimensions (4.7) is extended in an obvious way. For small advection velocities (4.7) is identical to the well-known and well behaved upwind scheme. It introduces an artificial diffusivity proportional to the velocity, which is just as large as would be needed in a - more accurate - centered scheme for avoiding chessboard solutions. For the fictitious neighbour values T_N, T_S, T_W, T_E an appropriate interpolation between the next points holding information about T must be taken. In order to avoid the grid separation we simply take

$$\text{e.g.} \quad T_N = (T + T_{NN} + T_{NE} + T_{NW})/4$$

We emphasize that this interpolation does not yield a high diffusivity; its influence depends on the advection velocities.

In order to minimize index handling, we illustrate the time discretization scheme for the shallow water equations described by elevation ζ and (equivalent) gravity g'.

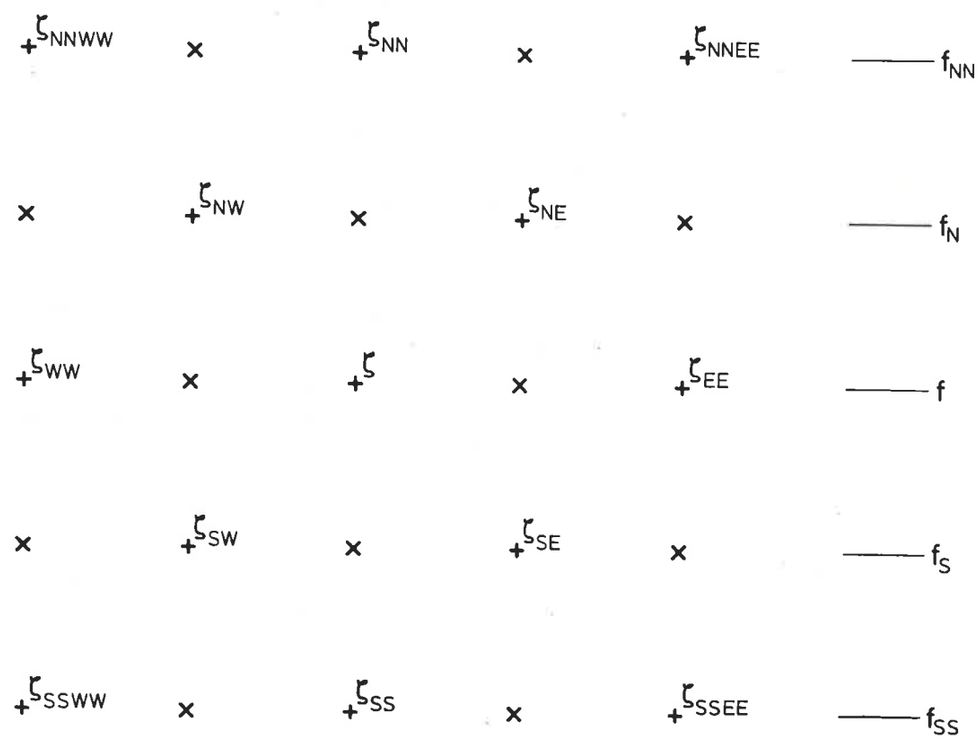

At a given time t the ζ-values are known. For cartesian gri in a β-plane with constant spatial increment h, the geostrop relations (neglecting friction) are

$$u = -\frac{g'}{f\ell}\left(\zeta_N - \zeta_S\right)$$

$$v = \frac{g}{f\ell}\left(\zeta_E - \zeta_W\right) \qquad (4.8)$$

Using these u,v, we compute a field ζ' at an intermediate time step from the mass conservation

$$\zeta' = \zeta^t + \frac{h\tau}{2\ell}\left(u_W - u_E + v_S - v_N\right) \qquad (4.9)$$

With this ζ' we determine the advection velocities acting over the full time step

$$u' = -\frac{g'}{f\ell}\left(\zeta_N' - \zeta_S'\right)$$

$$v' = \frac{g'}{f\ell}\left(\zeta_E' - \zeta_W'\right) \qquad (4.10)$$

The change of ζ over the whole time step is finally given as

$$\zeta^{t+\tau} = \zeta^t + \frac{h\tau}{\ell}\left(u'_W - u'_E + v'_S - v'_N\right) \qquad (4.11)$$

In order to investigate the stability properties of this difference scheme, we use (4.8), (4.9) and (4.10) to express the right-hand side of (4.11) in terms of ζ^t. After some algebra one obtains

$$\zeta^{t+\tau} = \zeta^t\left[1 - \frac{1}{2}\frac{(gh\tau)^2}{(\ell f)^4}\beta^2\ell^2\right]$$

$$+ \frac{g'h\tau}{2\ell^2f^2}\left[\zeta^t_{NE} + \zeta^t_{SE} - \zeta^t_{NW} - \zeta^t_{SW}\right] \qquad (4.12)$$

$$+ \frac{(g'h\tau)^2}{4\ell^2f^2}\beta^2\left[\zeta^t_{EE} + \zeta^t_{WW} - \zeta^t_{NN} - \zeta^t_{SS} + \frac{1}{2}\left(\zeta^t_{NNEE} + \zeta^t_{SSEE} + \zeta^t_{NNWW} + \zeta^t_{SSWW}\right)\right]$$

If we now introduce a periodical distortion $\exp(i(kx + \mu y)$ for ζ^t, we have the numerical dispersion relation

$$\zeta^{t+\tau} = \lambda\,\zeta^t \qquad (4.13)$$

with

$$\lambda = 1 - \frac{1}{2}\frac{(gh\tau\beta)^2}{\ell^2f^4} + 2i\,\frac{g'h\tau\beta}{\ell f^2}\cos\frac{\mu\ell}{2}\sin\frac{k\ell}{2} + \qquad (4.14)$$

$$+ \frac{1}{4}\left(\frac{g'h\tau\beta}{\ell f^2}\right)^2\left[2\cos k\ell - 2\cos\mu\ell + \frac{1}{2}\cos k\ell\cos\mu\ell\right.$$

The complex number λ contains phase shift and amplification (or damping) of the wave during one time step. Fig.4.2 shows its modulus at typical midlatitudes dependent on k and μ. For most parts of the spectrum, the difference scheme produces a slight damping. A slight increase is produced for large μ and small k. These waves have to be damped at the coasts. The effect of the intermediate step can be seen in the terms containing β^2. Omitting them, we have the result for the simple forward stepping procedure which would be unstable in any case.

So far we have assumed that the baroclinic velocity $\underline{u}'$ is evaluated from the geostrophic relation (2.29) or, in the equatorial zone, by the time buffering procedure described in Section 3.2. At lateral boundaries, however, neither of these relations will in general satisfy the condition of a vanishing normal component of the velocity. (Remember that the barotropic velocity satisfies this condition separately, as described in Section 2.1.) Hence, geostrophy is abandoned explicitly at lateral boundaries as indicated in the followin graph.

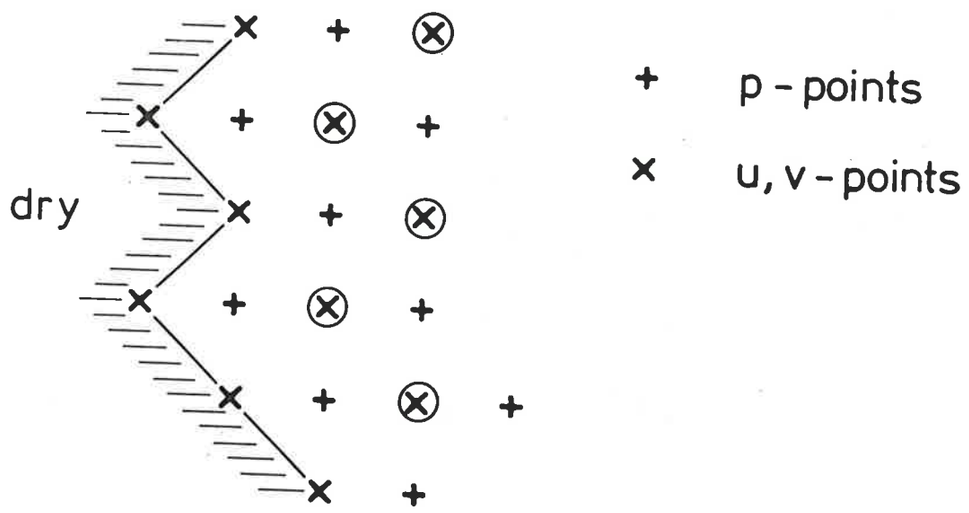

The boundary is chosen to coincide with u,v-points. Here the boundary condition $\underline{u}' = 0$ is set explicitly. In the adjacent u,v-points (circled in the sketch) the baroclinic velocity is calculated geostrophically from the surrounding pressure values. The vertical velocity in column is calculated from the continuity equation with the geostrophic inflow.

5. Results of a 60-year integration

The circulation model described in the preceding sections has been integrated for a time span of 60 years. As initial conditions, the annual averages of the fields of temperature and salinity from an updated version of the global analysis of Levitus and Oort (1977) were used. The wind stress distribution is shown in Fig. 5.1; it is essentially identical to that of Hellerman (1967).

5.1 Temperature and salinity

Figs. 5.2 - 5.6 display the horizontal distributions of temperature and salinity at the 5 levels of computation: (a) observed (initial) distribution, and (b), (c) and (d) after 5, 20 and 60 years of integration, respectively. In the uppermost level (75 m, Fig. 5.2) both fields remain almost unchanged, a deliberate consequence of the rather large value of α in the boundary condition (2.31). Only a small amount of smoothing of the initial fields takes place, especially in the equatorial regions.

In the next level (150 m, Fig. 5.3) the time evolution is much more pronounced. Three regions can be identified where already after 5 years considerable changes occur:

(i) the western boundary regions (WBR) of the subtropical gyres, (ii) the equatorial regions and (iii) the Antarctic Circumpolar Current (ACC). In the WBR the isothermals are initially more normal to the coast line while after 5 years they are more parallel, and both the temperatures and the salinities are lower. In the equatorial regions, the predicted fields are considerably smoother than the initial values, and the zonal temperature gradients in both the Pacific and Atlantic basin are wiped out. In the ACC the tendency is opposite: while the initial fields are zonal and rather smooth, the predicted fields show much more structure, strongly resembling the topography in this area. It should be pointed out that the data base in the Southern Ocean on which the observed maps are based is very sparse, and the smoothness of the initial maps is more or less caused by the method of their construction.

Overall, the fields at 150 m do not change much from 5 to 60 years and it seems that an equilibrium is reached after 5 - 10 years. Similar remarks apply to the distributions at the 300 m level (Fig. 5.4) which will not be discussed separately. The situation is different, however, at the deeper levels (Figs 5.5 and 5.6). There are considerable changes between the 20y and the 60y maps, especially at the 3000 m level, and it is by no means obvious that an equilibriu state has been reached after 60y. This point will further be discussed below.

Various sections of T and S for t = 0, 5y, 20y and 60y are shown in Figs 5.8 - 5.13. The sections are labelled as 1, 2, 3, 40^{o}N, Eq, ACC; their location is indicated in Fig. 5.1 The North-South section in the Atlantic (Fig. 5.8) shows the

destruction of the initial meridional structure of the equatorial thermocline already after 5 years, resulting in a nearly horizontal thermocline between 20^{o}S and 20^{o}N after 20 years of integration. This result indicates that the horizontal diffusion in the equatorial strip may be too large. At higher latitudes the structure of the thermocline remains unchanged in the North Atlantic but becomes shallower in the South Atlantic. Below 1000 m depth a deepening of the isotherms can be observed, resulting in a gradual warming of the lowest layer especially in the southern hemisphere. At the same time, the salinity increases and the tounge of Antarctic Intermediate Water (Fig. 5.8c) vanishes after 20 years. It seems that the convective adjustment procedure leads to less convective mixing than necessary to maintain the deep ocean T-S values. The inclusion of seasonal variations in the surface fields probably would improve this situation (see e.g. Bryan & Lewis, 1979).

The north-south sections 2 and 3 (Figs 5.9 and 5.10) exhibit similar features as the Atlantic section, and no individual discussion is given.

The 40^{o}N-section (Fig. 5.11) shows, besides warming of the deeper layers, a complete erosion of the salinity stratification after 20 years. Furthermore, strong changes occur near the coasts of both basins, probably a consequence of too large vertical velocities (see below). Also, the salinity maximum in the East Atlantic due to Mediterranean outflow is eroded (Fig. 5.11c). A more realistic model would have to introduce a source of salt in that region.

Fig. 5.14 shows time series of temperature at 1^{o}N on section 1 for the different levels. Initially, the temperature in the upper levels jumps to a higher value within a few time steps, indicating that the initial density field is dynamically not

consistent with the diagnostic velocity field. After 2 - 5 ye the temperature has more or less adjusted to an equilibrium which is somewhat different from the initial value. At deeper levels, starting at 300 m, the situation is different. Here, the adjustment time scale is larger, and after approximately 20 years a clear trend for increasing temperatures is seen. I is obvious from Fig. 5.14 that within the 60 years of integration the lower layers have not reached an equilibrium. As discussed above, the most likely reason for this behaviour is the absence of strong convective mixing in our model.

Fig. 5.15 shows the same information at 20° N. Here a new feature is observed after the initial adjustment: almost stationary oscillations with a period of less than 1 year, an an amplitude of 0.3° C. These oscillations probably originate from the numerical instability discussed in Section 2.3 which is not completely suppressed by the time buffering procedure and by equatorial diffusion. A detailed investigation of the results shows that indeed the fluctuations are small both near the equator where diffusion and buffering is effective as well as in higher latitudes where the instability does not occur. To avoid the occurrence of instabilities, the region where the time buffer is effective will have to be enlarged t approximately ± 20°.

In order to remove these fluctuations from the final results, the integration was extended from 60y to 65y and averages of all fields over this period were taken. For the T-S distributions, differences were generally negligible and the average maps are not shown.

5.2 Horizontal velocity

Fig. 5.16 shows maps of the horizontal velocity in all five levels (a - e) and the barotropic velocity (f) after 60 years of integration. The surface layer circulation (Fig. 5.16a)

exhibits several typical structures, viz. subtropical gyres with relatively broad western boundary currents, an equatorial current system including a more or less well defined counter-current, and an Antarctic circumpolar current strongly coupled to the topography. Most of those features persist at the 150 m level (Fig. 5.16b) although in the Atlantic the equatorial circulation is somewhat reversed. The North Atlantic subtropical gyre shows more small-scale structure than to be expected from the bottom topography. In 300 m depth (Fig. 5.16c) a broad and strong "equatorial undercurrent" shows up in both the Pacific and Atlantic basin. In the Pacific, this current persists down to the 1000 m but is reversed again at the lowest level (Fig. 5.16e).

Fig. 5.17 shows the horizontal circulation averaged over the period from 60 - 65y. Comparison with Fig. 5.16 reveals essentially no differences, except for a few minor details near boundaries.

5.3 Vertical velocity

Maps of the vertical velocity after 60y on all 4 levels of computation are shown in Fig. 5.18. Generally the fields exhibit much more small-scale structure than density or horizontal velocity. This behaviour is not surprising as computation of the vertical velocity involves twice differentiating the density field. The uppermost level is dominated by Ekman pumping resulting in downwelling over the subtropical gyres and upwelling in the equatorial and Antarctic regions. Near the coastlines the spatial variability is stronger than in the open ocean. The magnitudes are typically $O(10^{-5}$ cm $s^{-1})$.

In the deeper levels small-scale structures of approximately 2 gridpoints wavelength become rather strong outside the immediate vicinity of the equator and in the western boundary

region. It is very suggestive that they are caused by the oscillations arising from numerical instability as discussed above. Consequently, those structures should disappear once the fields are averaged over 5 years. That is indeed the case as can be seen from Figs 5.19b - d: in the areas where the oscillations occur a considerable amount of smoothing occurs whereas the remaining parts of the maps are virtually unchanged.

Other interesting aspects are the upwelling below the thermocline under larger parts of the subtropical gyres, notably in the North Pacific, and the downwelling below the equatorial undercurrent (Fig. 5.19c). The deepest level (Fig. 5.19d) is characterized by downwelling in the eastern part and upwelling in the western part of most basins.

Fig. 5.20 shows time series of the vertical velocity at 20^{o} N (a) and at 1^{o} N (b). It is clearly seen that the w-fluctuations are stronger than those in T-S or horizontal velocity. Also, the success of the equatorial buffer in surpressing the fluctuations is demonstrated.

5.4 Numerical diffusivity

The numerical diffusivity introduced by the modified upstream scheme (4.7) in the vertical direction is $|w| \Delta z$, up to a factor O(1). That quantity is displayed in Figs 5.21a - d for all 4 levels. In the uppermost layer, typical values are O(1 $cm^2\ s^{-1}$). At 650 m values are typically between 1 and 10 $cm^2\ s^{-1}$, and in the lowest layer they frequently exceed 10 $cm^2\ s^{-1}$ considerably and occasionally reach values of 100 $cm^2\ s^{-1}$. Clearly, those large values are unwelcome as they may prevent the establishment of a purely advective regime in deep-ocean heat and salt budgets.

6. Tracer experiments

As first application of the ocean circulation model, we have used the velocity field after 60 years to simulate the distribution of two dynamically passive tracers:

(a) bomb-produced tritium ^{3}H

(b) natural ^{14}C.

A few results of those simulations will be discussed in the following.

6.1 Tritium

In the 1950s and early 1960s nuclear tests added large amounts of tritium to the northern hemisphere stratosphere from where it leaked to the troposphere and finally to the ocean surface waters mainly by water vapor exchange and rainfall. The concentrated introduction of tritium into the ocean, mainly in 1963-64, makes this isotope a powerful tracer for the water movements in the upper ocean. For our model, tritium simulation and comparison with the observed tritium field in the ocean provides a strong test of water exchange between the surface layer and the deeper layers.

The transport of tritium is governed by the advection equation

$$\partial_t C + (\underline{u}\underline{\nabla} + w\partial_z) C = -\lambda C + q \qquad (6.1)$$

where C is the local tritium concentration and $\lambda^{-1} = 12.4$ years is the time scale of radioactive decay. The source term $q = q_{in} + q_c$ consists of two contributions, the convective flux divergence q_c and the atmospheric input q_{in}. This latter source q_{in} is prescribed as in the uppermost layer

according to the tritium flux analysis of Weiss and Roether (1980). The open ocean input by rainout and water vapor exchange is given as a product of a function of time and a function of latitude. The time dependence for the northern hemisphere is displayed in Fig. 6.1. The input by river runoff and outflow of air mass from the continents is placed in the eastern- or westernmost box of the upper layer in each latitudinal band. The relative importance of these three modes of tritium input for the North Atlantic can be obtained from Fig. 6.2 showing the contributions to the total input up to 1972 in each 5^{o} latitudinal band. Here, river runoff and continental outflows account for 25 % of the total input. The ratios for the other basins are given in Table 6.1 adopted from Weiss and Roether (1980). Except for the northern Indian Ocean and North Atlantic the open ocean input is seen to be the dominant input mode. The input function of Weiss and Roether (1980) is accurate to about 20 % and agrees within this accuracy with the tritium inventories for the North Atlantic and the Pacific Ocean.

We have run two cases which were identical except for the convective flux divergence q_c. In first case convection was neglected completely, while in the second case convection was accounted for in the following way: at each grid point, the tritium content was mixed to a certain depth depending on latitude. That depth was chosen as follows: 2000 m (level 1 poleward of 70^{o}, 650 m (level 3) from 50^{o} - 70^{o}, and 225 m (level 2) from 40^{o} - 50^{o}. These depths are a rough approximation to the maximum depth of deep convection during the winter time in the North Atlantic as e.g. shown in the atlas of Robinson et al. (1979). In the Pacific Ocean the convection amplitude is known to be considerably smaller, so that the convective run is inappropriate in this basin. The run without convection will be referred to as diffusive simulation though diffusion in the simulations reported here are caused by

	Northern Hemisphere			Southern Hemisphere		
	I_{EP}	I_{RV}	$I_{RV}/(I_{EP}+I_{RV})$	I_{EP}	I_{RV}	$I_{RV}/(I_{EP}+I_{RV})$
Atlantic	173.9	519.5	25%	91.4	11	10%
Pacific	674.5	60	8%	208.9	7	4%
Indian Ozean	54.2	32.8	38%	154.1	4	3%

Table 6.1: Tritium input to the world ocean up to the end of 1972 by open ocean exchange (I_{EP}) and river runoff and continental outflow (I_{RV}) in MCI.

numerical discretization only. As the advecting velocity field is constant in time, we used a different numerical technique to solve e.g. (6.1) as compared to the analogous system (2.3), namely an implicit upstream scheme. For a one-dimensional equivalent of (6.1), the discretized form is given by

$$C^{n+1} - C^{n} + \frac{\Delta t}{2}\left[u_w^*\left(C_w^{n+1} + C_w^{n} - C^{n+1} - C^{n}\right) + u_E^*\left(C_E^{n+1} + C_E^{n} - C^{n+1} - C^{n}\right)\right] = -\lambda C^{n+1}$$

Here n is the time index, and u_W^*, u_E^* are defined as in (4.7).

The resulting system of equations for the C^{n+1} was solved iteratively; for each time step sufficient accuracy was achieved after 12 iterations. The implicit formulation (6.2) allowed to select the large time step Δt = 1y. For the convective runs the mixing procedure was inserted after each time step. In this way equation (6.1) was integrated from 1952 to 1972 with initial condition C = 0 everywhere. The simulations shown below refer to 1972. They will be compared with the observed tritium field constructed from data obtained by the GEOSECS programme during 1972-74.

The global maps of the diffusive simulation are displayed in Fig. 6.3 . These results will be compared with Pacific GEOSECS data. The model section 3 (cf. Fig. 5.7) is shown in Fig. 6.4. Some of the GEOSECS data are reproduced in Fig. 6.5, the tritium concentration at the surface (a), the western (b) and eastern (c) NS-sections (from Fine et al., 1981, Östlund and Fine, 1979). In the Atlantic we will

discuss both the diffusive and the convective runs. The model section 1 for these cases as well as the western Atlantic section of GEOSECS (from Östlund et al., 1976) are shown in Fig. 6.6. Fig. 6.7 displays maps of the North Atlantic part of the diffusive and convective runs. These may be compared with Fig. 6.8 which reproduces the tritium analysis of GEOSECS and other data by Sarmiento et al. (1982).

Let us first consider the Pacific in more detail. The surface values (Fig. 6.3) show a general decrease from north to south which reflects the greater input rate in the northern hemisphere. The highest concentration occurs in the eastern basin. The North-Equatorial Current seems to prevent penetration from the northern to the southern hemisphere resulting in a strong meridional gradient in this region. The isolines bend towards the north in the western part of the basin apparently due to transport by the western boundary current. These features as well as the magnitude of the surface tritium concentration compare favourably with the observations shown in Fig. 6.5a. The NS-section 3 (Fig. 6.4) reveals that most of the tritium is found in the upper 1000 m of the northern hemisphere. There is a fairly good agreement with the data (Figs 6.5b and c) with respect to the penetration depth. The simulation even gives an indication of the subsurface maximum below the strong surface gradients of the North-Equatorial Current.

The GEOSECS section Fig. 6.6c reflects the drastic difference of tritium penetration in the Atlantic and Pacific ocean. The isopleths in the North Atlantic indicate the effective downward motion of water masses newly formed in the Norwegian and Greenland seas flowing over the sill of the Denmark Strait into the deep ocean. This sinking plume is entirely absent in the Pacific Ocean. The model reproduced the plume in the diffusive as well as in the convective run (see Figs 6.6a and b). Convection in the model smoothes out the strong subsurface gradients in mid- and highlatitudes appearing in the diffusive

run. Without convection the tritium does not get deep enough in these regions. The convective run is thus preferable in agreement with the simulations of Sarmiento (1982). The penetration in low latitudes, however, is too deep in the model. Also, there is disagreement in the surface layer which shows too large concentrations within the region of the subtropical gyre.

These features also appear in the tritium maps of the North Atlantic displayed in Fig. 6.7. Whereas the tritium values (apart from the detailed structure) for the convective run in the deep layers (300 m and 1000 m) agree roughly with the observations (Fig. 6.8) the values in surface layers (75 m and 150 m) are too high in mid-latitudes and somewhat too low in higher latitudes. In particular the high concentration off Europe in the upper layers seem to be unrealistic. The diffusive run suffers from these discrepancies even more. A further disagreement is apparent in the downward moving plume off Brazil visible in the 1000 m map. This is caused by the downward direction of the vertical velocity at this coast (see Fig. 18) which is an unrealistic artifact of the model. As already in the case of temperature (cf. Figs 5.3 - 5) the simulated isopleths of the tritium also run parallel to the coast in the western basin while the observation shows only little indication of this behaviour (e.g. the 7 TU isopleth in the surface layer). Since the horizontal circulation of the boundary current (sweeping low concentrations northward) is rather weak in the model this feature must be attributed to a too strong upwelling of the coast (pushing low concentration upward).

6.2 Radioactive carbon

Natural radiocarbon ^{14}C is continually produced by the interaction of ^{14}N and cosmic rays in the atmosphere from where it distributes in the carbon reservoirs. Although the natural

production rate has not remained constant on large time scales and an anthropogenic contribution has started by combustion of fossil fuels and nuclear tests we will assume here a steady state condition for ^{14}C which globally is governed by the natural production and radioactive decay. Because of its large lifetime (λ^{-1} = 8200 years) the average ^{14}C atom can penetrate the ocean but the time is still not large enough for complete mixing, so that more remote water masses (with respect to the circulation pattern) will have less ^{14}C in relation to ordinary carbon than water masses closer to the input region (the surface mixed layer). In this respect ^{14}C-simulations provide a test of the abyssal overturning in the model.

For the ^{14}C-simulations we thus looked at the stationary solution of (6.1), i.e. with $\partial_t C = 0$. The input in the upper layer is taken globally uniform with a flux of 8 m/year. We use upwind differences and solve the resulting system iteratively. The results are shown in Fig. 6.9 for the layers 2 to 5 (the upper layer is almost uniform). The isolines give the fraction which is lost by decay which roughly (i.e. ignoring diffusion effects and recirculation to the surface layer) may be converted to an apparent age of the water masses by multiplying with the lifetime. The simulations reproduce the general increase of the apparent age in the deep ocean down (i.e. from north to south) the Atlantic and up the Pacific with the "oldest" water in the western part of the North Pacific. A more detailed comparison with the observation of ^{14}C obtained by the GEOSECS programme reveals, however, that the abyssal overturning in the model is far too rapid. This may partly be attributed to the large vertical velocities at lateral boundaries discussed in Section 5.3.

In summary to the tracer simulations we conclude that the upper ocean circulation and exchange between the upper layer and the thermocline is reproduced fairly well (except for the up- and down-welling at lateral boundaries and the equatorial zone) whereas the exchange between the upper and the deep ocean is too rapid (partly due to the same inconsistencies).

7. A model for the seasonal boundary layer

Along the concept of Kraus and Turner (1967, hereafter KT), a one-dimensional model of the upper ocean has been designed which describes the ocean surface layer as cheap and simple way. The model refers to the following rough picture of upper ocean dynamics. Wind-generated turbulent kinetic energy mixes the uppermost layer more or less completely. A comparatively strong gradient just below the mixed layer - generated during the heating season - prevents energy and momentum to penetrate into the quiescent, stably stratified seasonal thermocline. During the cooling period the gradient decreases and the turbulent kinetic energy at the bottom of the mixed layer "entrain s" water against the buoyancy forces from the thermocline into the mixed layer. Thus, the center of mass of the water column is raised and so is the potential energy. On an annual time-scale the dominant feature of the time development of the upper ocean structure is its cyclic behaviou Since the annual atmospheric heat flux results in a net heating or cooling depending on the latitude of the locus under considerations advection must yield a relevant contribution to the dynamics of the upper ocean. This latter effect lies outside the scope of strictly one-dimensional models.

In generalization of the original KT-model the existence of an always self-similar profile throughout the mixed layer and the seasonal thermocline is assumed. Then, heat and potential

energy of the water column may be expressed in terms of a few profile parameters and dynamical equations for these parameters are derived from the relation between the time rate of change of heat and potential energy to the surface fluxes. In contrast to KT-models the seasonal thermocline is not given a static shape but is capable of ML-independent dynamics. In this section we describe the strictly one-dimensional version of the model.

It is assumed that the temperature profile of the upper ocean can be represented by

$$T(t,z) = \begin{cases} T_o(t) \;, & 0 > z > -h(t) \\ T_* + (T_o - T_*)\, e^{(z+h)/d} \;, & -h > z > -h_* \end{cases} \qquad (7.1)$$

with the three profile parameters: $T_o(t)$ as ML-temperature, $h(t)$ as the ML-depth, and $d(t)$ as the e-folding depth of the exponentially decaying profile in the seasonal thermocline. The deep ocean temperature $T_* = T(-h_*)$ is assumed to be constant; changes in T_* can easily be incorporated. There is one degree of freedom assigned to the seasonal thermocline which allows for changes in the gradient just below the ML

$$\partial_z T\big|_{z=-h} = (T_o - T_*)/d \qquad (7.2)$$

independent of ML-temperature T_o.

The validity of the temperature profile (7.1) has been tested against data from various weatherships. Several typical cases are demonstrated in Fig. 7.1. Each picture shows two profiles,

the observed one (which represents a weekly average) and its representation in terms of (7.1). The three model parameters were derived from the observations according to the following procedure. The mixed layer depth h was determined as the locus of largest gradient. All temperature values above h were averaged to yield the mixed layer temperature T_o. Finally, the temperature distribution below the mixed layer was fitted to the exponential part of (7.1) to determine d and T_*. In comparison to an overall least square fit of the whole observed profile, this partly subjective method is preferable: in particular, the overall least square fit systematically overestimates the mixed layer depth of the winter-time profiles - having a small gradient below the mixed layer - and consequently leads to significant misrepresentations of the relevant physical quantities, namely the heat and potential energy of the column. Fig. 7.1 demonstra that the chosen procedure leads to a satisfying agreement betwe observed and parameterized profiles.

The assumption that the profile (7.1) is valid at all times completely ignores the emergence of any secondary mixed layers. Particularly, the assumption that the profile always retains its exponential shape in the thermocline contradicts the genera accepted picture of ML-shallowing. According to this picture, the ML retreats to an "equilibrium-depth" and leaves its former shape as a fossile remnant behind. However, if the profile (7.1 is interpreted as an average of instantaneous profiles over a sufficiently large time ($\gtrsim$ 10d) it can be assumed that unresolv sub-scale processes act to restore the profile (7.1). In the dynamical equations the concept of an "equilibrium-depth" leads to the asymmetry of a "prognostic" and a "diagnostic" regime which will be discussed below.

Heat content and potential energy of the water column are defined as

$$\tilde{H} = \varrho_* c_p \int_{-h_*}^{0} T(t,z)\, dz$$

$$\tilde{E}_{pt} = -\alpha g \varrho_* \int_{-h_*}^{0} z\, T(t,z)\, dz \qquad (7.3a)$$

For convenience we introduce the new variables

$$H = \tilde{H}/\varrho_* c_p - h_* T_*, \qquad E_{pt} = \tilde{E}_{pt}/\alpha g \varrho_* - \tfrac{1}{2} h_*^2 T$$

instead of $\tilde{H}$, $\tilde{E}_{pt}$ and

$$\varphi_0 = T_o - T_*, \qquad \varphi_1 = h + d, \qquad \varphi_2 = d$$

instead of T_o, h, d. In terms of the new variables, and assuming that always $h_* >> h + d$ so that exponential terms from the integrals (7.3a) may be dropped, heat and potential energy become

$$H = \varphi_0 \varphi_1, \qquad E_{pt} = \tfrac{1}{2} \varphi_0 (\varphi_1^2 + \varphi_2^2) \qquad (7.3b)$$

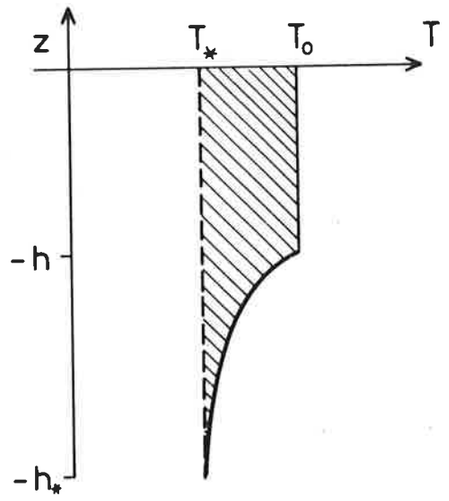

The interpretation of the variables H and E_{pt} can be seen from the diagram. While the whole area enclosed by the profile and the z-axis represents $\tilde{H}$ (up to a factor), the shaded region is equal to H. The analogous representation holds for $\tilde{E}_{pt}$ and E_{pt}. The form of (7.3) now suggests the following interpretation: the heat of the system is concentrated in a "mixed layer" of temperature φ_0 and depth $\varphi_1 = h + d$, while the potential energy is represented by the potential energy of this "mixed layer" plus the potential energy of an additional "mixed layer" having the same temperature φ_0 as the first one but depth $\varphi_2 = d$.

The dynamics of the system are now obtained from

$$\dot{H} = Q \tag{7.4}$$

$$\dot{E}_{pt} = W$$

where Q denotes the external heat fluxes, while W is related to the "mixing energy". However, (7.4) yield only two equations for three unknowns. Thus, an additional closure hypothesis is necessary. Observations of wind-driven ocean-surface layers suggest an ansatz

$$\dot{d} = - \text{const } \dot{h}$$

This expression assumes that a wind-induced deepening leads to a steepening of the gradient below the mixed layer. Allowing

additional for changes in d with respect to the mixed layer temperature and rewriting the ansatz in terms of the dynamical variables, the "closure hypothesis" reads

$$\dot{\varphi}_2 = - \alpha_0 \dot{\varphi}_0 - \alpha_1 \dot{\varphi}_1 \tag{7.5a}$$

where α_0 and α_1 denote model-parameters to be determined from the data. Thus, the complete system of dynamical equations describing mixed-layer deepening consists of (7.5a) and

$$\dot{\varphi}_0 = 2 \frac{W - Q(\varphi_1 + \alpha_1 \varphi_2)}{\varphi_2^2 - 2\varphi_2(\alpha_0 \varphi_0 - \alpha_1 \varphi_1) - \varphi_1^2} \tag{7.5b}$$

$$\dot{\varphi}_1 = (Q - \varphi_1 \dot{\varphi}_0) / \varphi_0 \tag{7.5c}$$

which follow from (7.4).

During retreat of the mixed layer the system (7.5) cannot apply as it would describe "unmixing" in violation of the second law of thermodynamics. That situation occurs if the kinetic energy input is too small to compensate the change in potential energy during heating, i.e. $W < hQ/2$. We assume that a new mixed layer is formed with the equilibrium-depth

$$h_e = 2W/Q \tag{7.6a}$$

The change in mixed-layer temperature is calculated from

$$\dot{\varphi}_0 = Q / h_e \qquad (7.6b)$$

In the thermocline, it is assumed that the exponential profile is restored while the heat content under the new mixed layer is conserved. That can be achieved only if some unspecified turbulent kinetic energy is available to account for the change in potential energy. The heat budget can be written in discrete form as

$$H^n = H^o + Q\,\Delta t \qquad (7.6c)$$

where H^n, H^o is the heat content calculated with the new resp. old values for T_o, h, d. Eq. (7.6c) is used to calculate the new value for the variable $d = \varphi_2$. The diagnostic system (7.6) replaces the prognostic system (7.5) whenever the condition $W < hQ/2$ is satisfied. The integration of (7.5) resp. (7.6) is only numerically possible.

The tuning and verification of the model is performed by comparison of the time behaviour of (7.5) with weathership data. The forcing terms Q(t) and W(t) are then usually represented by the well-known bulk expressions, which, however, suffer several shortcomings. In particular, the radiative heatflux, combined from solar and infrared radiation, is expressed in terms of climatic values, referring to cloudless skies. Since no data on cloud coverage are available, representations of this kind always imply a high degree of arbitrariness. Moreover, the penetration of radiation into

the ocean is usually treated as a δ-like surface effect or represented by one, finite penetration-depth for all frequencies. Even more severe uncertainties occur for the bulk expressions of the turbulent fluxes, i.e. latent and sensible heat flux. For a detailed discussion of the bulk heat fluxes see Bunker (1976). The main objection against the use of the bulk expressions in tuning a one-dimensional model arises from the viewpoint of global heat transport. A one-dimensional model, being perfectly tuned to atmospheric heat fluxes, in fact annihilates advective effects.

To obtain an appropriate heat flux for the tuning of (7.5) and (7.6) the observed temperature profiles were therefore integrated with respect to z and the resulting H(t) was differentiated with respect to time. By this procedure, changes in heat content due to atmospheric fluxes and due to advection are both included.

The kinetic energy input at the surface is represented in terms of the applied wind stress

$$\tau = \rho_a u_*^2 \qquad (7.7)$$

where ρ_a denotes the density of air and u_* is the friction velocity which is defined by the wind velocity at 10 m above sea surface u_{10},

$$u_*^2 = c_{10}\, u_{10}^2$$

For a detailed discussion of the drag coefficient c_{10} see Bunker (1976). Then, from the condition of continuity of

stress at the air-sea interface

$$W \sim \rho_a U_{10}^3 C_{10}^{3/2} (\rho_a/\rho_*)^{1/2}$$

is derived as a scale expression for the mechanical energy input. The energy, available for vertical turbulent mixing should be comparable to this expression in order of magnitude, i.e. the "mixing energy" is assumed to be expressable as

$$\tilde{W}_0(t) = \frac{\alpha_2 \rho_a}{\alpha_g \rho_*} U_{10}^3 C_{10}^{3/2} (\rho_a/\rho_*)^{1/2} e^{-h(t)/\alpha_3} \qquad (7.8)$$

where α_2 is the "mixing parameter" of order 1 and an additional penetration of mixing energy to a characteristic depth α_3 has been introduced. α_2 and α_3 have to be determined from the data. Obviously (7.8) is strictly positive and its insertion into (7.5) leads to a continuous increase in potential energy, i.e. an infinitely deep mixed layer. This is in clear contradiction to the cyclic behaviour of the upper ocean structure. Hence, one has to introduce a mechanism that allows the system to loose potential energy. In physical terms this may be called a "dissipation of turbulent kinetic energy". Several possible parameterizations of dissipation have been reviewed by Stevenson (1978). Here we adopt an approach suggested by Gill and Turner (1975). They assume that only a small part of the convectively generated turbulent kinetic energy contributes to changes in E_{pt}. The assumption implies that wind- and convectively generated turbulence dissipate in different ways. Thus, (7.8) is modified to

$$W(t) = \tilde{W}_0(t) + \tfrac{1}{2}(1-\alpha_4)\varphi_1 Q \cdot \Theta(-Q) \qquad (7.9)$$

where $\Theta(-Q)$ denotes the unit-step function. The model parameter α_4 measures the part of convectively generated turbulence that contributes to changes in E_{pt}. If $\alpha_4 = 1$ all convectively generated turbulence does, if $\alpha_4 = 0$ none does. Laboratory observations suggest a value for α_4 of order 0.15. Its exact value will be determined from ocean data.

The model has now 5 model parameters $\alpha_0 \ldots \alpha_4$ which are determined by tuning (7.5) resp. (7.6) to time series of temperature profiles observed at weatherships. Fig. 7.2 shows a fit to temperature-profiles measured at weathership ECHO. The timeseries covers one annual cycle with a weekly time step. The values of the model parameters determined thus are $\alpha_0 = 3$ m/°K, $\alpha_1 = .08$, $\alpha_2 = 1$, $\alpha_3 = 50$ m, $\alpha_4 = .15$. The model is capable to exhibit all features of the data, in particular it gives an almost constant value for d and yields a cyclostationary behaviour of the system. This is represented in Fig. 7.3, where the heat of the water column is plotted against sea surface temperature and potential energy of the column.

Literature

Arakawa, A., and V.R. Lamb: Computational Design of the Basic Dynamical Processes of the UCLA General Circulation Model. Meth. Comp. Phys. 16, 173-263, 1977.

Bryan, K., and M.D. Cox: The circulation of the world ocean: A numerical study, 1, A homogeneous model. J.Phys. Oceanogr. 2, 319-335, 1972.

Bryan, K., and L.J. Lewis: A water mass model of the world ocean. J.Geophys.Res. 84, 2503-2517, 1979.

Bunker, A.: Computations of surface energy flux and annual air-sea interaction cycles over the North Atlantic Ocean. Mon.Wea.Rev. 104, 1122-1140, 1976.

Fine, A.F., J.L. Reid, and H.G. Östlund: Circulation of tritium in the Pacific Ocean. J.Phys.Oceanogr. 11, 3-14, 1981.

Friedrich, H., and S. Levitus: An approximation to the equation of state for Sea Water, suitable for numerical ocean models. 3. Phys. Ocean. 2, 514-517, 1972.

Gill, A.E., and J.S. Turner: A comparison of seasonal thermocline models with observation. Deep-Sea Res. 23, 391-401, 1975.

Grotjahn, R., and J.J. O'Brien: Some inaccuracies in finite differencing hyperbolic equations. Mon.Wea.Rev. 104, 180-194, 1976.

Hasselmann, K., An ocean model for climate variability studies. Prog.Oceanog. 11, 69-92, 1982.

Hellerman, S.: An updated estimate of the wind stress on the world ocean. Mon.Wea.Rev. 95, 606-626, 1967.

Kraus, E.B., and J.S. Turner: A one-dimensional model of the seasonal thermocline. Tellus 19, 88-106, 1967.

Levitus, S., and H.A. Oort: Global analysis of oceanographic data. Bull.Am.Meteorol.Soc. 58, 1270-1284, 1977.

Maier-Reimer, E.: Hydrodynamisch-numerische Untersuchungen zu horizontalen Ausbreitungs- und Transportvorgängen in der Nordsee. Mitt.Inst.f.Meer. 21, 56 pp, Hamburg, 1973.

Östlund, H.G., H.G. Dorsey, and R. Brescher: GEOSECS Atlantic radiocarbon and tritium results (Miami), Rosenstiel Sch.Mar.Atmos.Sci., Univ.Miami, Data Rep. No. 5, 1976.

Östlund, H.G., and R.A. Fine: Oceanic distribution and transport of tritium, in: The Behaviour of Tritium in the Environment (International Atomic Energy Agency, Vienna, 1979), 303-314, 1979.

Rhines, P.B.: The dynamics of unsteady currents, in: The Sea, Vol. 6, 189-318, N.Y., 1977.

Robinson, M., R.A. Bauer, and E.H. Schroeder: Atlas of the North Atlantic-Indian Ocean monthly mean temperatures and mean salinities of the surface layer. Naval Oceanog. Off., Ref. Pub. 18, Washington, D.C., 243 pp, 1979.

Sarmiento, J.L.: A three-dimensional simulation of tritium distribution in the Atlantic ocean, 1982 (in preparation).

Sarmiento, J.L., J. Willebrand, and S. Hellerman: Objective analysis of tritium observations in the Atlantic Ocean during 1971-1974. Tech.Rep. 1, Ocean Tracers Lab., Dept. of Geological and Geophysical Sciences, Princeton University, New Jersey, 1982.

Stevenson, J.W.: On the effect of dissipation on seasonal thermocline models. J.Phys.Oceanogr. 9, 57-64, 1979.

Weiss, W., W. Roether, and E. Dreisigacker: Tritium in the North Atlantic Ocean: inventory, input and transfer into the deep water, in: The Behaviour of Tritium in the Environment (International Atomic Energy Agency, Vienna, 1979), 315-336, 1979.

Weiss, W., and W. Roether: The rates of tritium input to the world oceans. Earth and Planetary Sci. Letters 49, 435-446, 1980.

Figure captions

Fig. 4.1 Contours of depth h and f/h.

Fig. 4.2 Contours of stability parameter λ from eq. (4.14).

Fig. 5.1 Wind-stress distribution according to Hellerman (1967).

Fig. 5.2a Temperature and salinity at 75 m-level. Observed (= initial) distribution.

Fig. 5.2b Temperature and salinity at 75 m-level. Distribution after 5 years of integration.

Fig. 5.2c Temperature and salinity at 75 m-level. Distribution after 20 years of integration.

Fig. 5.2d Temperature and salinity at 75 m-level. Distribution after 60 years of integration.

Fig. 5.3a Temperature and salinity at 150 m-level. Observed (= initial) distribution.

Fig. 5.3b Temperature and salinity at 150 m-level. Distribution after 5 years of integration.

Fig. 5.3c Temperature and salinity at 150 m-level. Distribution after 20 years of integration.

Fig. 5.3d Temperature and salinity at 150 m-level. Distribution after 60 years of integration.

Fig. 5.4a Temperature and salinity at 300 m-level. Observed (= initial) distribution.

Fig. 5.4b Temperature and salinity at 300 m-level. Distribution after 5 years of integration.

Fig. 5.4c Temperature and salinity at 300 m-level. Distribution after 20 years of integration.

Fig. 5.4d Temperature and salinity at 300 m-level. Distribution after 60 years of integration.

Fig. 5.5a Temperature and salinity at 1000 m-level. Observed (= initial) distribution.

Fig. 5.5b Temperature and salinity at 1000 m-level. Distribution after 5 years of integration.

Fig. 5.5c Temperature and salinity at 1000 m-level. Distribution after 20 years of integration.

Fig. 5.5d Temperature and salinity at 1000 m-level. Distribution after 60 years of integration.

Fig. 5.6a Temperature and salinity at 3000 m-level. Observed (= initial) distribution.

Fig. 5.6b Temperature and salinity at 3000 m-level. Distribution after 5 years of integration.

Fig. 5.6c Temperature and salinity at 3000 m-level. Distribution after 20 years of integration.

Fig. 5.6d Temperature and salinity at 3000 m-level. Distribution after 60 years of integration.

Fig. 5.7 Location of sections 1, 2, 3, 40° N, Eq, and ACC.

Fig. 5.8a Temperature along section 1. Observed distribution and after 5 years of integration.

Fig. 5.8b Temperature along section 1. After 20 years and after 60 years of integration.

Fig. 5.8c Salinity along section 1. Observed distribution and after 5 years of integration.

Fig. 5.8d Salinity along section 1. After 20 years and after 60 years of integration.

Fig. 5.9a Temperature along section 2. Observed distribution and after 5 years of integration.

Fig. 5.9b Temperature along section 2. After 20 years and after 60 years of integration.

Fig. 5.9c Salinity along section 2. Observed distribution and after 5 years of integration.

Fig. 5.9d Salinity along section 2. After 20 years and after 60 years of integration.

Fig. 5.10a Temperature along section 3. Observed distribution and after 5 years of integration.

Fig. 5.10b Temperature along section 3. After 20 years and after 60 years of integration.

Fig. 5.10c Salinity along section 3. Observed distribution and after 5 years of integration.

Fig. 5.10d Salinity along section 3. After 20 years and after 60 years of integration.

Fig. 5.11a Temperature along section 40°N. Observed distribution and after 5 years of integration.

Fig. 5.11b Temperature along section 40°N. After 20 years and after 60 years of integration.

Fig. 5.11c Salinity along section 40°N. Observed distribution and after 5 years of integration.

Fig. 5.11d Salinity along section 40°N. After 20 years and after 60 years of integration.

Fig. 5.12a Temperature along section Eq. Observed distribution and after 5 years of integration.

Fig. 5.12b Temperature along section Eq. After 20 years and after 60 years of integration.

Fig. 5.12c Salinity along section Eq. Observed distribution and after 5 years of integration.

Fig. 5.12d Salinity along section Eq. After 20 years and after 60 years of integration.

Fig. 5.13a Temperature along section ACC. Observed distribution and after 5 years of integration.

Fig. 5.13b Temperature along section ACC. After 20 years and after 60 years of integration.

Fig. 5.13c Salinity along section ACC. Observed distribution and after 5 years of integration.

Fig. 5.13d Salinity along section 3. After 20 years and after 60 years of integration.

Fig. 5.14 Time series of temperature at 1°N on the section 1 for different levels.

Fig. 5.15 Time series of temperature at 20° N on the section 1 for different levels.

Fig. 5.16a Horizontal velocity at 75 m-level after 60 years of integration.

Fig. 5.16b Horizontal velocity at 150 m-level after 60 years of integration.

Fig. 5.16c Horizontal velocity at 300 m-level after 60 years of integration.

Fig. 5.16d Horizontal velocity at 1000 m-level after 60 years of integration.

Fig. 5.16e Horizontal velocity at 3000 m-level after 60 years of integration.

Fig. 5.16f Horizontal barotropic velocity after 60 years of integration.

Fig. 5.17a Horizontal velocity at 75 m-level. Average over 60 years to 65 years integration period.

Fig. 5.17b Horizontal velocity at 150 m-level. Average over 60 years to 65 years integration period.

Fig. 5.17c Horizontal velocity at 300 m-level. Average over 60 years to 65 years integration period.

Fig. 5.17d Horizontal velocity at 1000 m-level. Average over 60 years to 65 years integration period.

Fig. 5.17e Horizontal velocity at 3000 m-level. Average over 60 years to 65 years integration period.

Fig. 5.17f Horizontal barotropic velocity. Average over 60 years to 65 years integration period.

Fig. 5.18a Vertical velocity at 112 m-level after 60 years of integration.

Fig. 5.18b Vertical velocity at 225 m-level after 60 years of integration.

Fig. 5.18c Vertical velocity at 650 m-level after 60 years of integration.

Fig. 5.18d Vertical velocity at 2000 m-level after 60 years of integration.

Fig. 5.19a Vertical velocity at 112 m-level. Average over 60 years to 65 years integration period.

Fig. 5.19b Vertical velocity at 225 m-level. Average over 60 years to 65 years integration period.

Fig. 5.19c Vertical velocity at 650 m-level. Average over 60 years to 65 years integration period.

Fig. 5.19d Vertical velocity at 2000 m-level. Average over 60 years to 65 years integration period.

Fig. 5.20a Time series of vertical velocity at 20^{o} N on section 1 for different levels.

Fig. 5.20b Time series of vertical velocity at 1^{o} N on section 1 for different levels.

Fig. 5.21a Numerical vertical diffusivity at 112 m-level computed for the 60 years velocity field.

Fig. 5.21b Numerical vertical diffusivity at 225 m-level computed for the 60 years velocity field.

Fig. 5.21c Numerical vertical diffusivity at 650 m-level computed for the 60 years velocity field.

Fig. 5.21d Numerical vertical diffusivity at 2000 m-level computed for the 60 years velocity field.

Fig. 6.1 Tritium in rainfall at ~ 50^{o} N (Weiss et al., 1979). This illustrates the temporal pattern of the input to the oceans.

Fig. 6.2 Total input of tritium to the ocean up to 1972. The figure shows the contributions of open ocean input, river runoff, and water vapor transport from continents.

Fig. 6.3a Tritium at 75 m- and 150 m-level for 1972. Diffusive simulation.

Fig. 6.3b Tritium at 300 m- and 1000 m-level for 1972. Diffusive simulation.

Fig. 6.4 Tritium along section 3 for 1972. Diffusive simulation.

Fig. 6.5a Observed tritium concentration at the surface. (Fine et al., 1981).

Fig. 6.5b North-south section of tritium in the western Pacific (Fine et al., 1981).

Fig. 4.1 Contours of depth h and f/h.

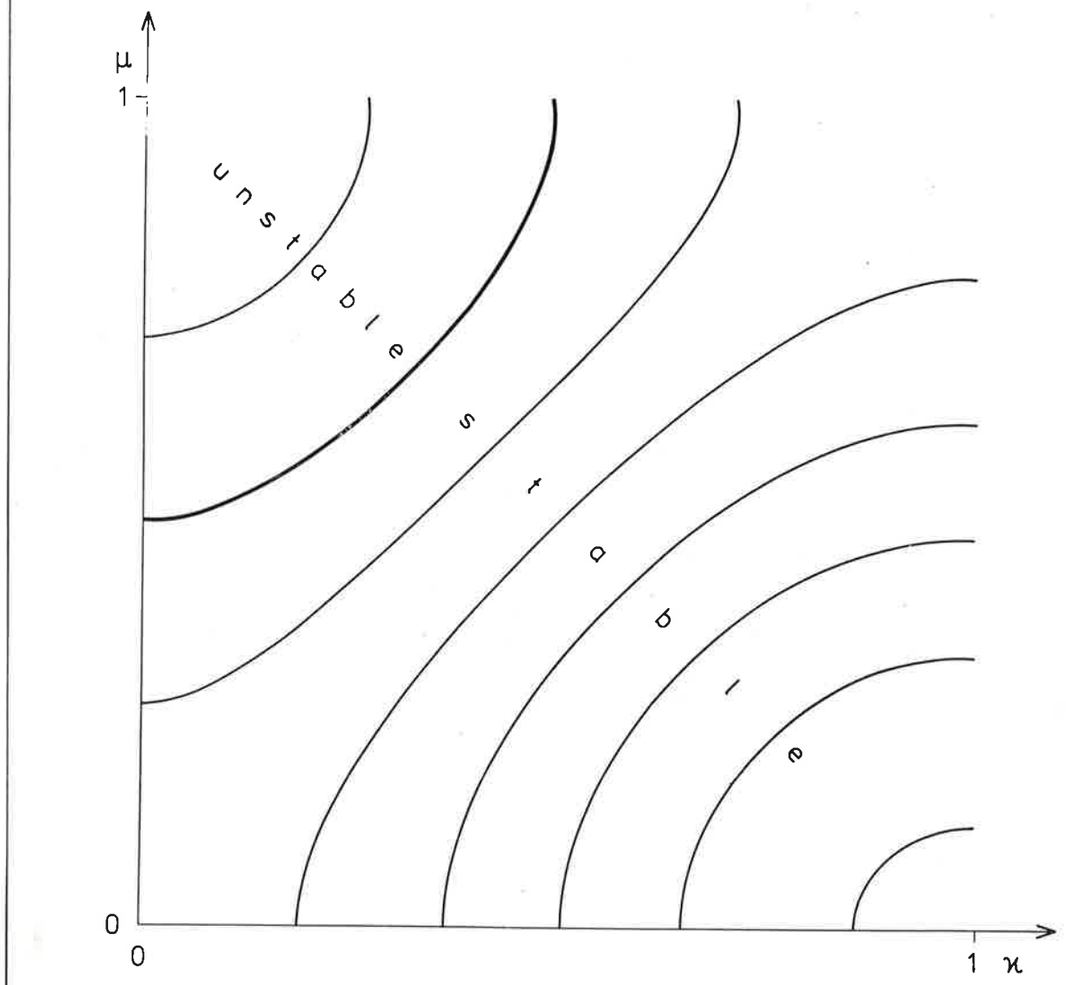

Fig. 4.2 Contours of stability parameter λ from eq. (4.14).

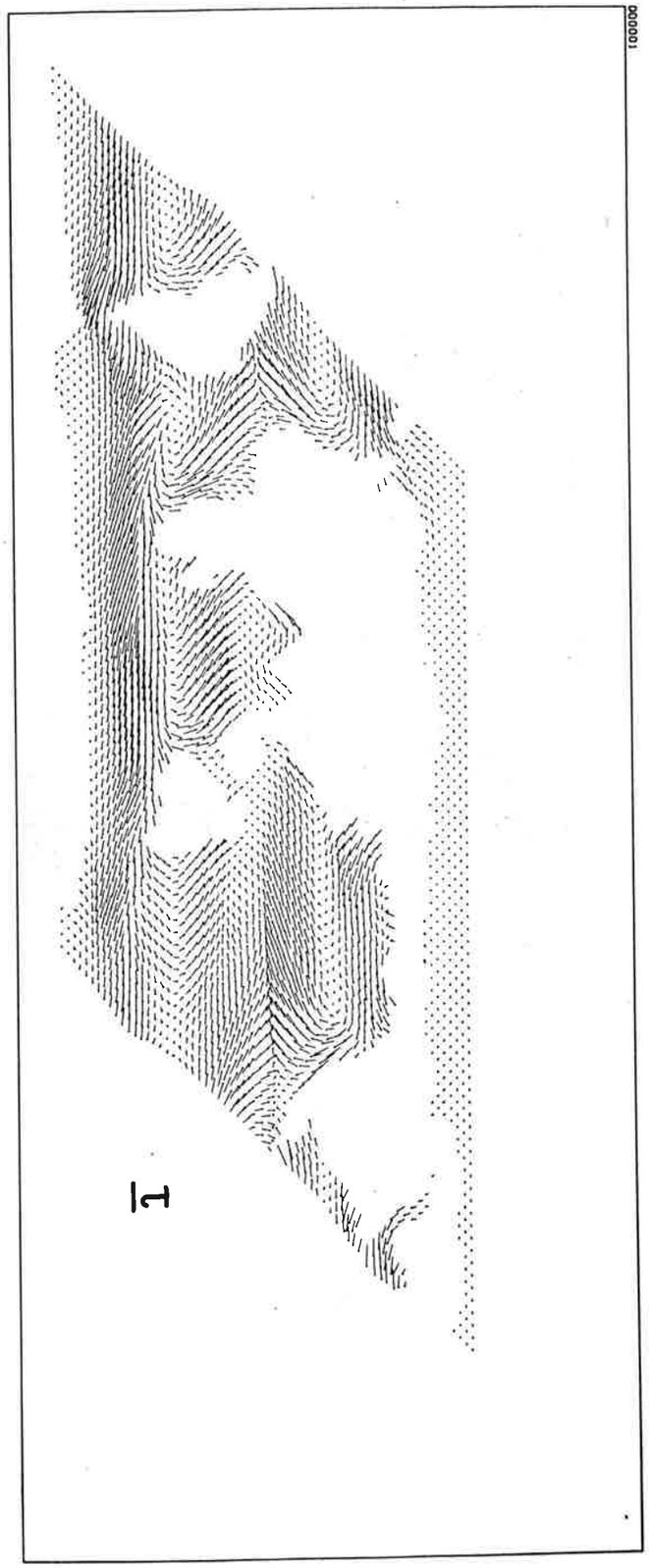

Fig. 5.1 Wind-stress distribution according to Hellerman (1967).

Fig. 5.2a Temperature and salinity at 75 m-level. Observed (= initial) distribution.

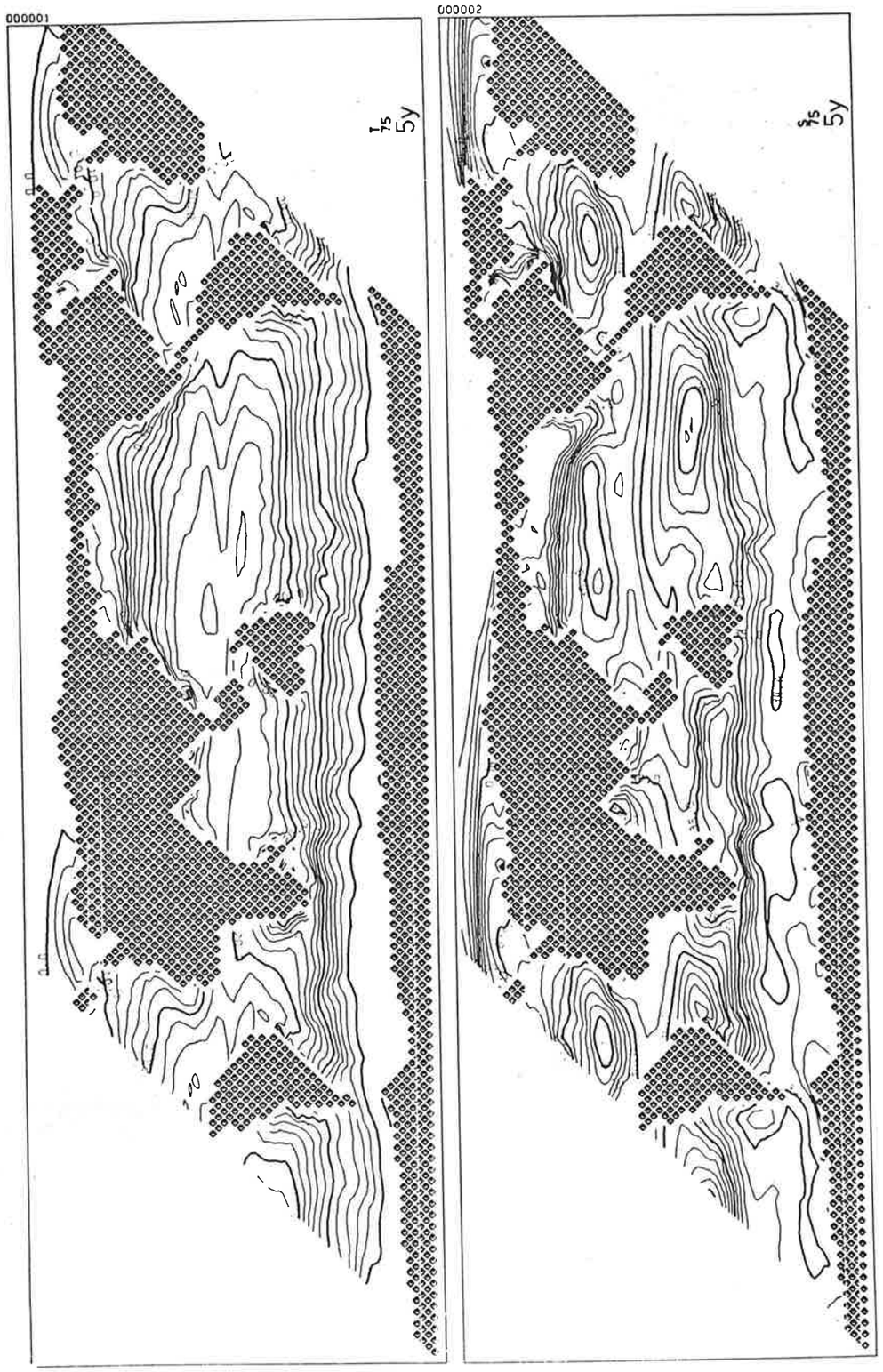

Fig. 5.2b Temperature and salinity at 75 m-level.
Distribution after 5 years of integration.

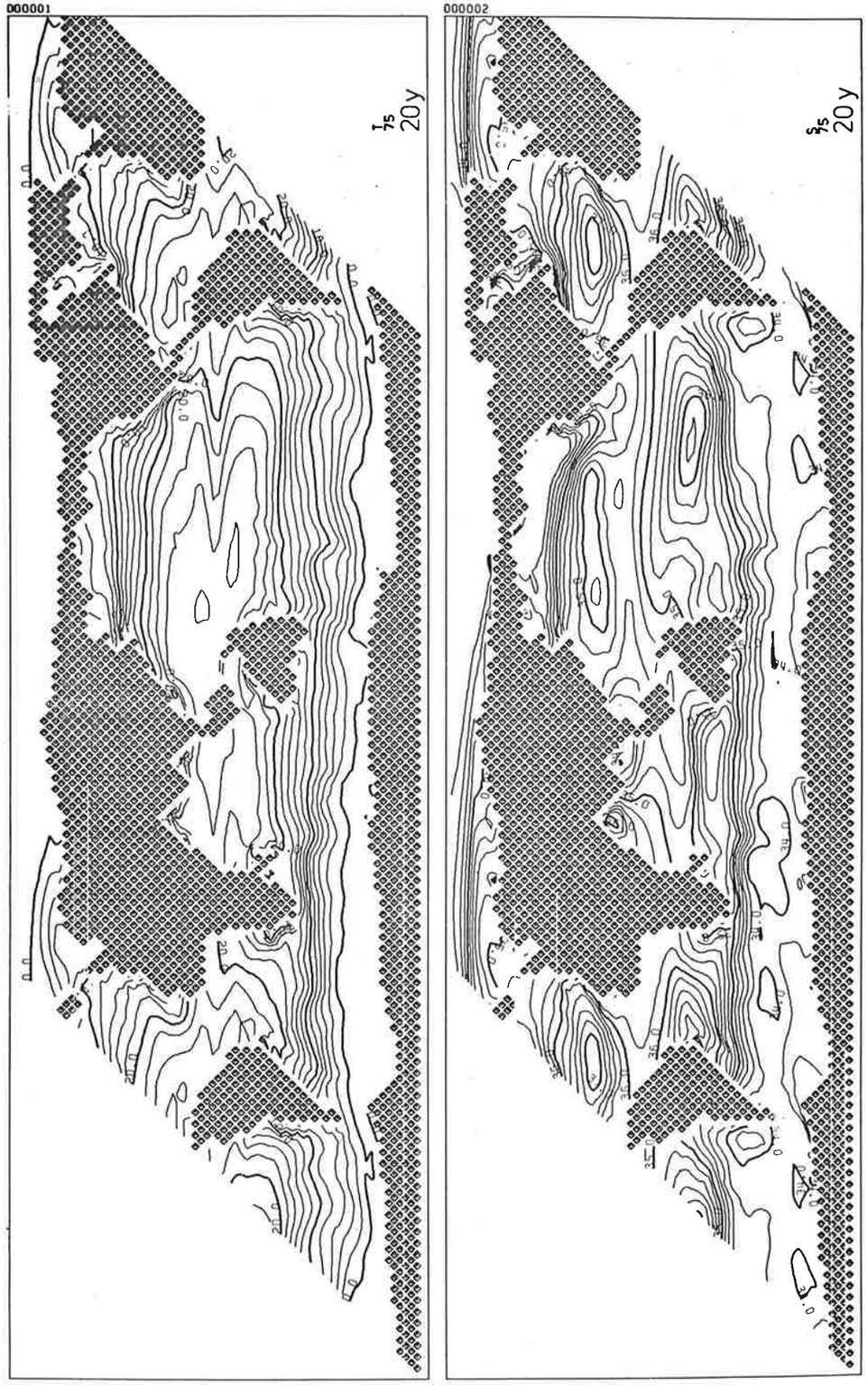

Fig. 5.2c Temperature and salinity at 75 m-level.
Distribution after 20 years of integration.

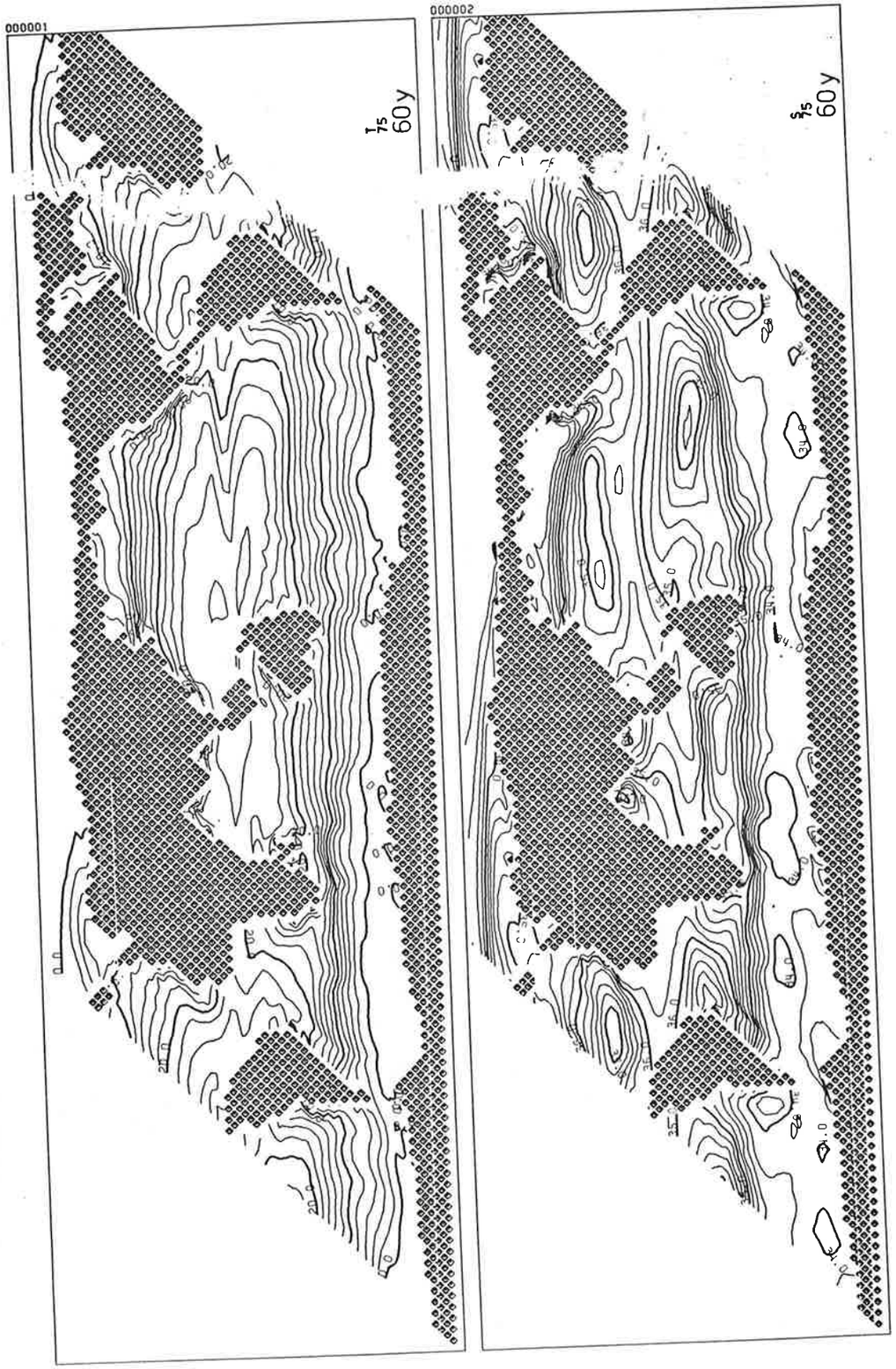

Fig. 5.2d Temperature and salinity at 75 m-level.
Distribution after 60 years of integration.

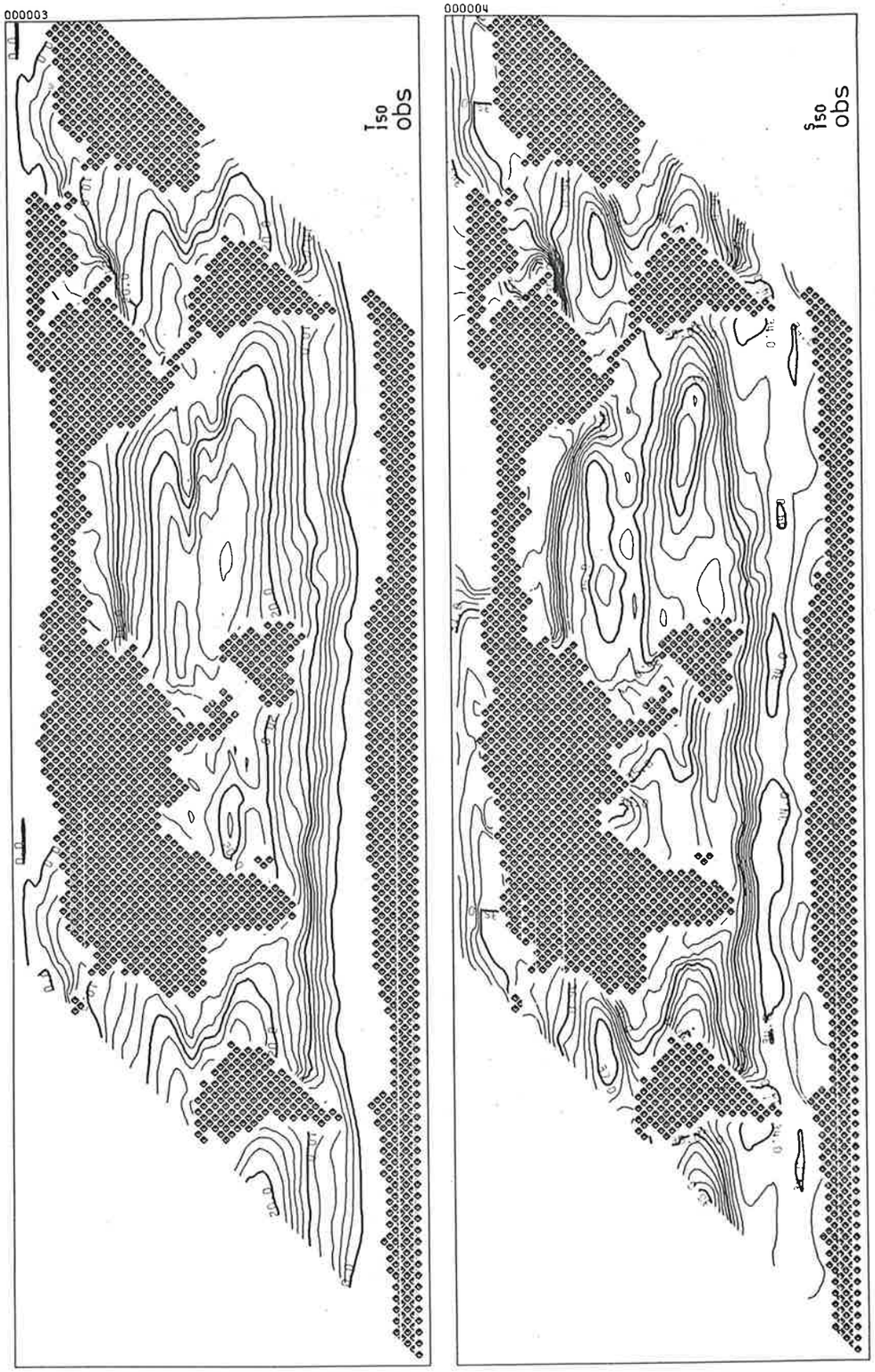

Fig. 5.3a Temperature and salinity at 150 m-level.
Observed (= initial) distribution.

Fig. 5.3b Temperature and salinity at 150 m-level.
Distribution after 5 years of integration.

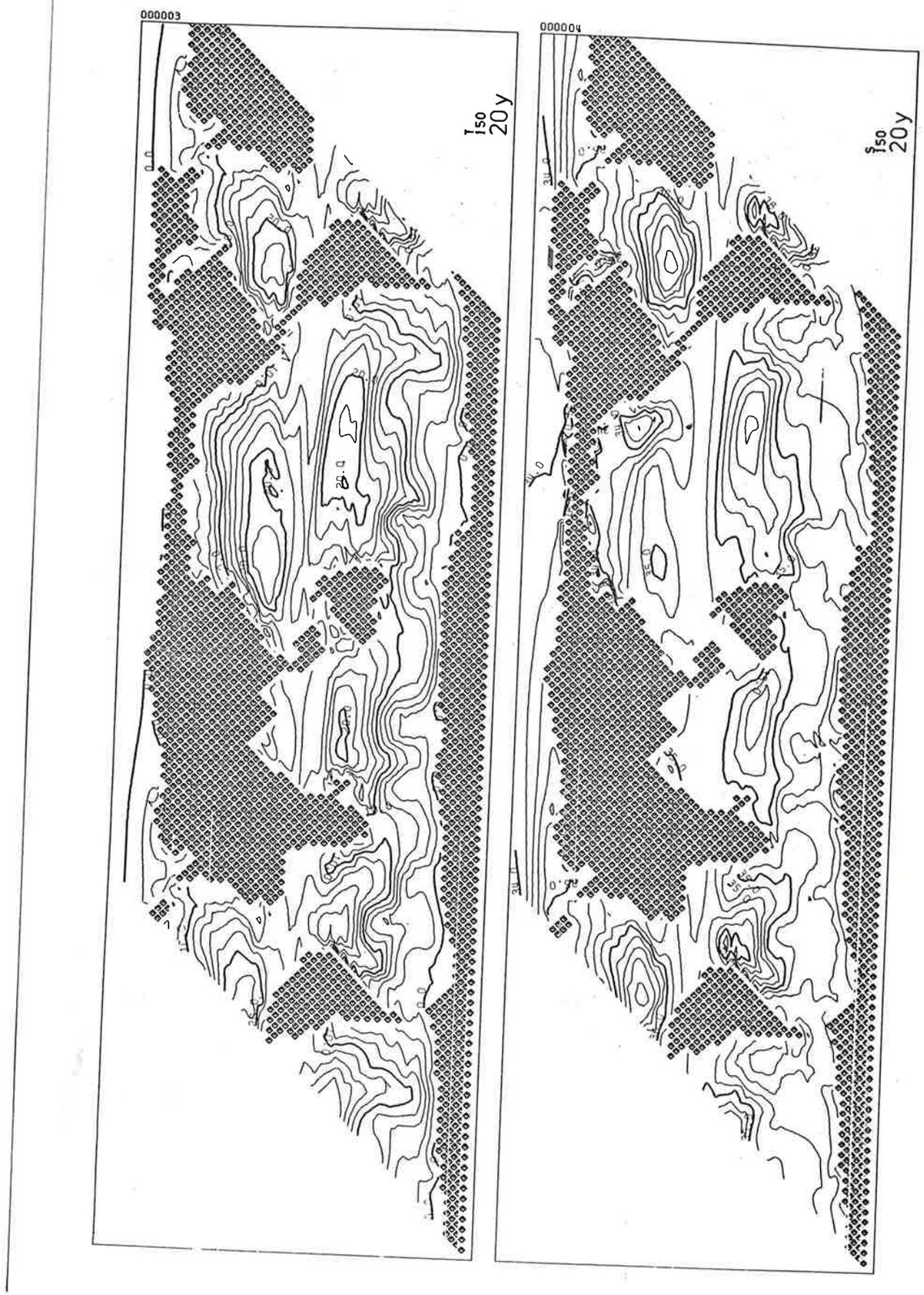

Fig. 5.3c Temperature and salinity at 150 m-level.
Distribution after 20 years of integration.

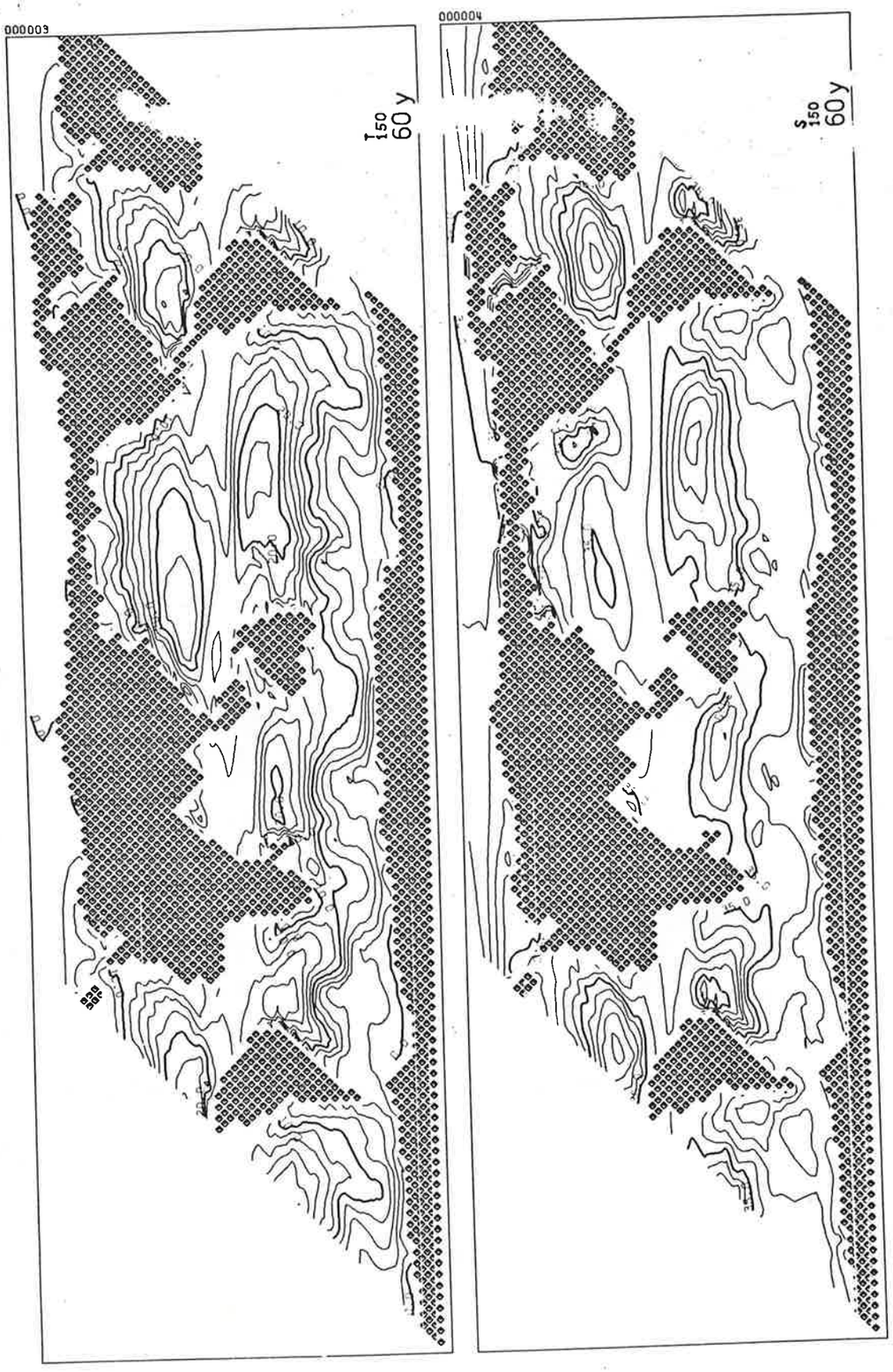

Fig. 5.3d Temperature and salinity at 150 m-level.
Distribution after 60 years of integration.

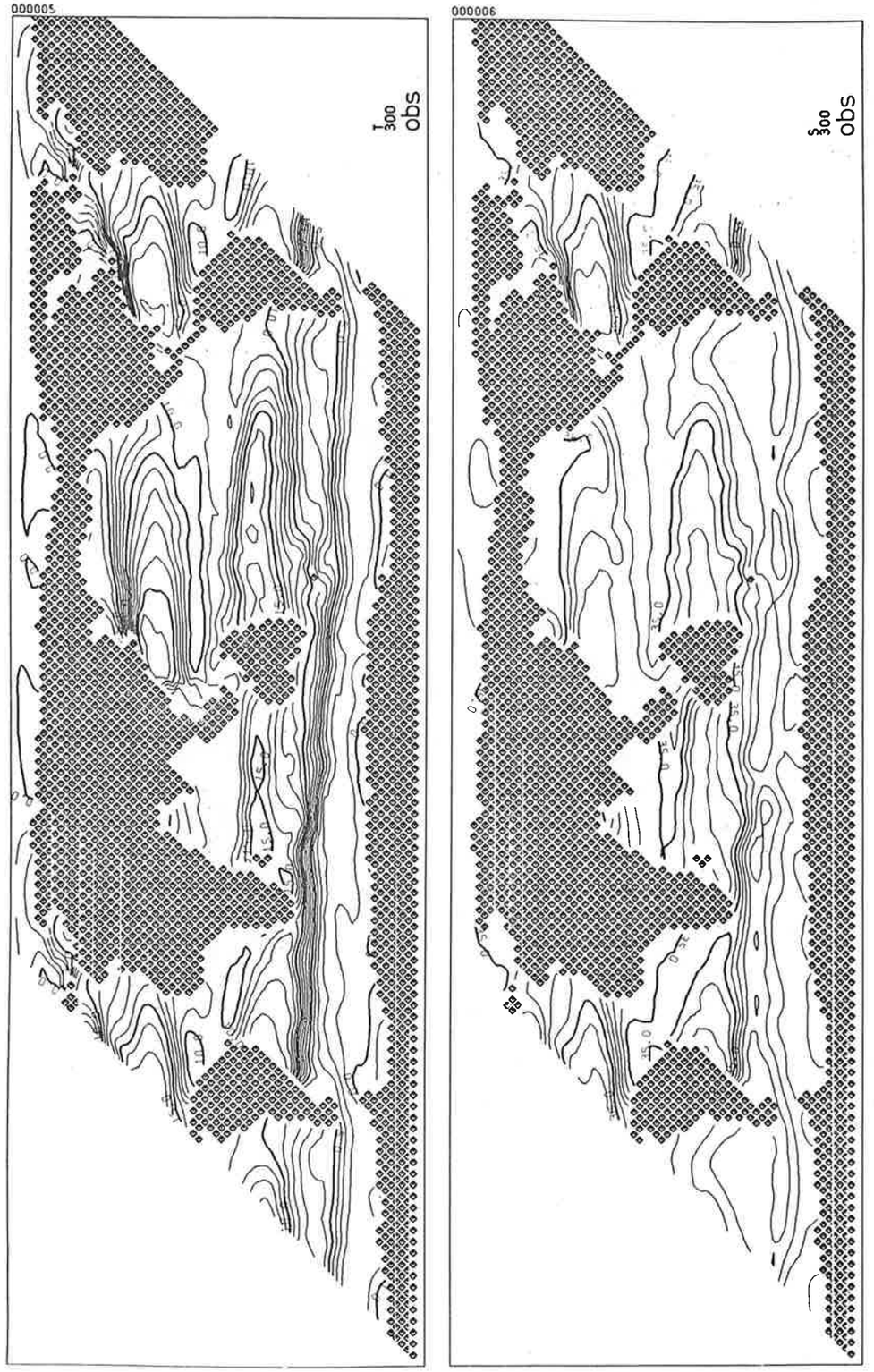

Fig. 5.4a Temperature and salinity at 300 m-level.
Observed (= initial) distribution.

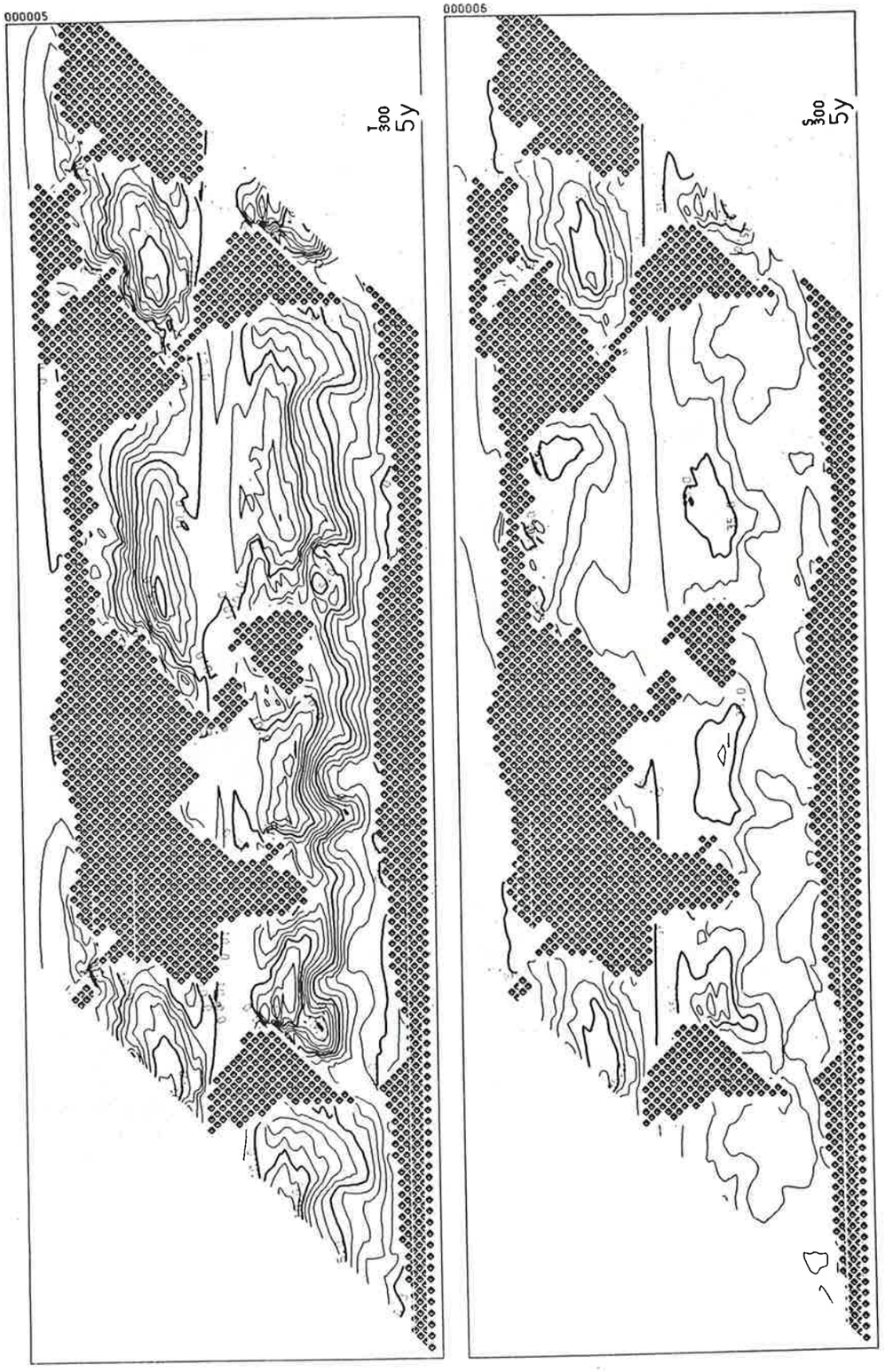

Fig. 5.4b Temperature and salinity at 300 m-level.
Distribution after 5 years of integration.

Fig. 5.4c Temperature and salinity at 300 m-level.
Distribution after 20 years of integration.

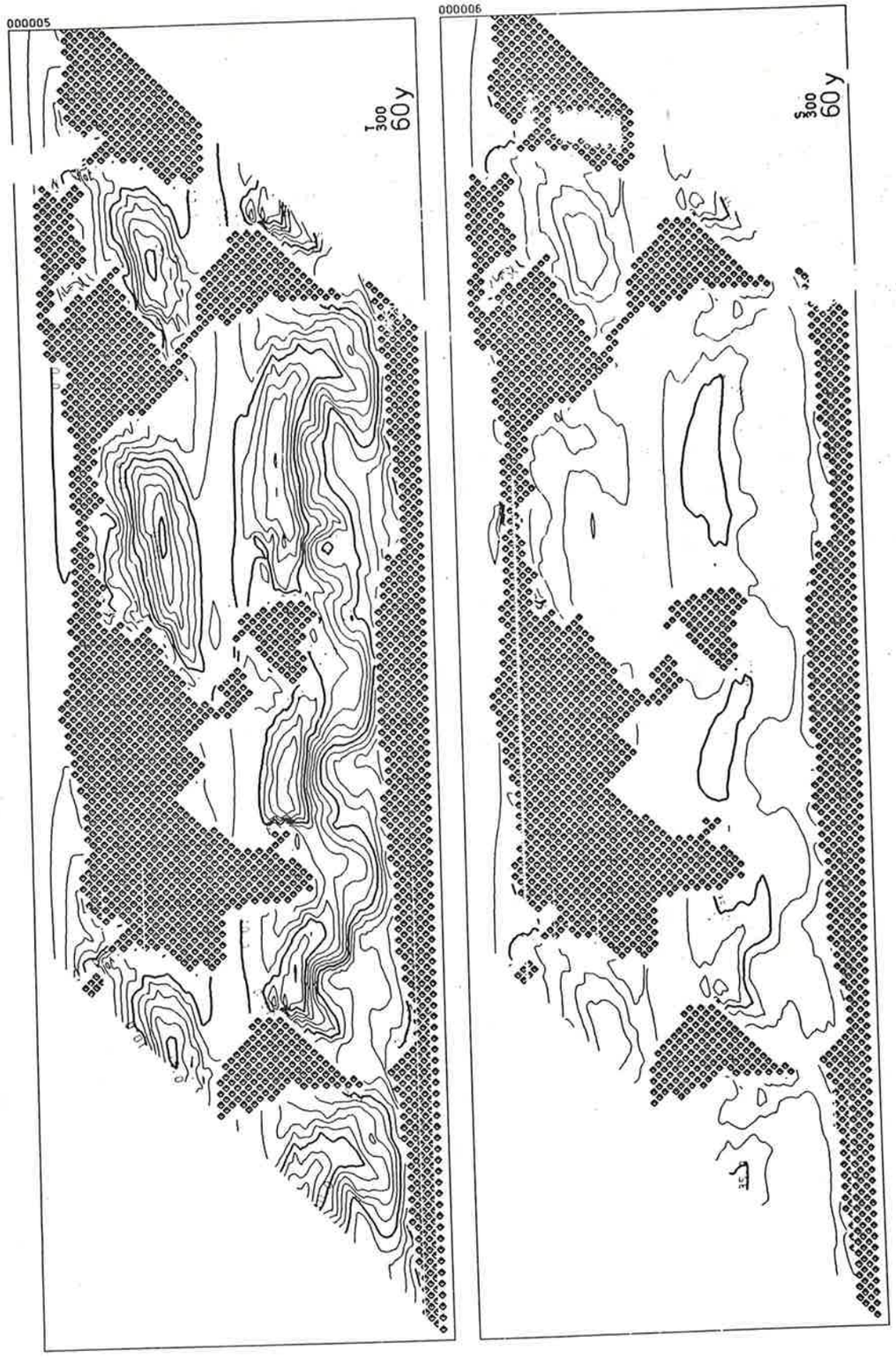

Fig. 5.4d Temperature and salinity at 300 m-level.
Distribution after 60 years of integration.

Fig. 5.5a Temperature and salinity at 1000 m-level.
Observed (= initial) distribution.

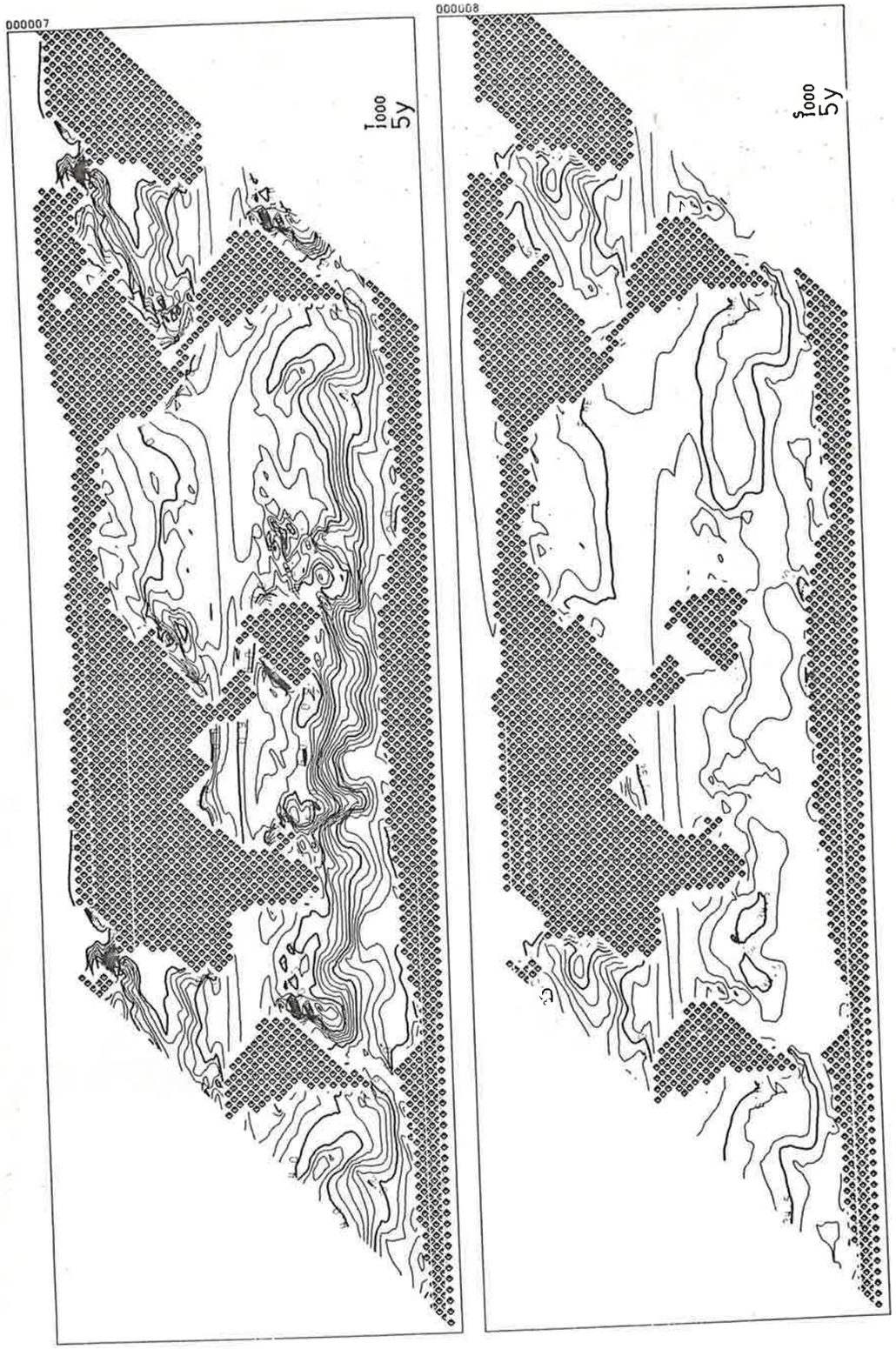

Fig. 5.5b Temperature and salinity at 1000 m-level.
Distribution after 5 years of integration.

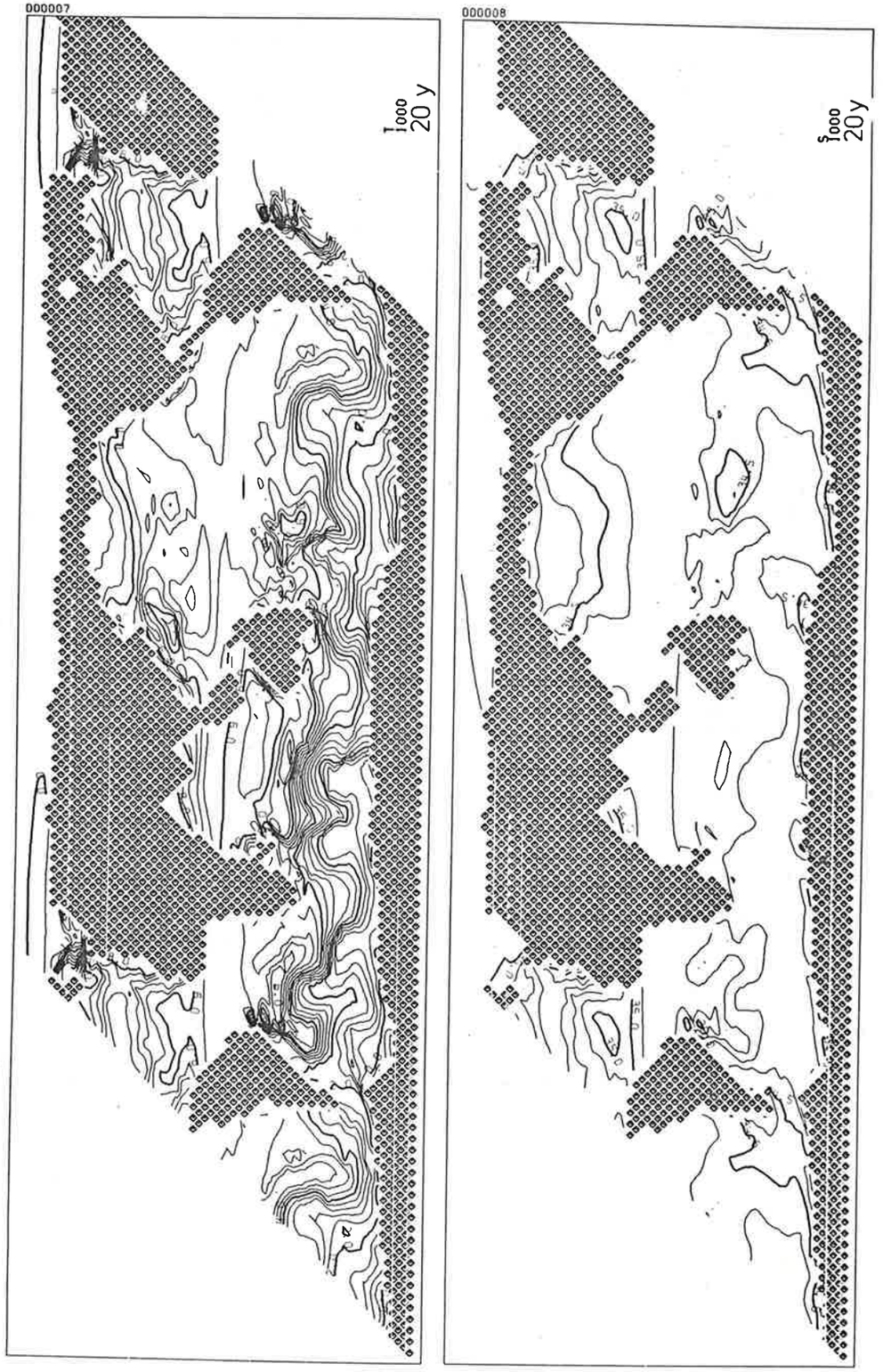

Fig. 5.5c Temperature and salinity at 1000 m-level.
Distribution after 20 years of integration.

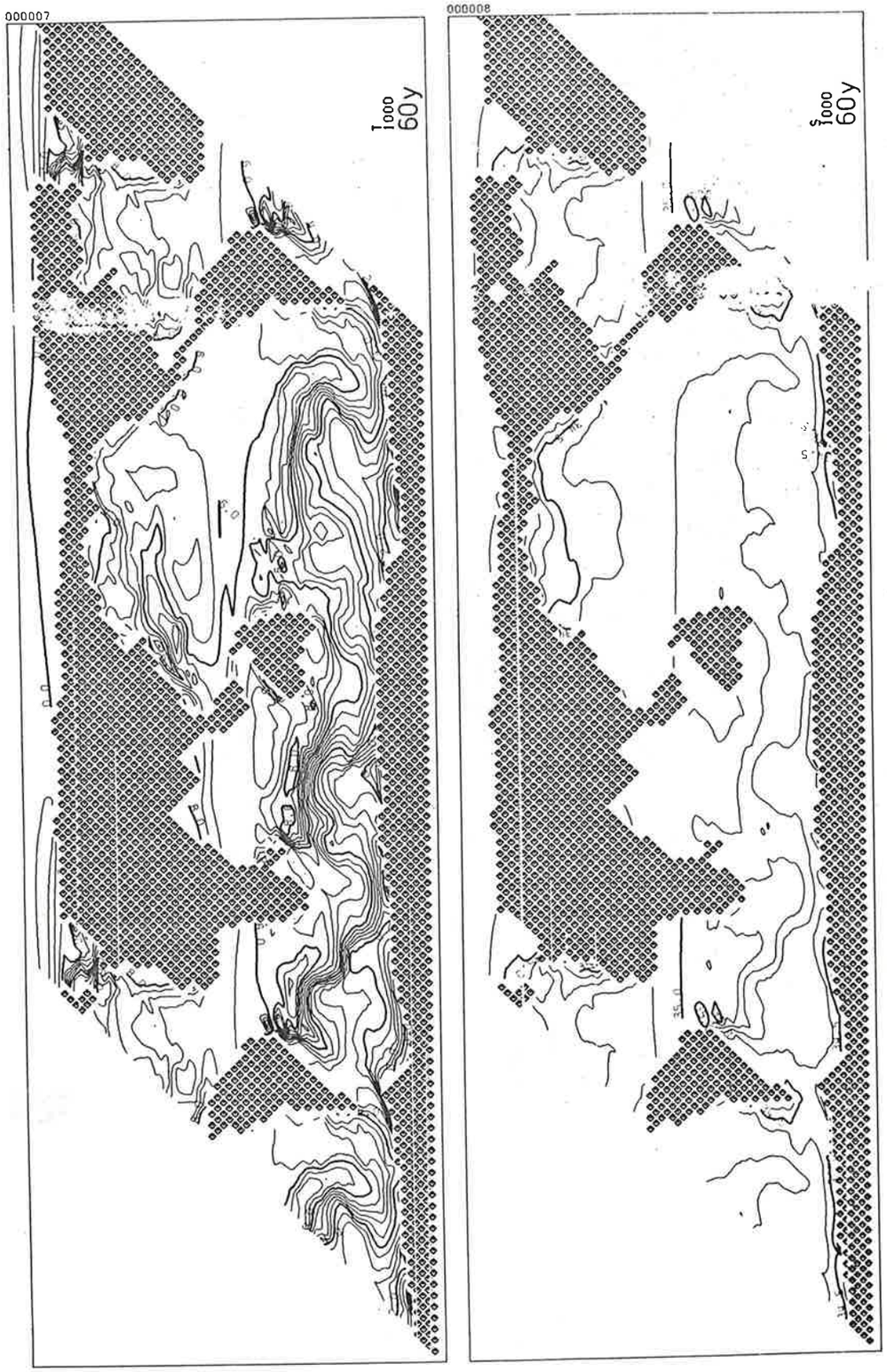

Fig. 5.5d Temperature and salinity at 1000 m-level.
Distribution after 60 years of integration.

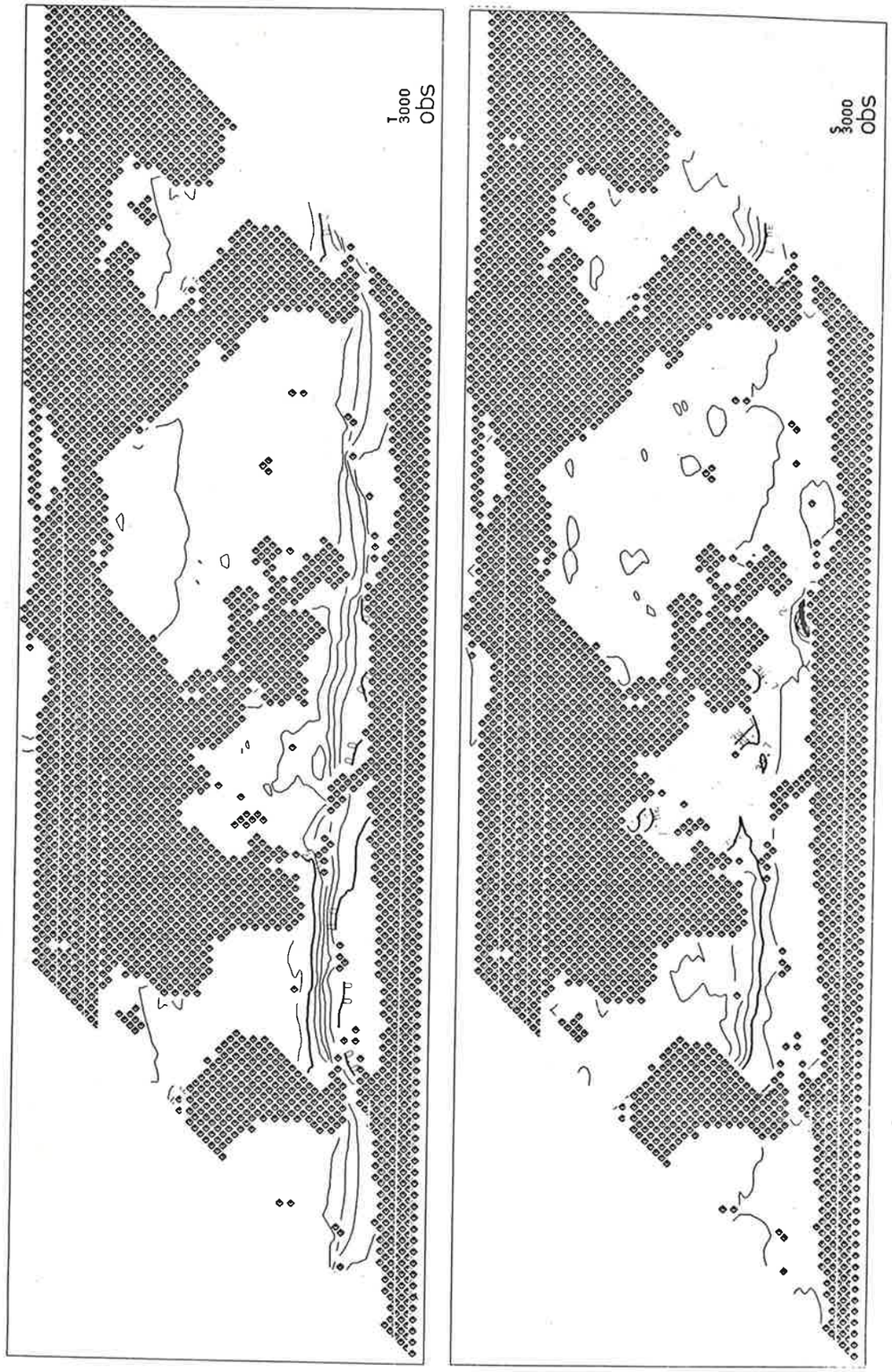

Fig. 5.6a Temperature and salinity at 3000 m-level.
Observed (= initial) distribution.

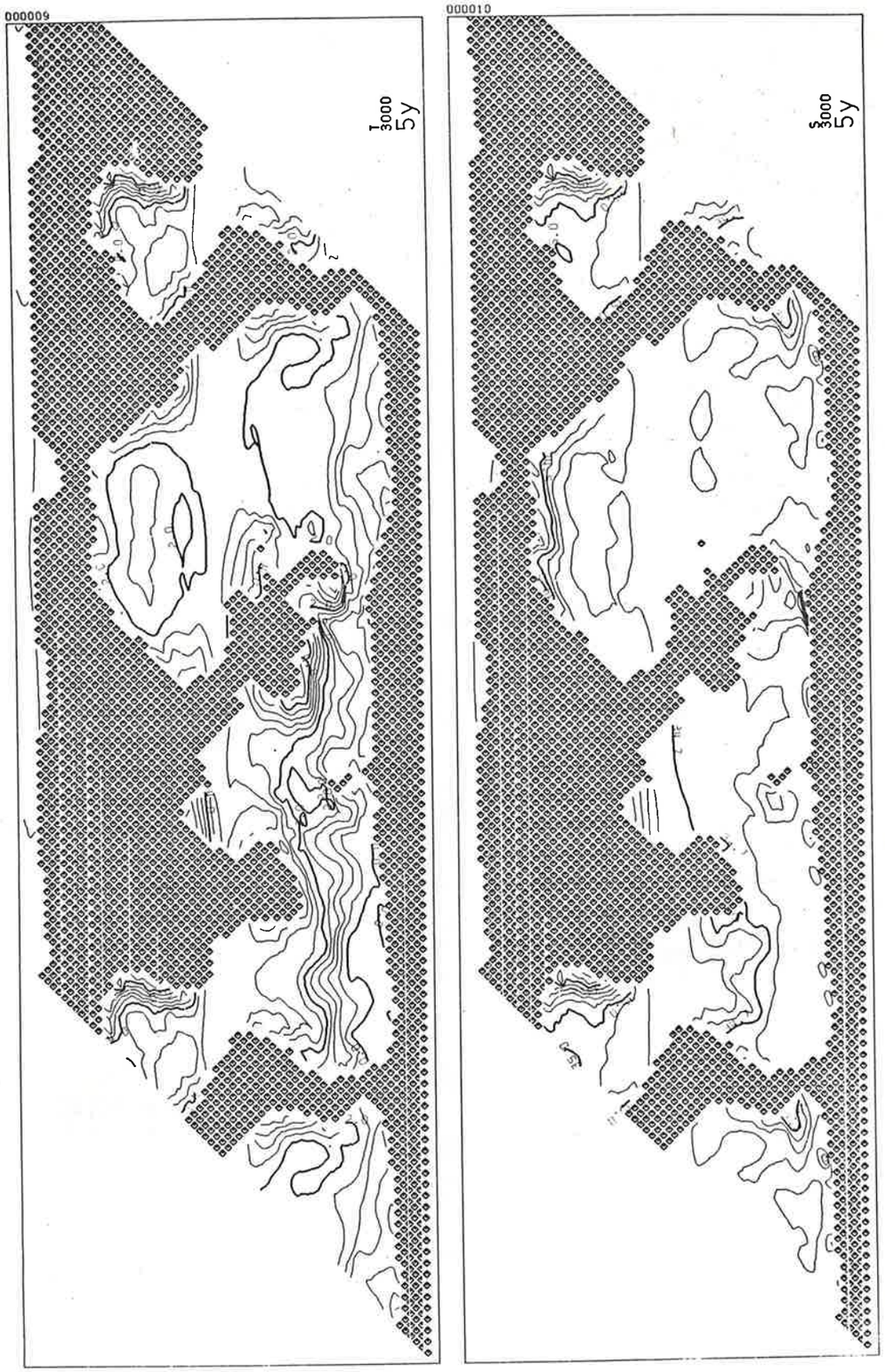

Fig. 5.6b Temperature and salinity at 3000 m-level.
Distribution after 5 years of integration.

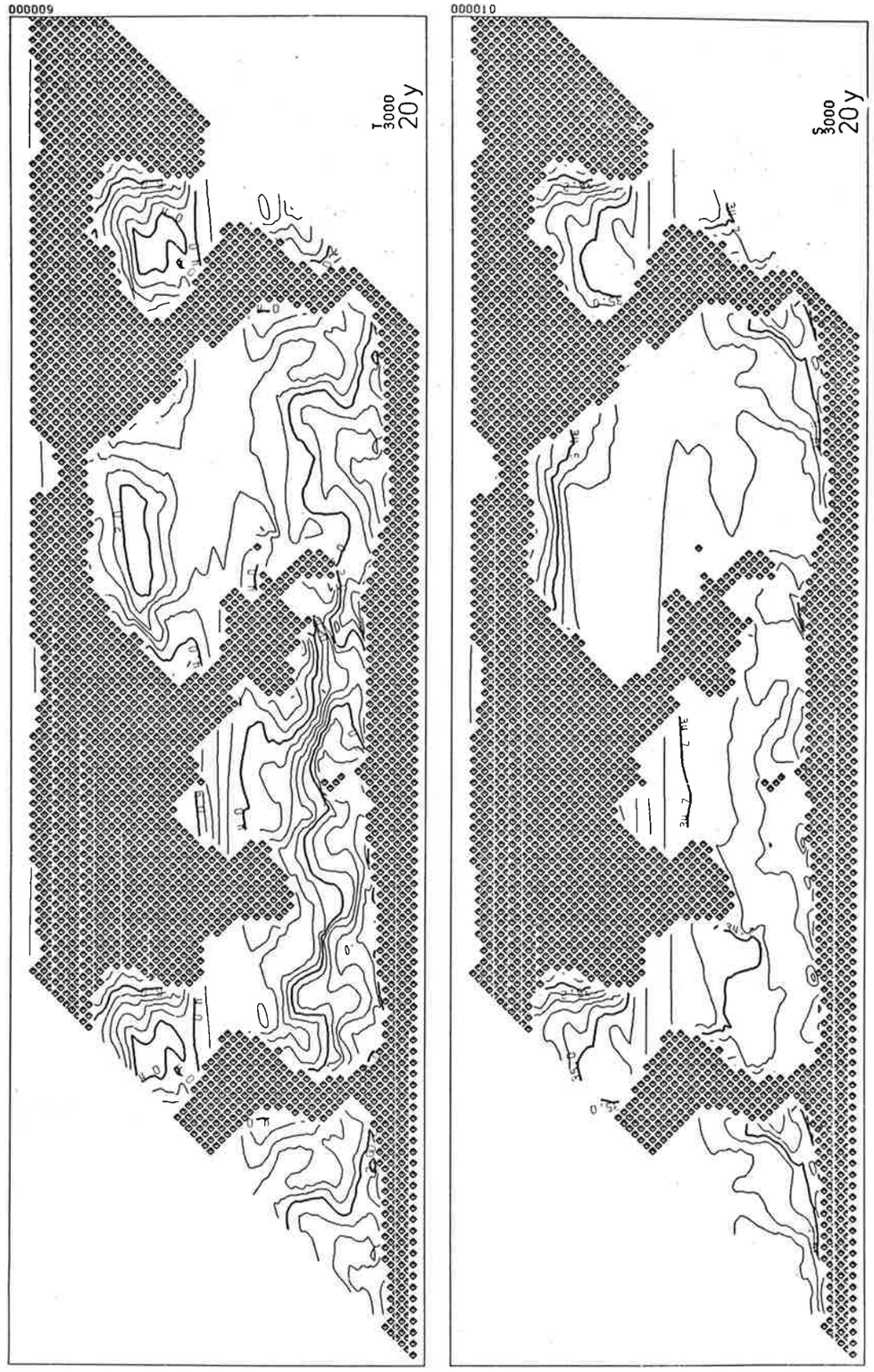

Fig. 5.6c Temperature and salinity at 3000 m-level.
Distribution after 20 years of integration.

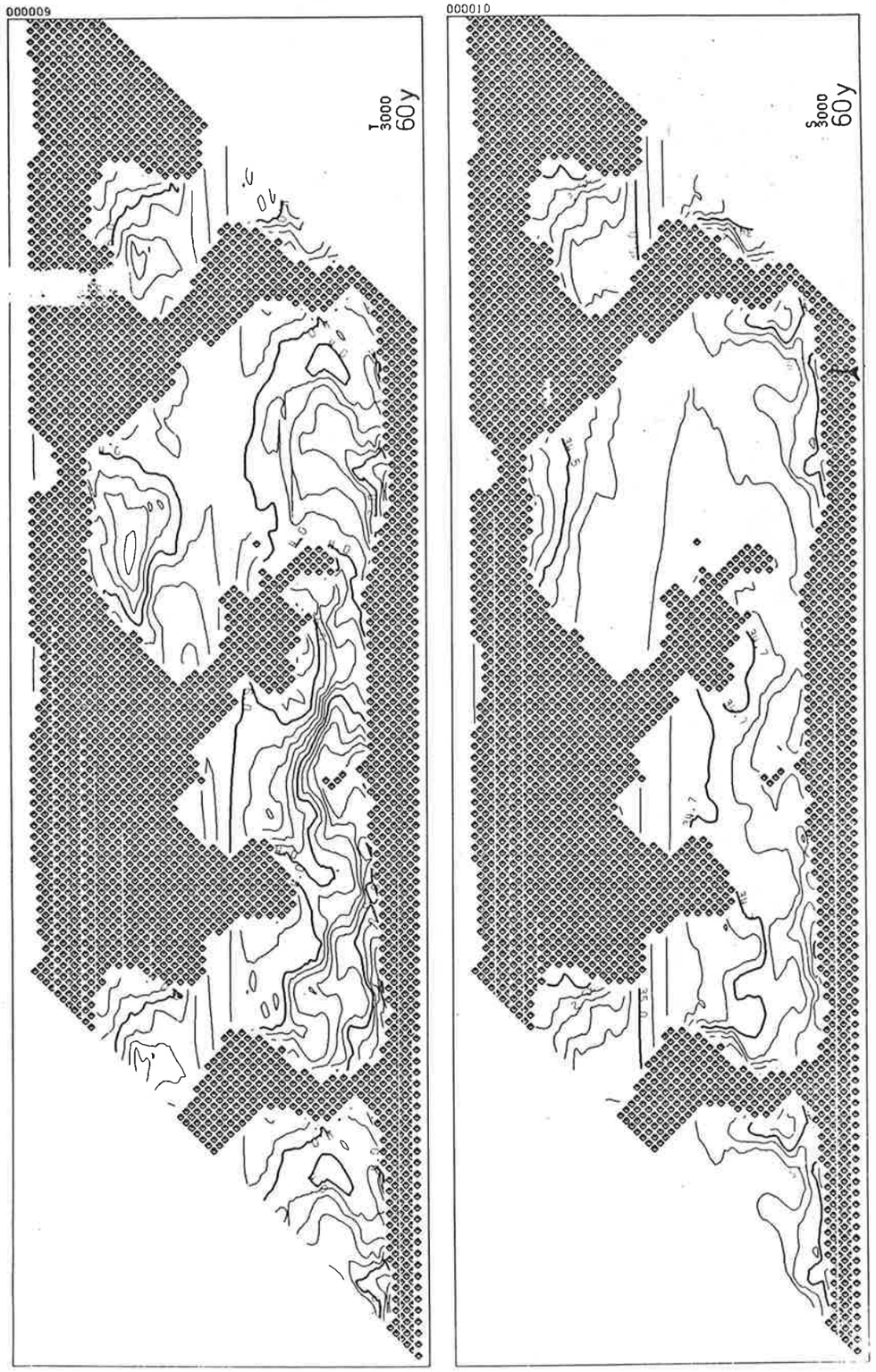

Fig. 5.6d Temperature and salinity at 3000 m-level.
Distribution after 60 years of integration.

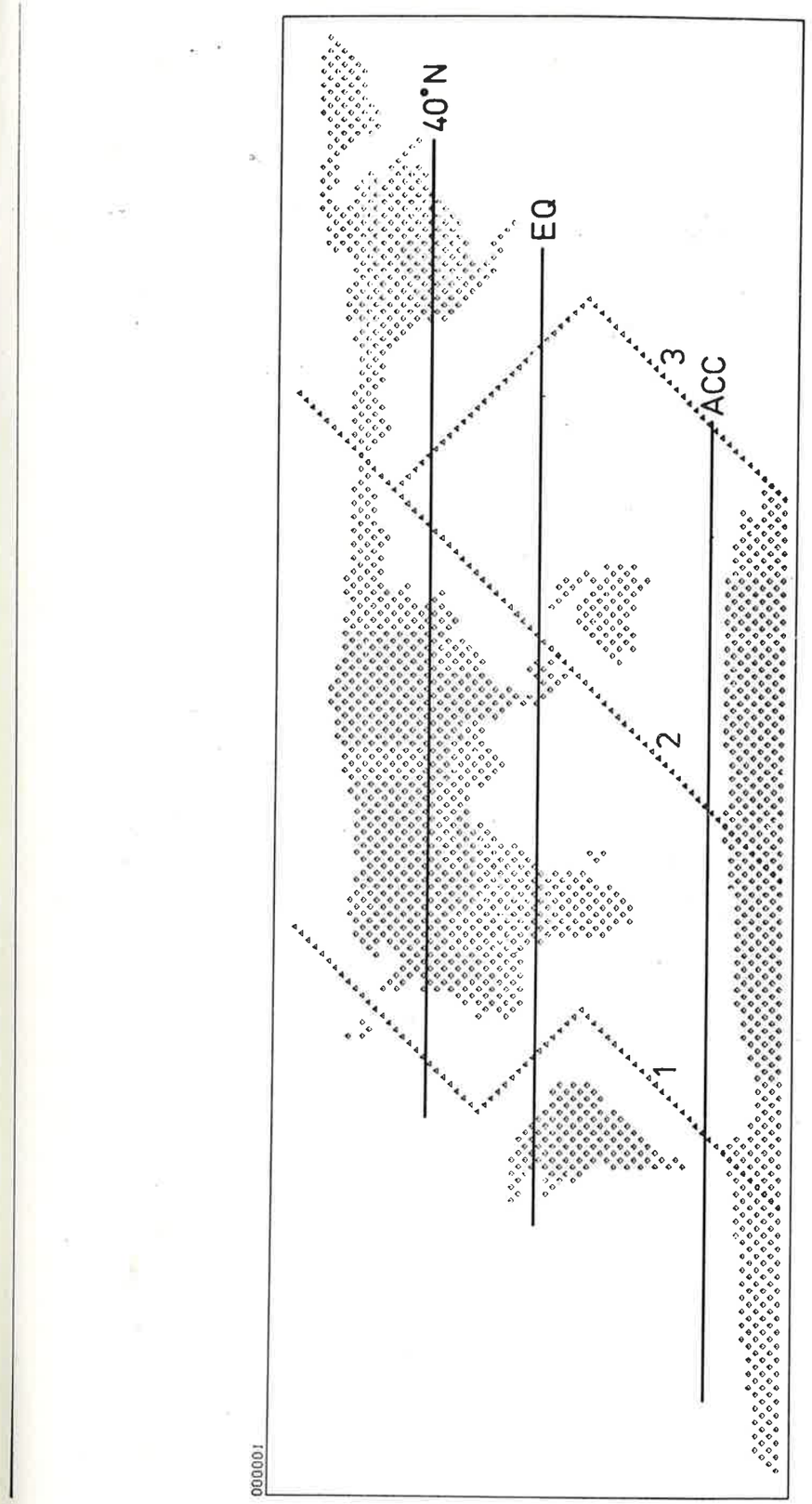

Fig. 5.7 Location of sections 1, 2, 3, 40°N, Eq, and ACC.

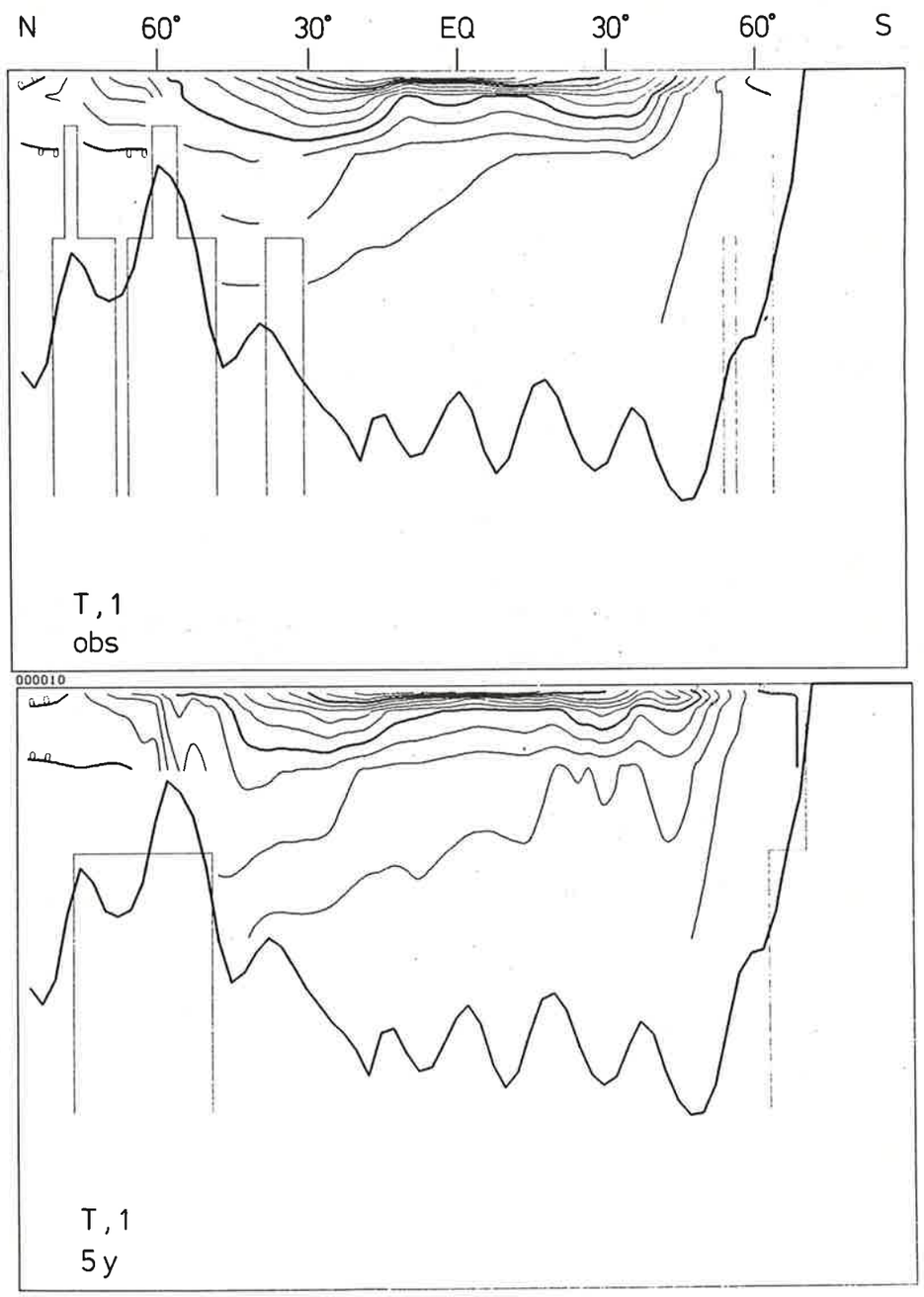

Fig. 5.8a Temperature along section 1. Observed distribution and after 5 years of integration.

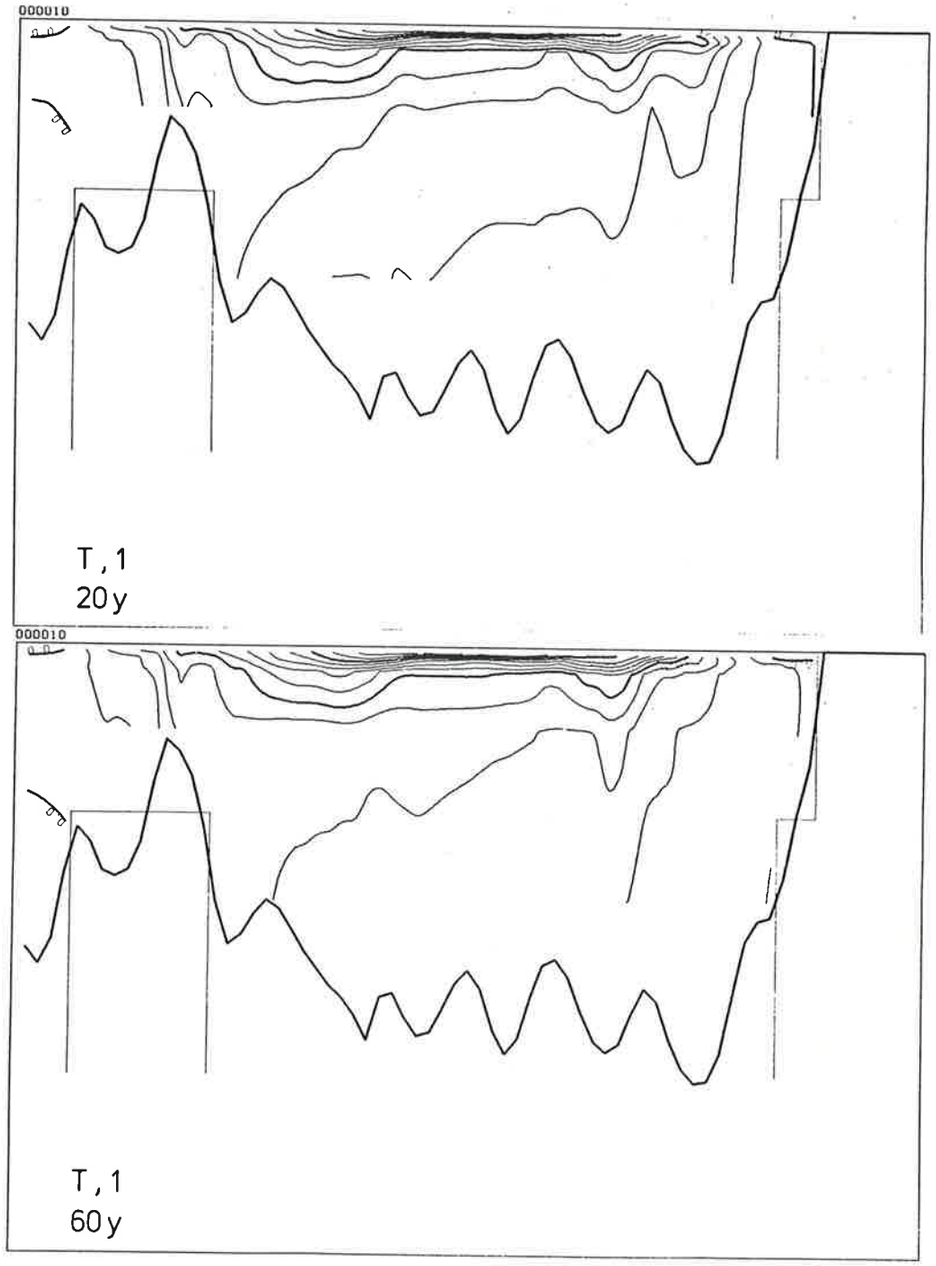

Fig. 5.8b Temperature along section 1. After 20 years and after 60 years of integration.

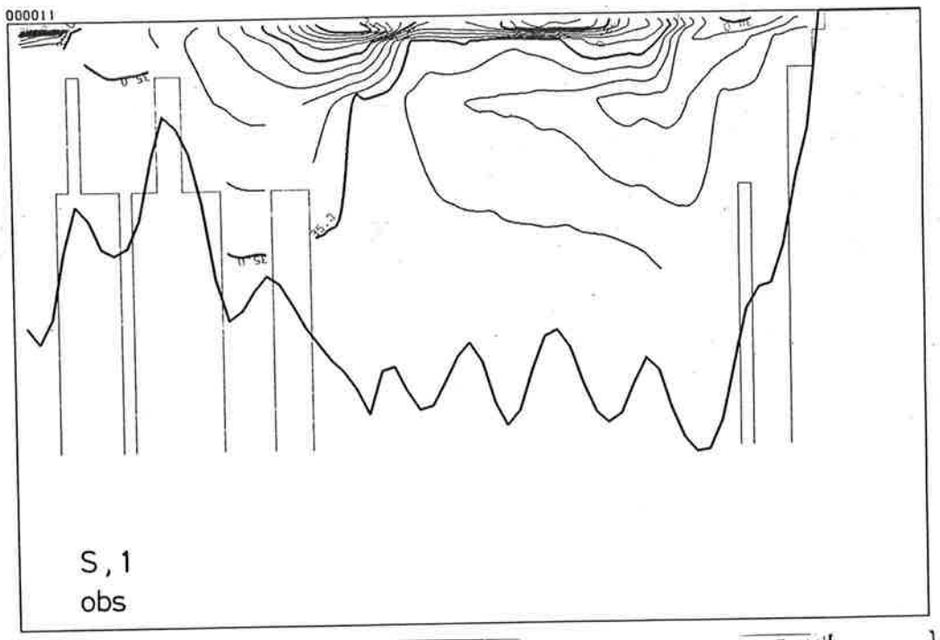

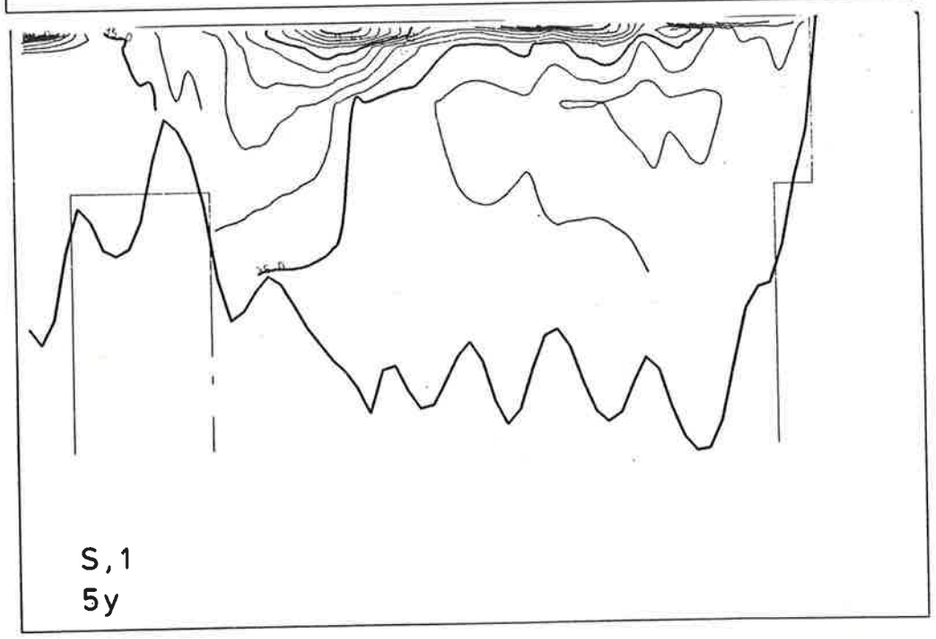

Fig. 5.8c Salinity along section 1. Observed distribution and after 5 years of integration.

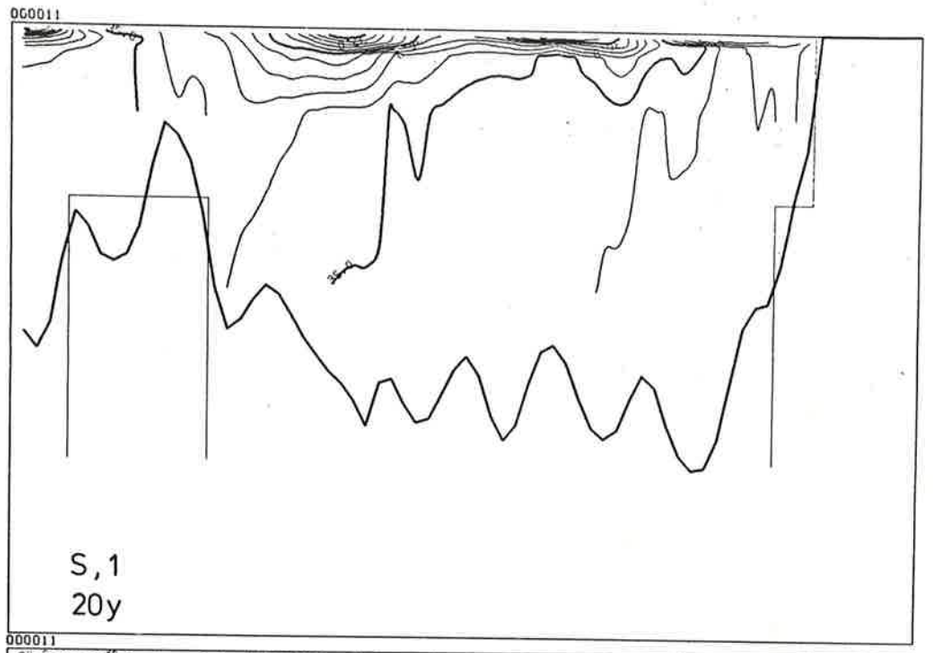

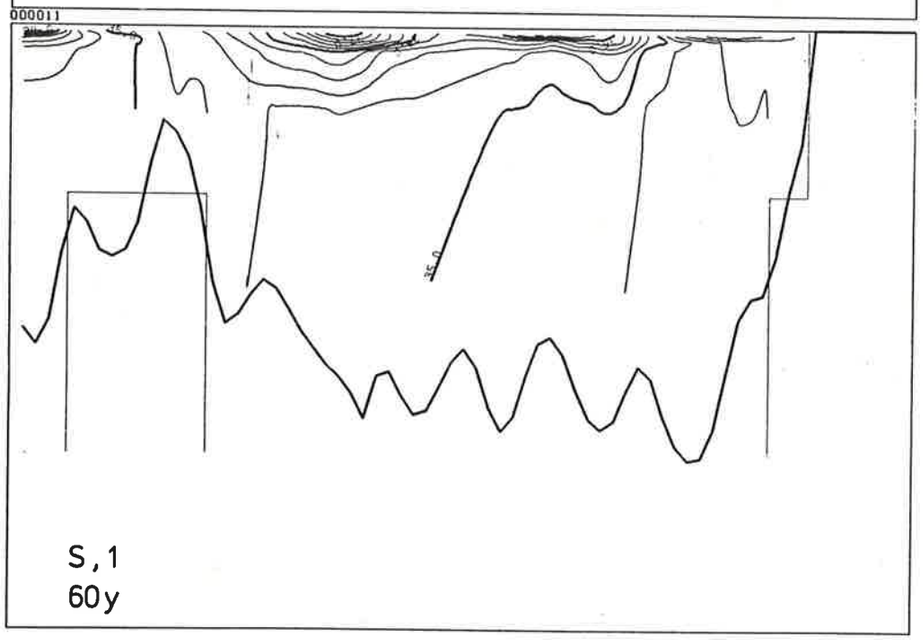

Fig. 5.8d Salinity along section 1. After 20 years and after 60 years of integration.

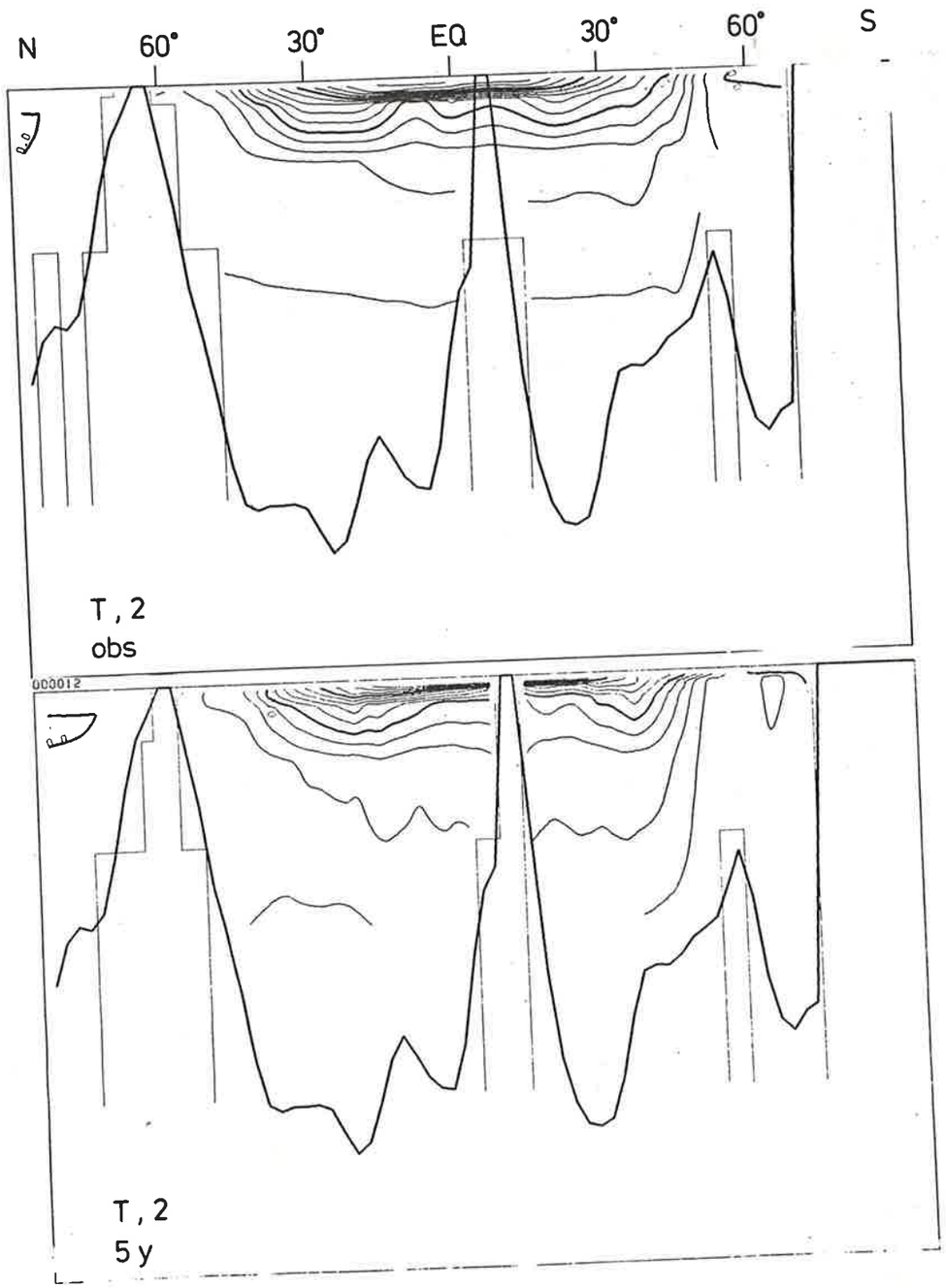

Fig. 5.9a Temperature along section 2. Observed distribution and after 5 years of integration.

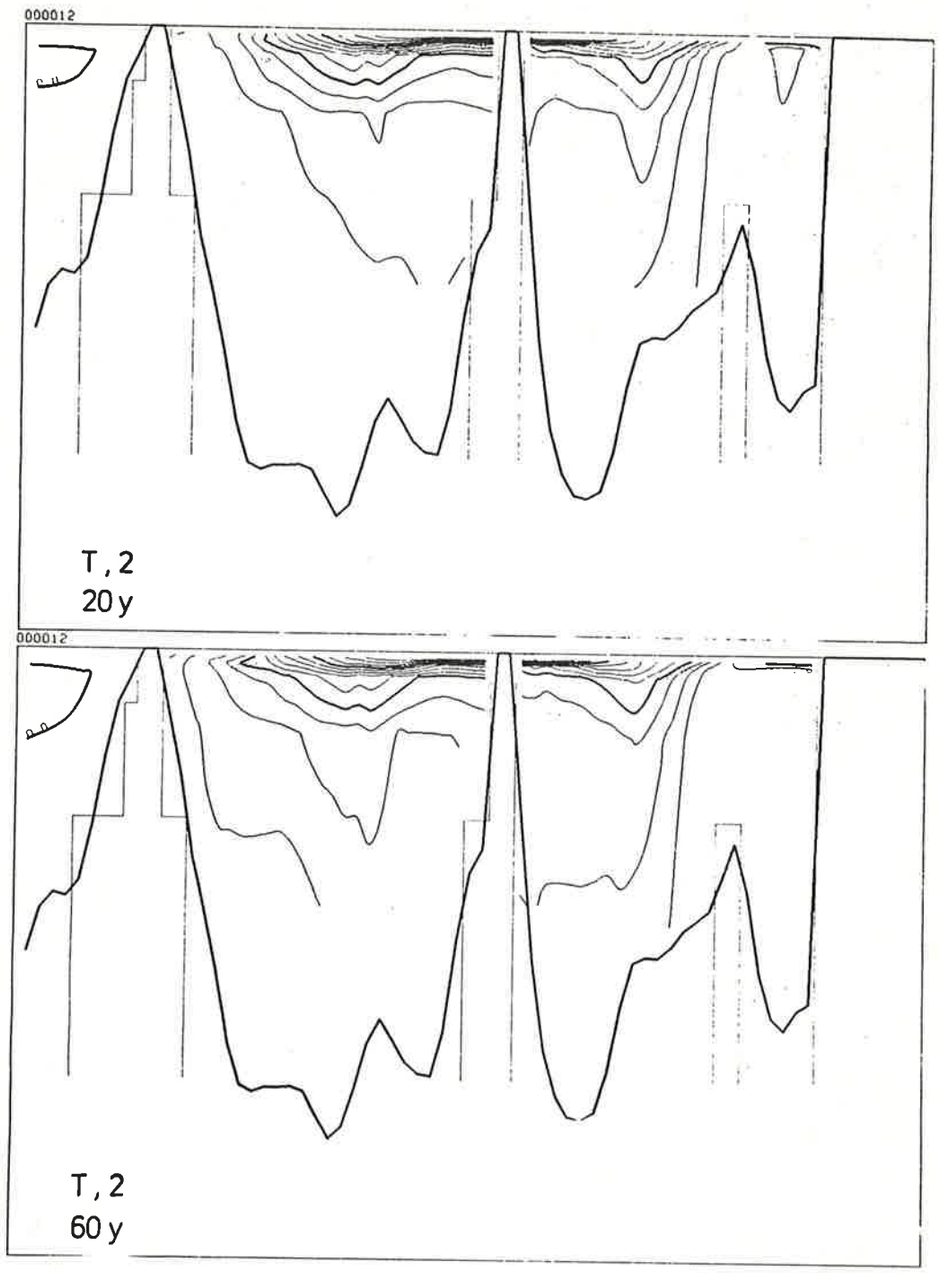

Fig. 5.9b Temperature along section 2. After 20 years and after 60 years of integration.

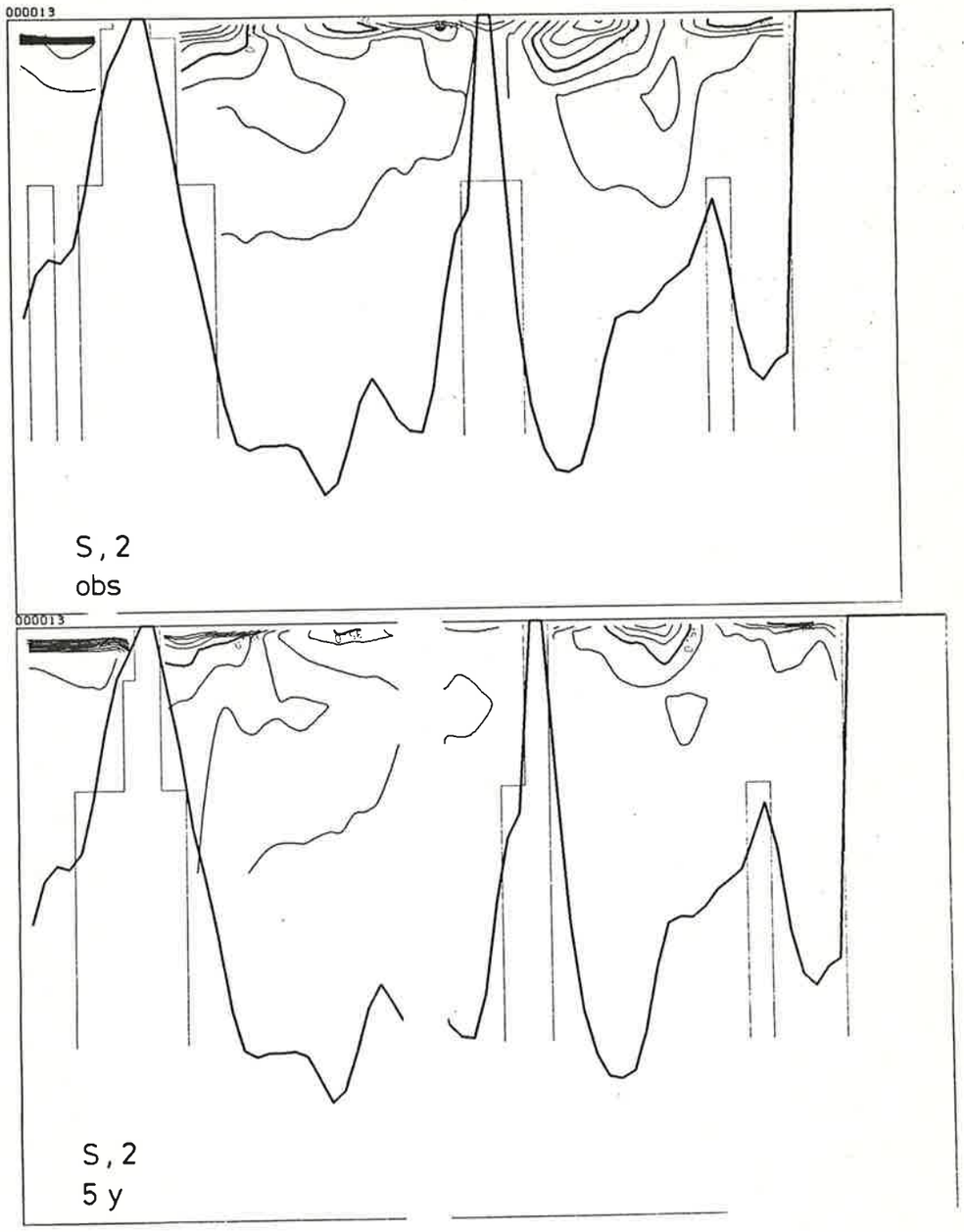

Fig. 5.9c Salinity along section 2. Observed distribution and after 5 years of integration.

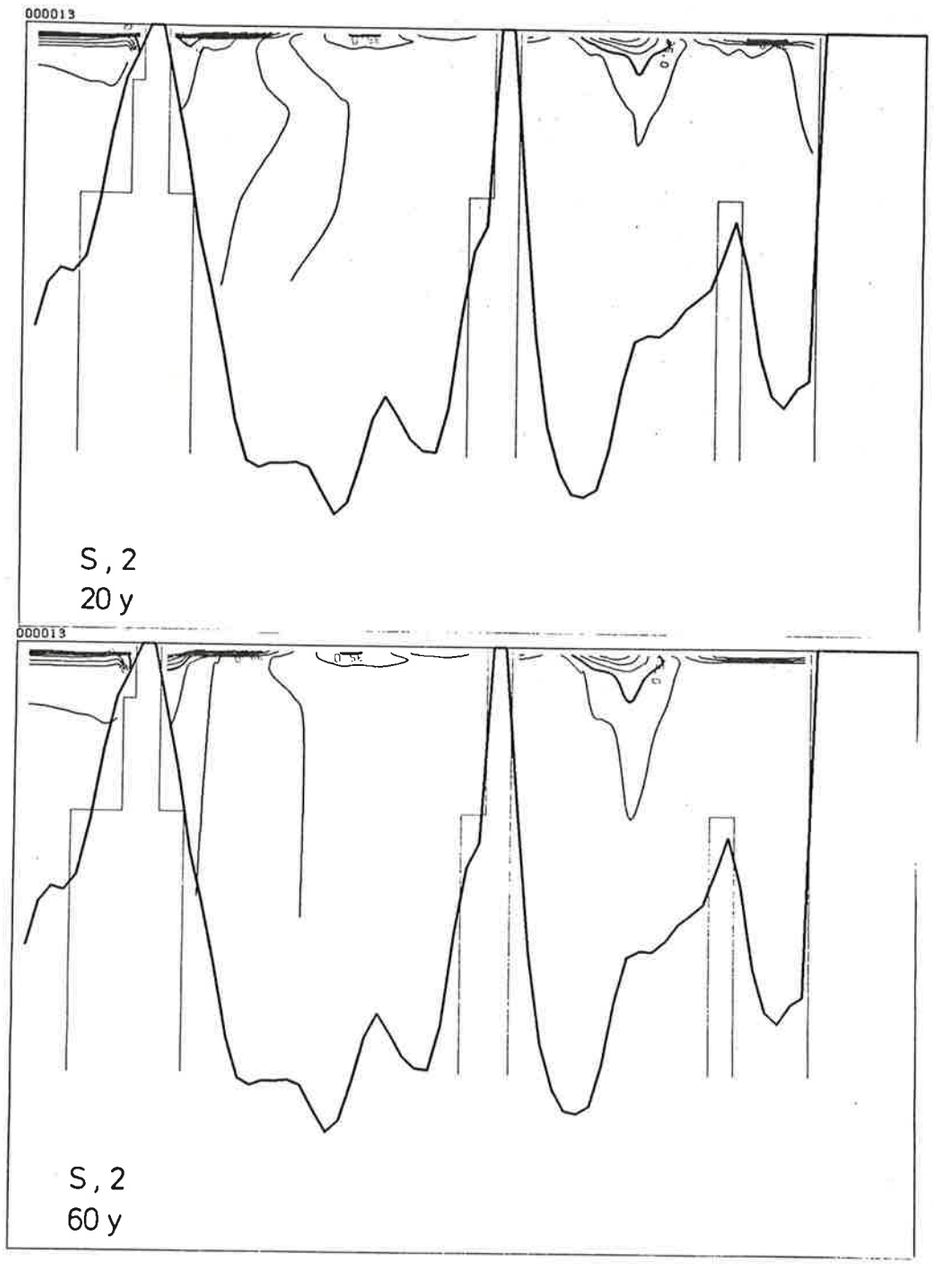

Fig. 5.9d Salinity along section 2. After 20 years and after 60 years of integration.

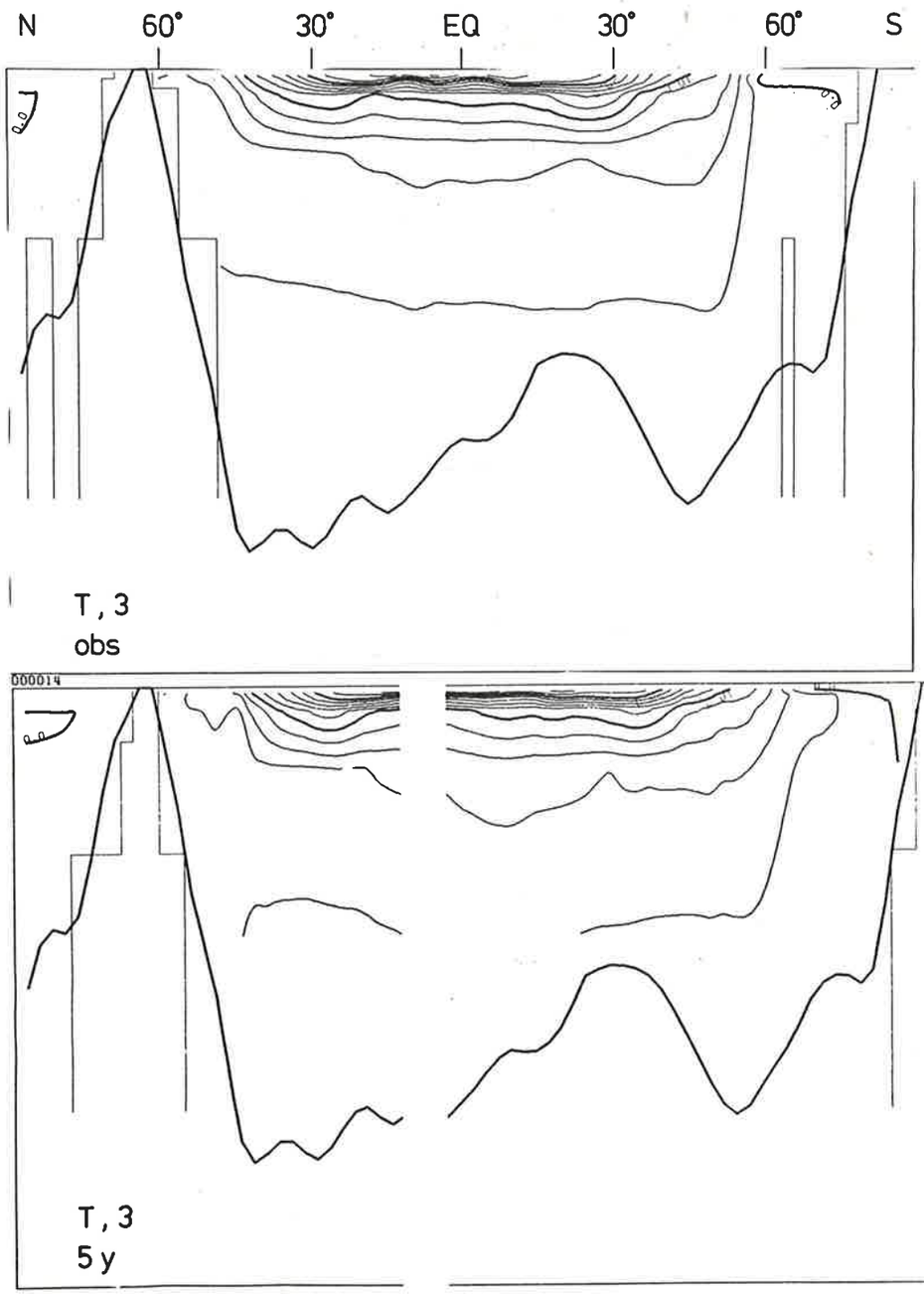

Fig. 5.10a Temperature along section 3. Observed distribution and after 5 years of integration.

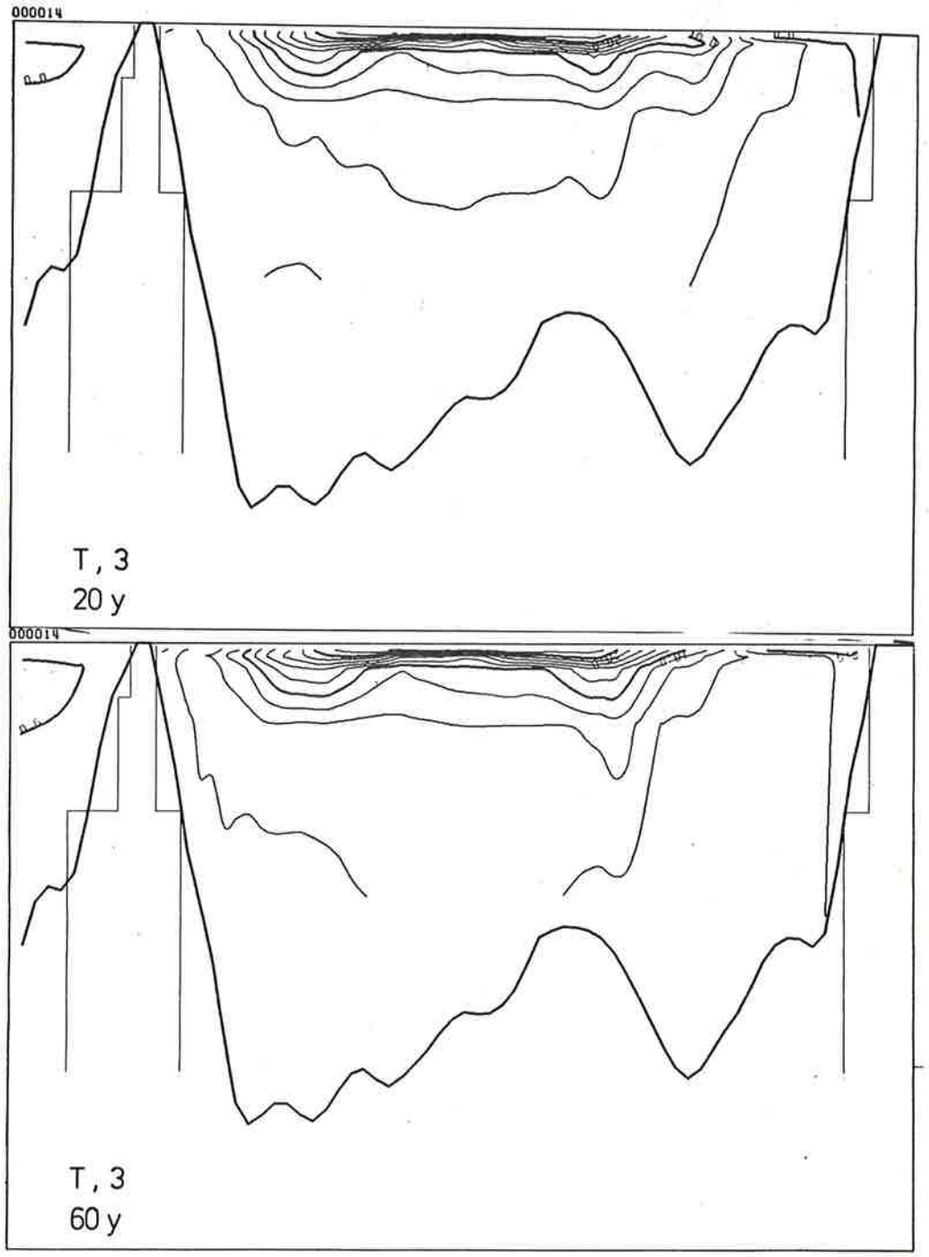

Fig. 5.10b Temperature along section 3. After 20 years and after 60 years of integration.

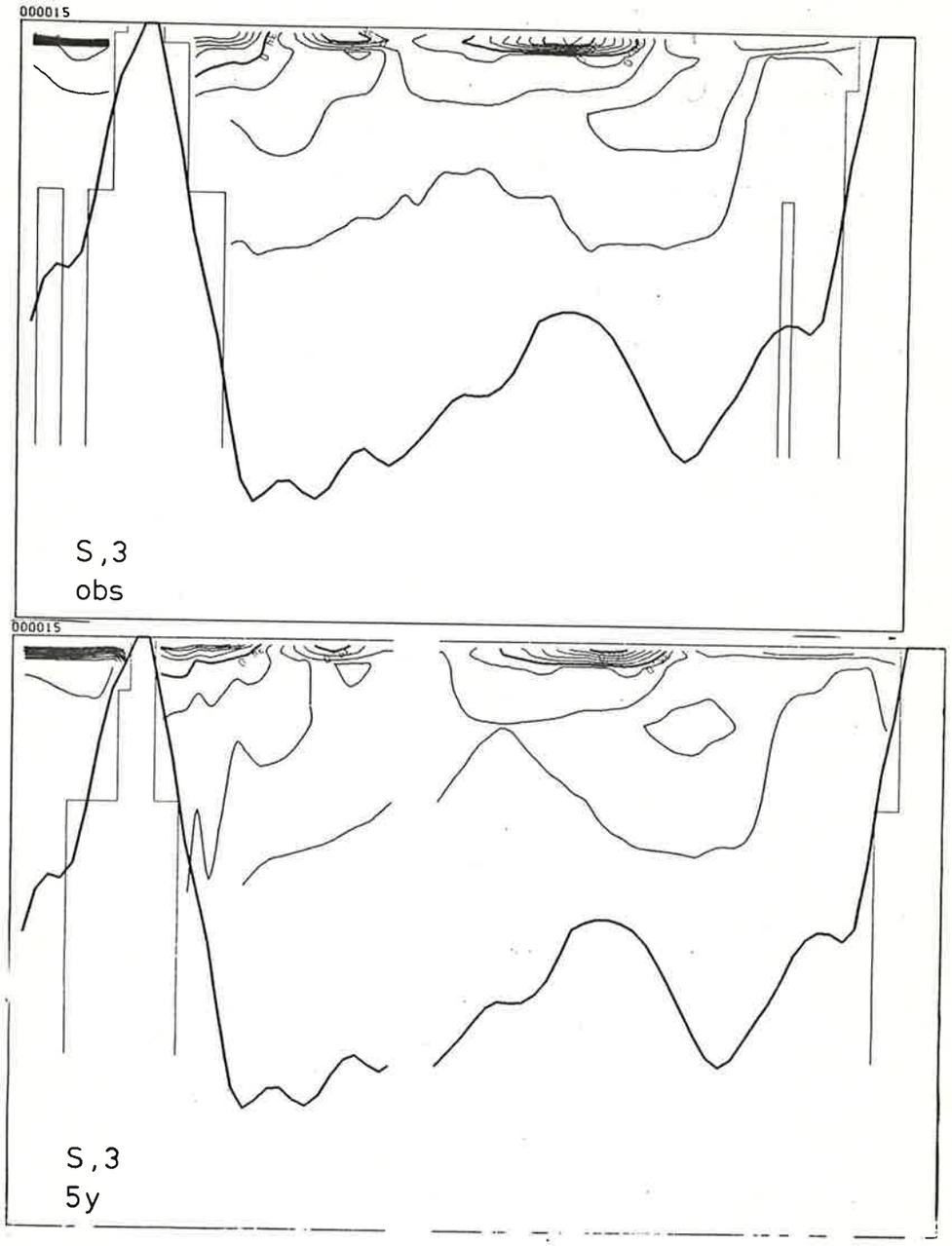

Fig. 5.10c Salinity along section 3. Observed distribution and after 5 years of integration.

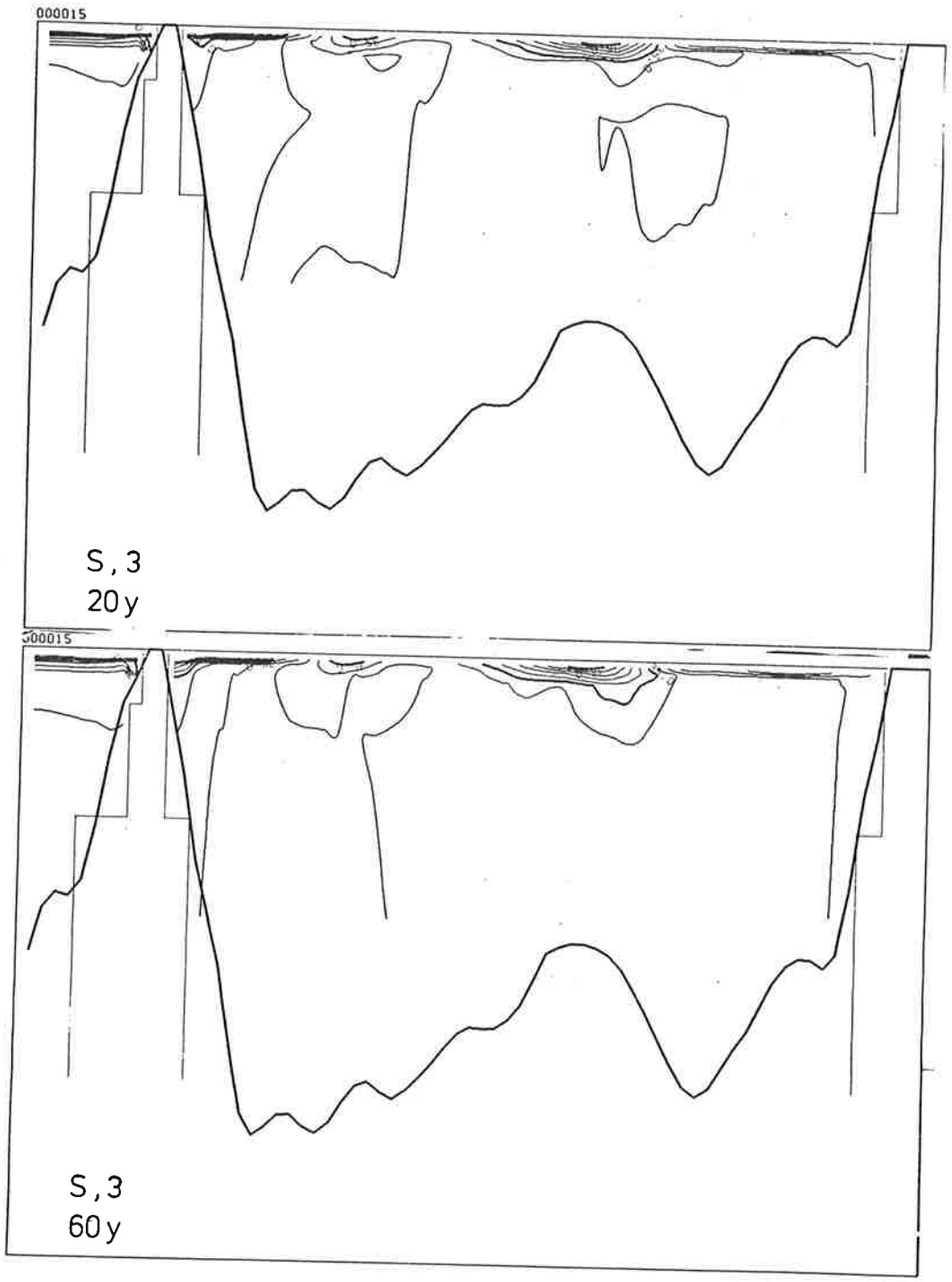

Fig. 5.10d Salinity along section 3. After 20 years and after 60 years of integration.

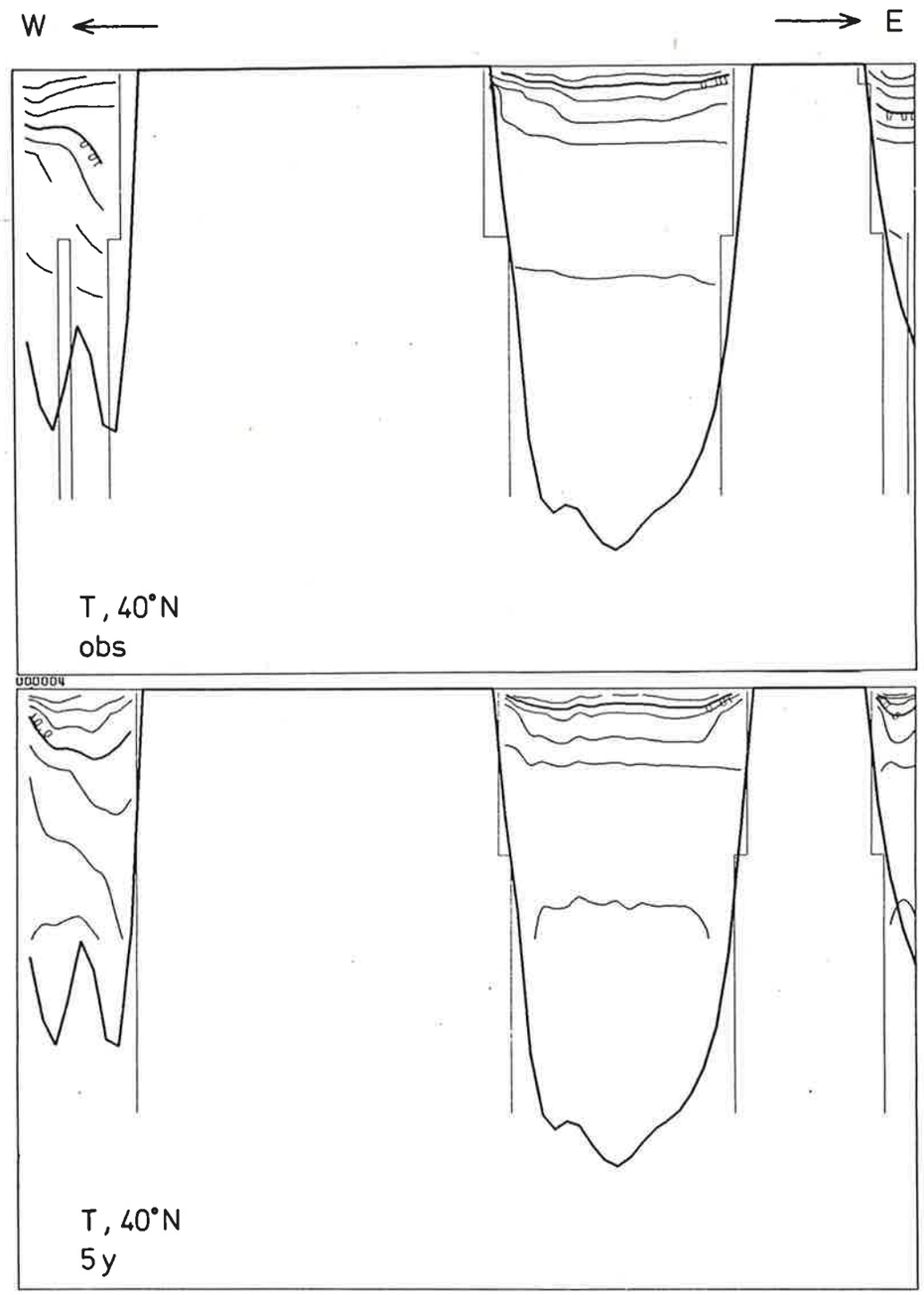

Fig. 5.11a Temperature along section 40°N. Observed distributio and after 5 years of integration.

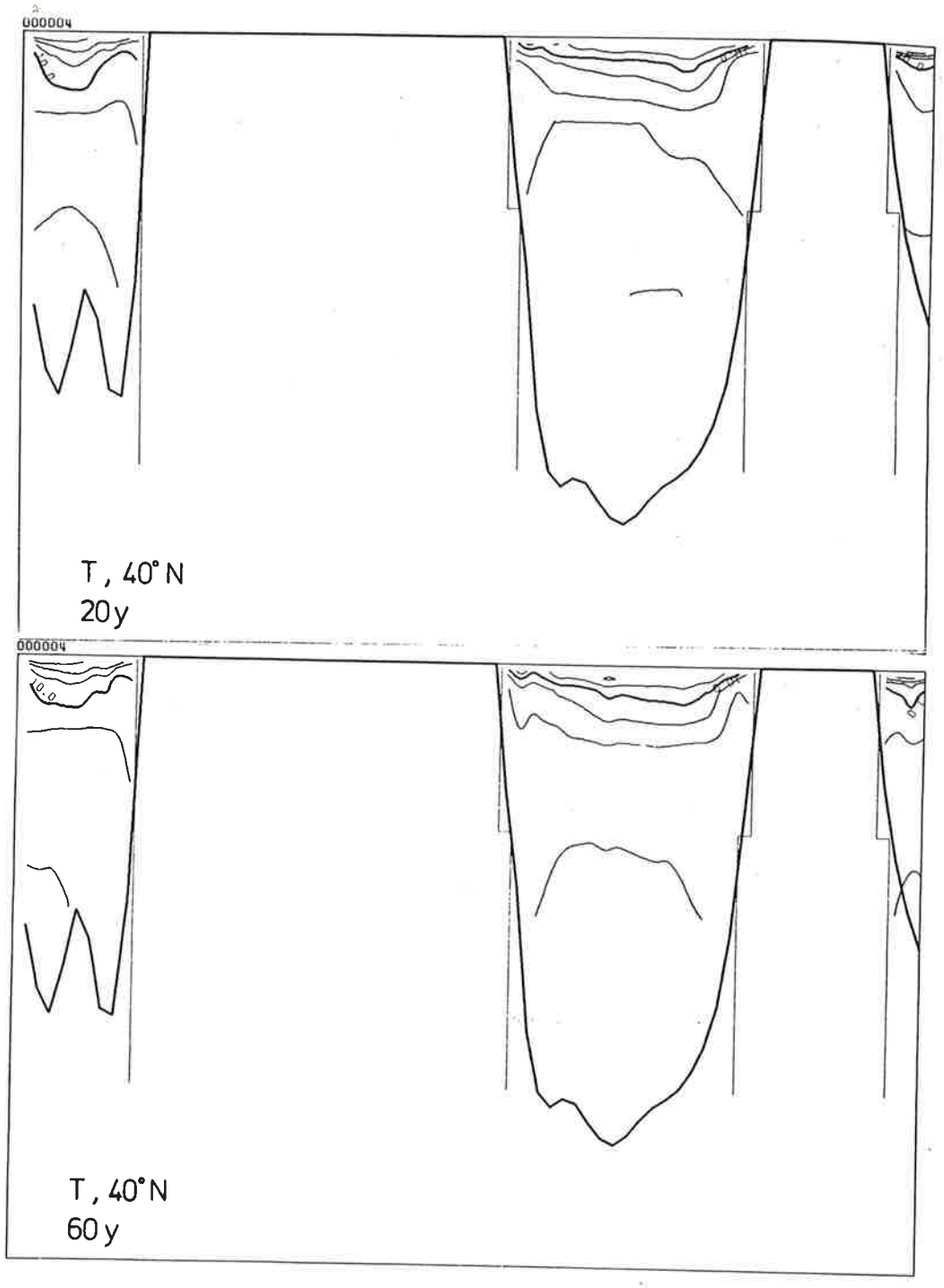

Fig. 5.11b Temperature along section 40°N. After 20 years and after 60 years of integration.

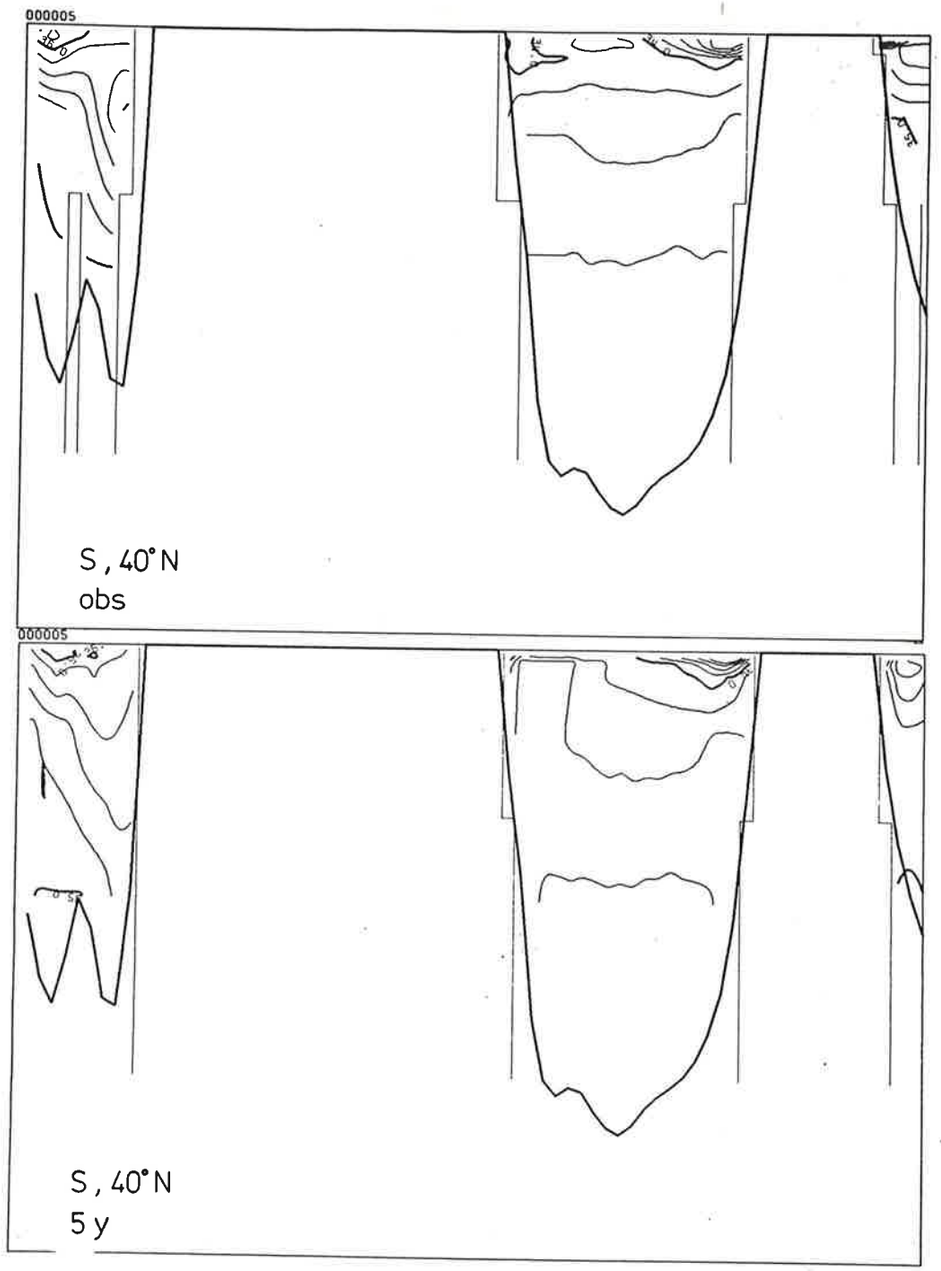

Fig. 5.11c Salinity along section 40°N. Observed distribution and after 5 years of integration.

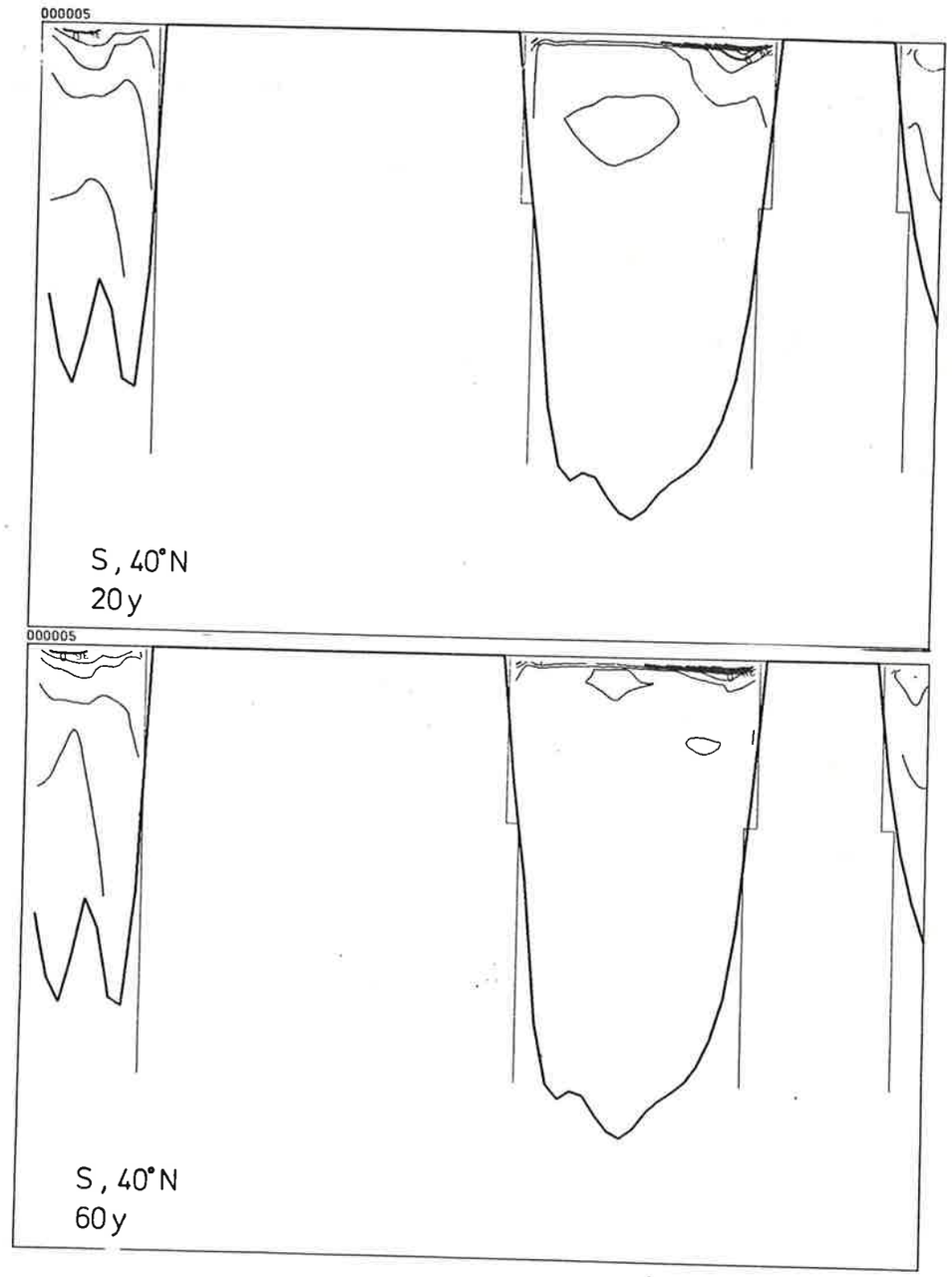

Fig. 5.11d Salinity along section 40°N. After 20 years and after 60 years of integration.

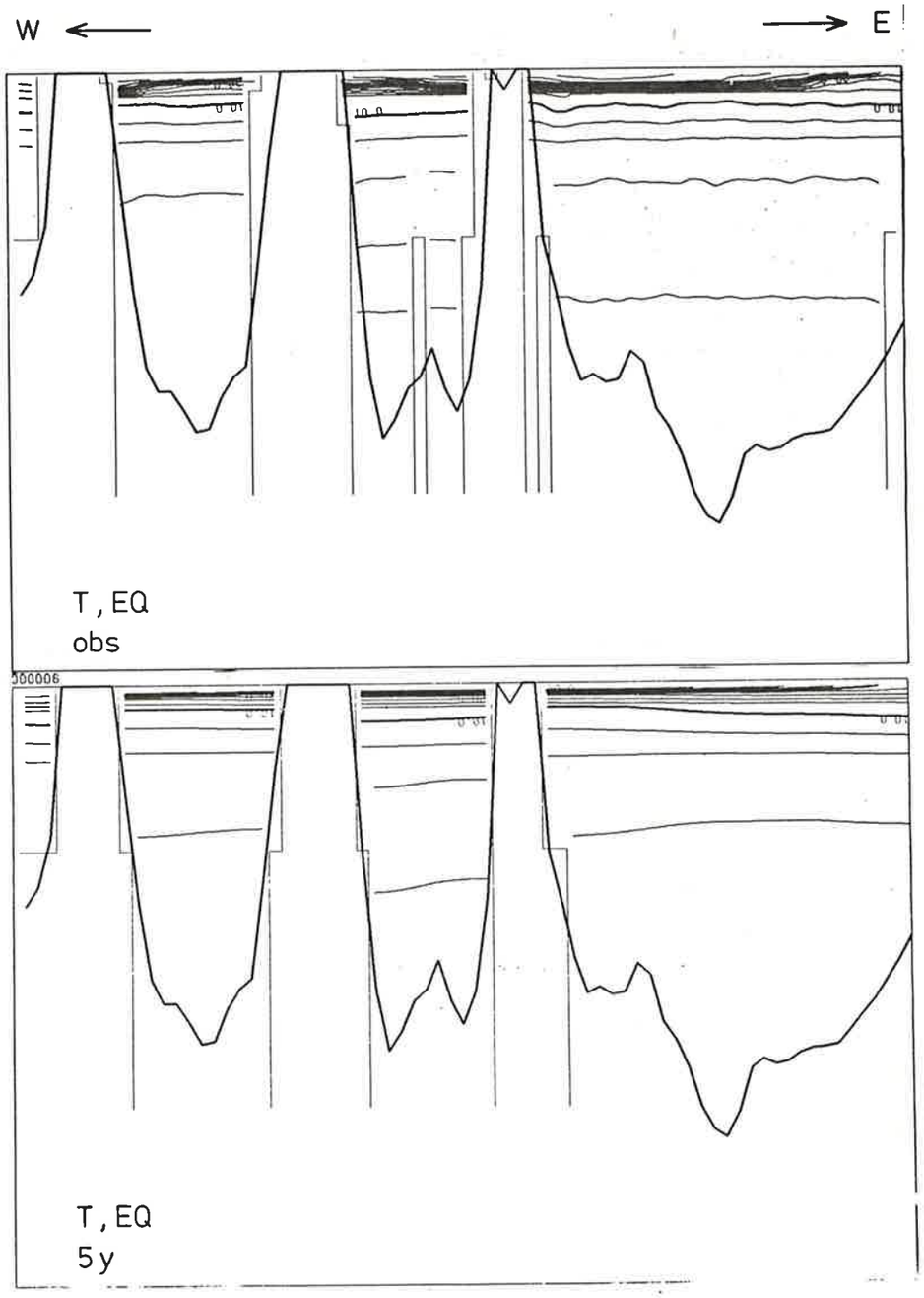

Fig. 5.12a Temperature along section Eq. Observed distribution and after 5 years of integration.

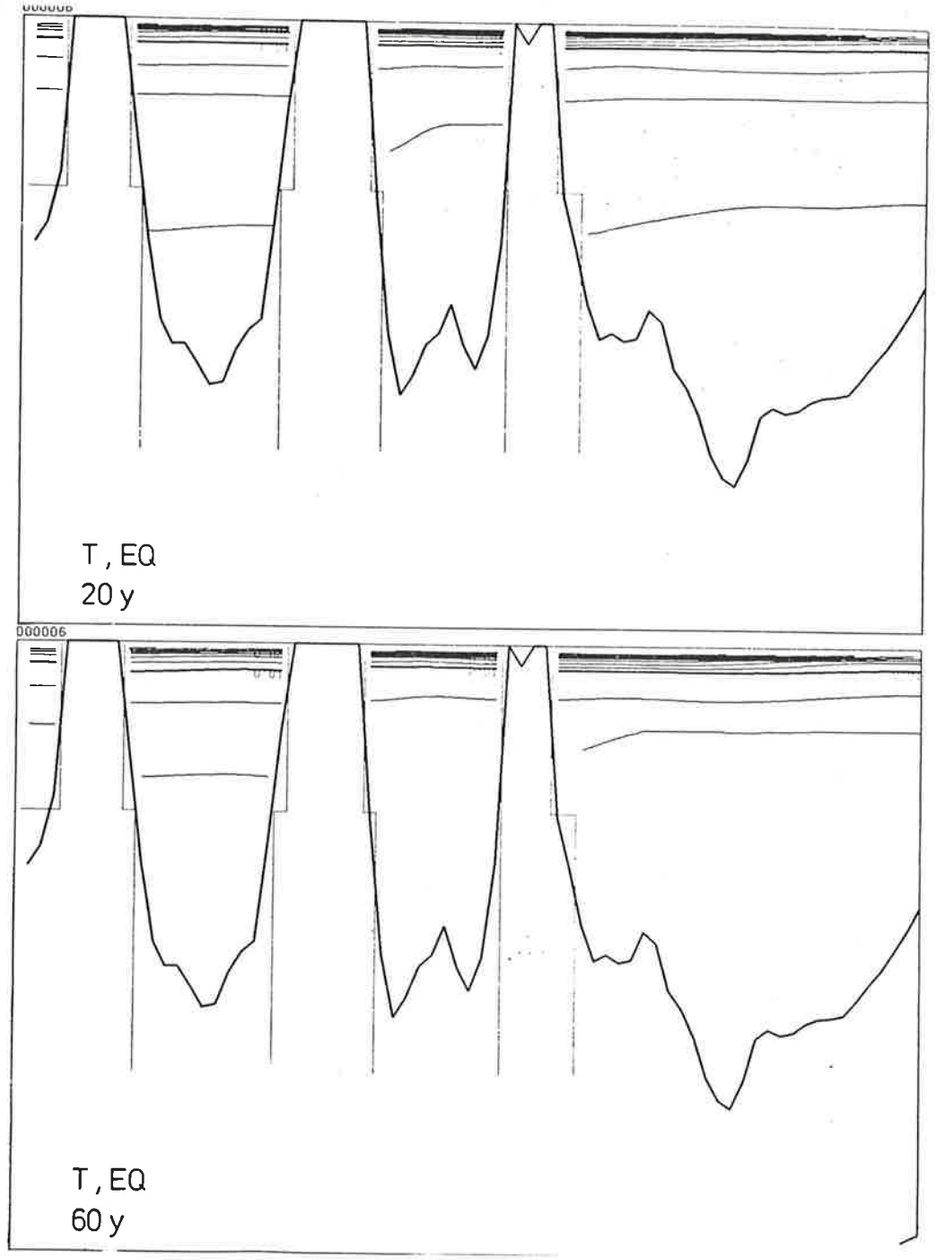

Fig. 5.12b Temperature along section Eq. After 20 years and after 60 years of integration.

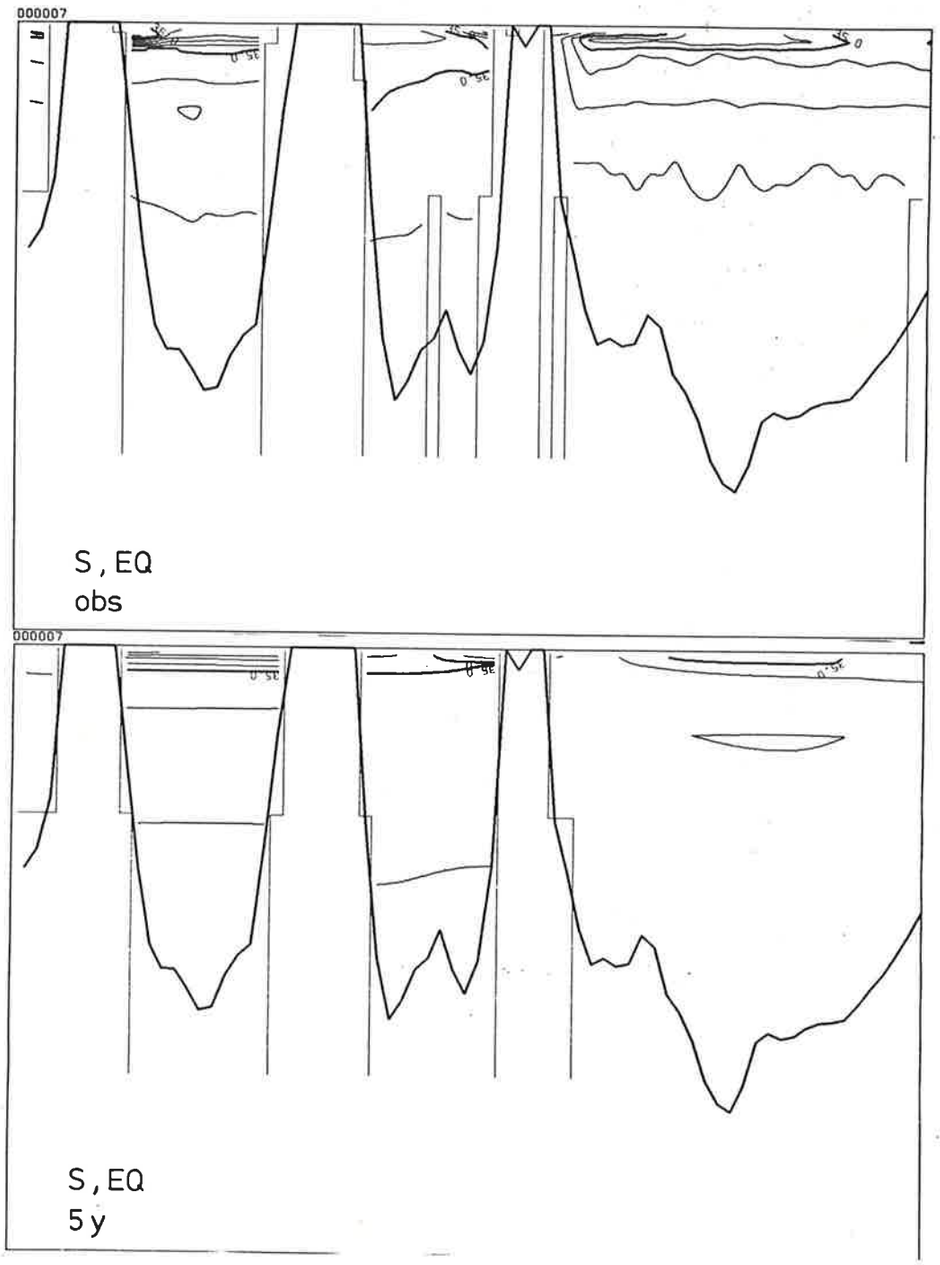

Fig. 5.12c Salinity along section Eq. Observed distribution and after 5 years of integration.

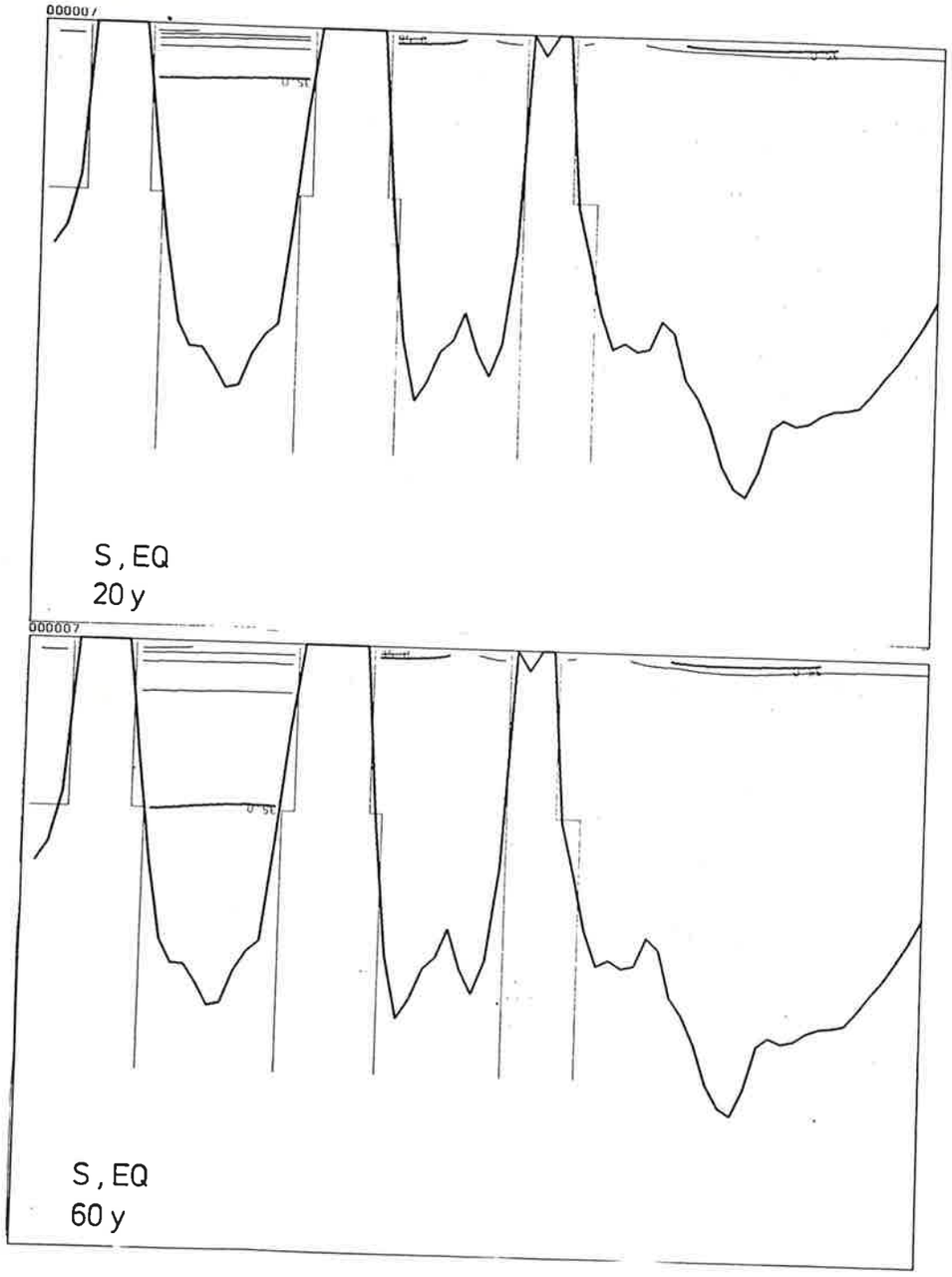

Fig. 5.12d Salinity along section Eq. After 20 years and after 60 years of integration.

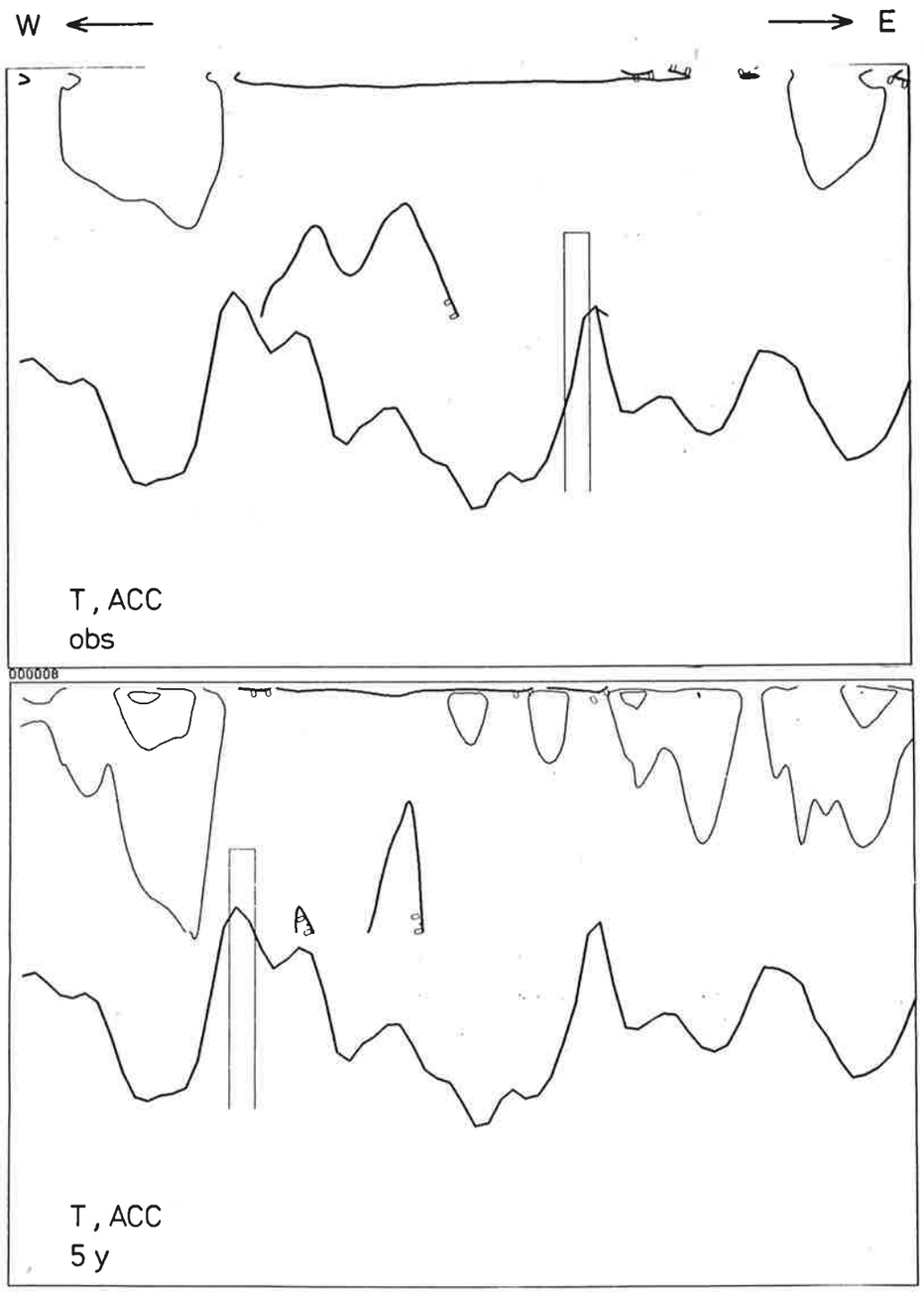

Fig. 5.13a Temperature along section ACC. Observed distribution and after 5 years of integration.

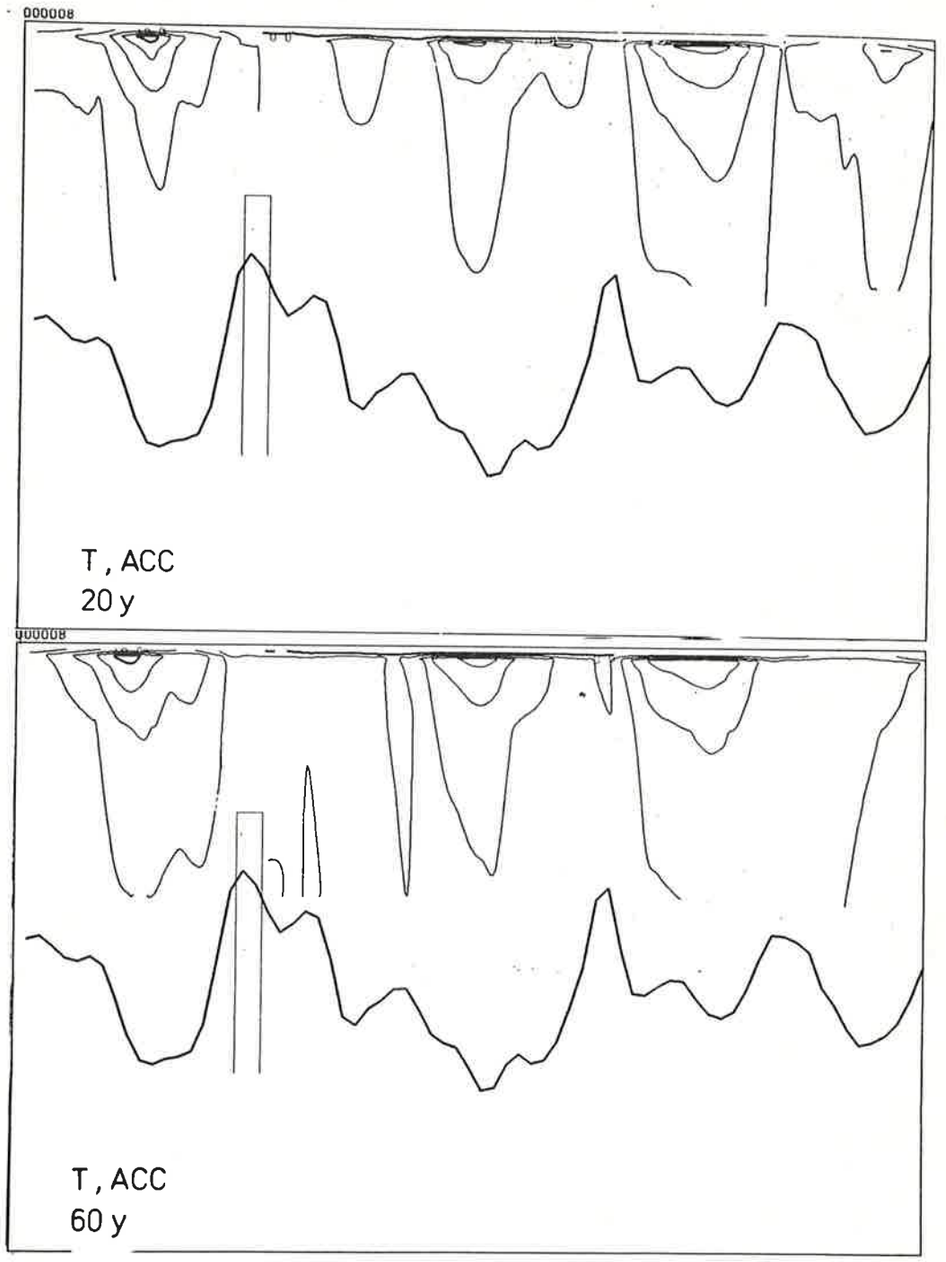

Fig. 5.13b Temperature along section ACC. After 20 years and after 60 years of integration.

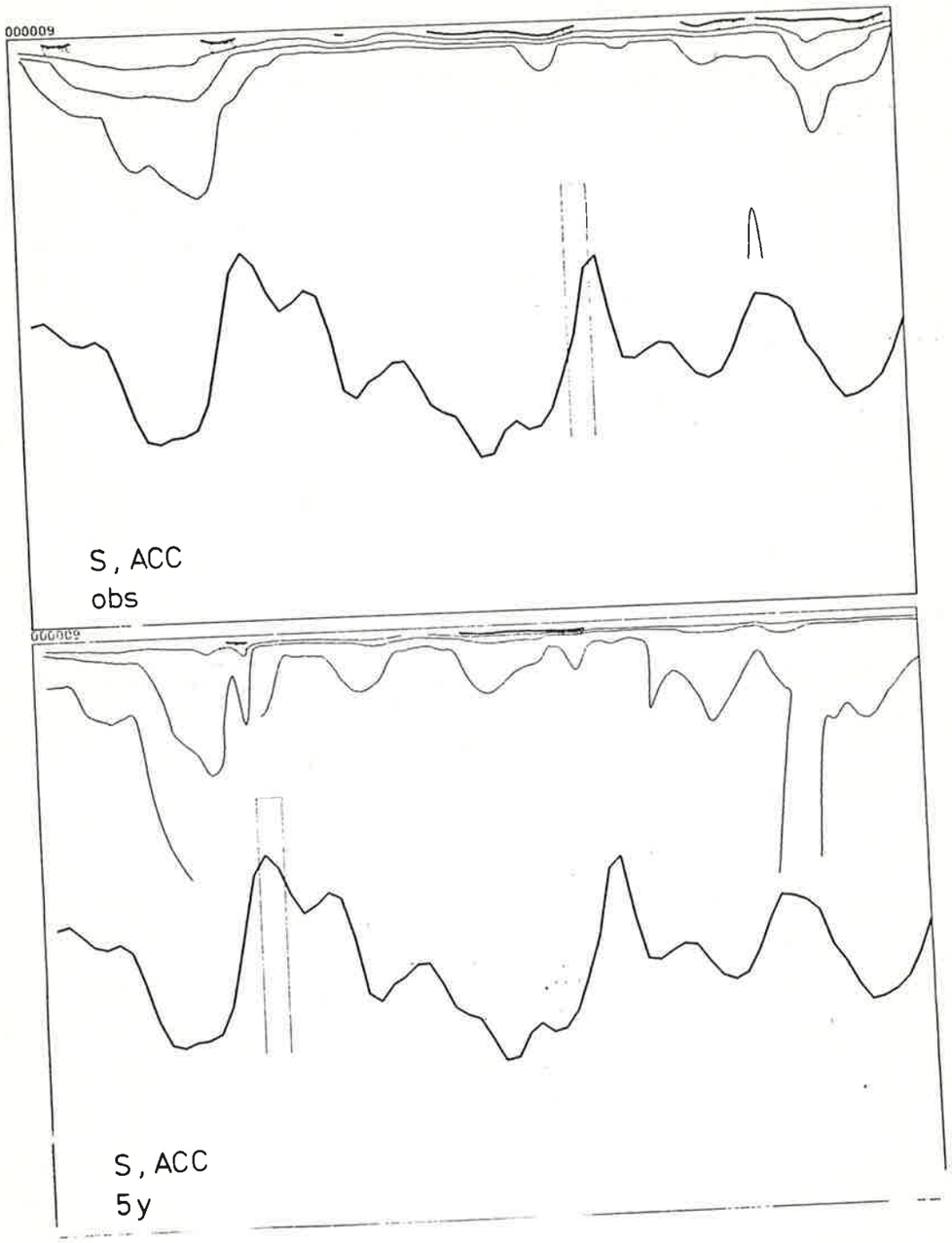

Fig. 5.13c Salinity along section ACC. Observed distribution and after 5 years of integration.

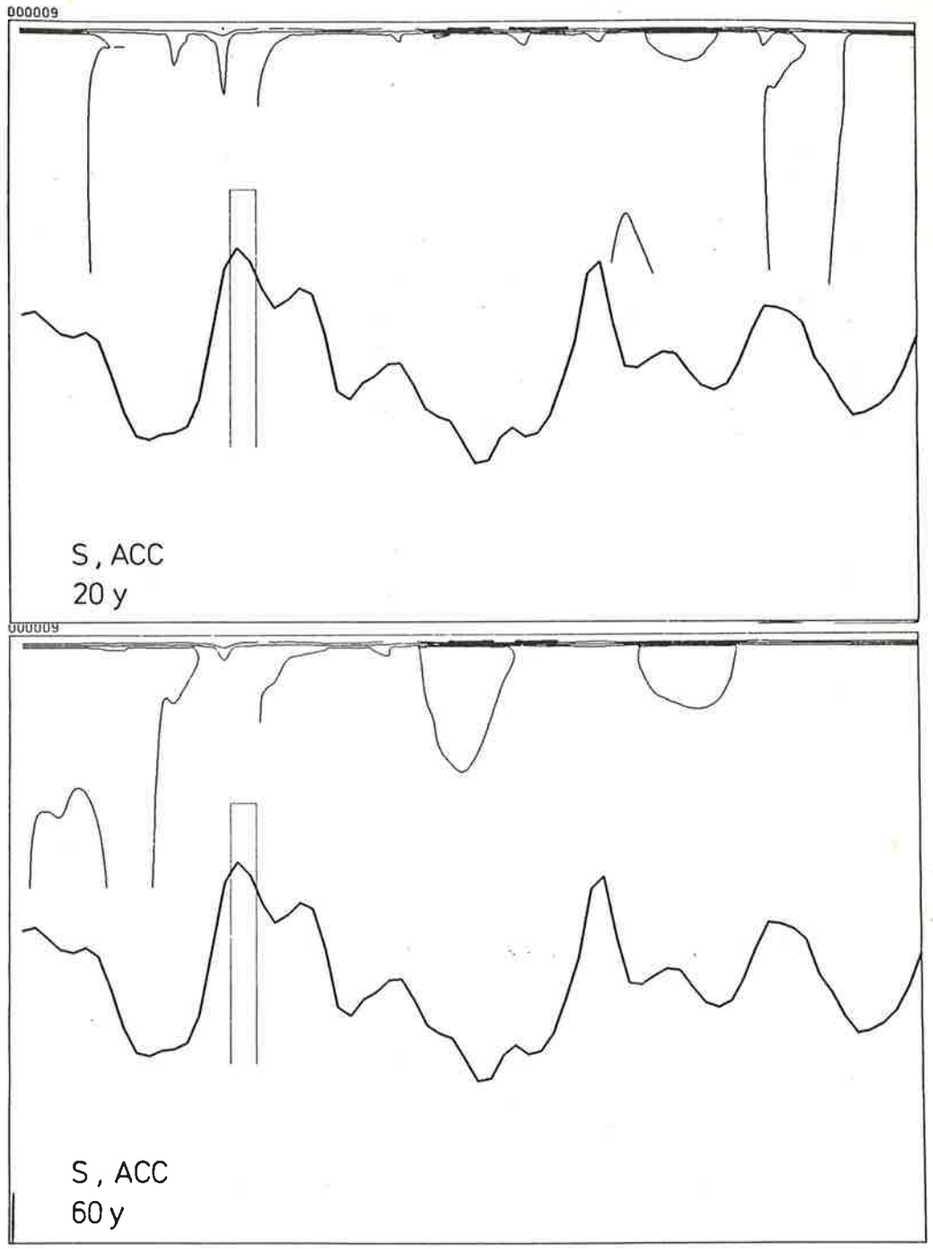

Fig. 5.13d Salinity along section 3. After 20 years and after 60 years of integration.

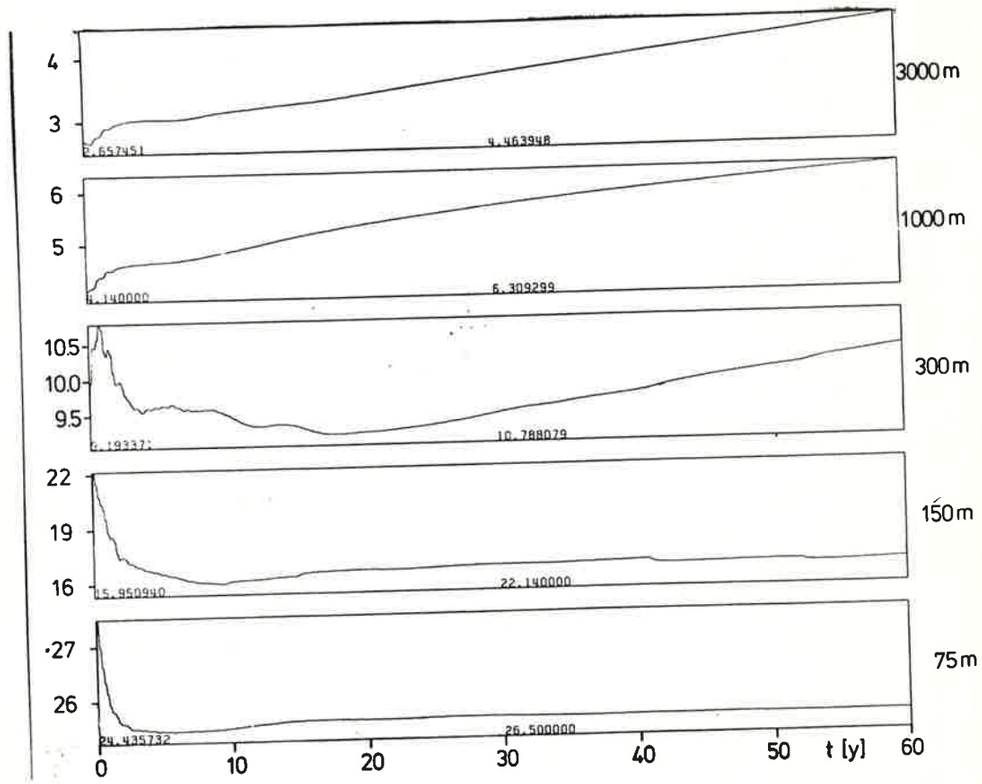

Fig. 5.14 Time series of temperature at 1° N on the section 1 for different levels.

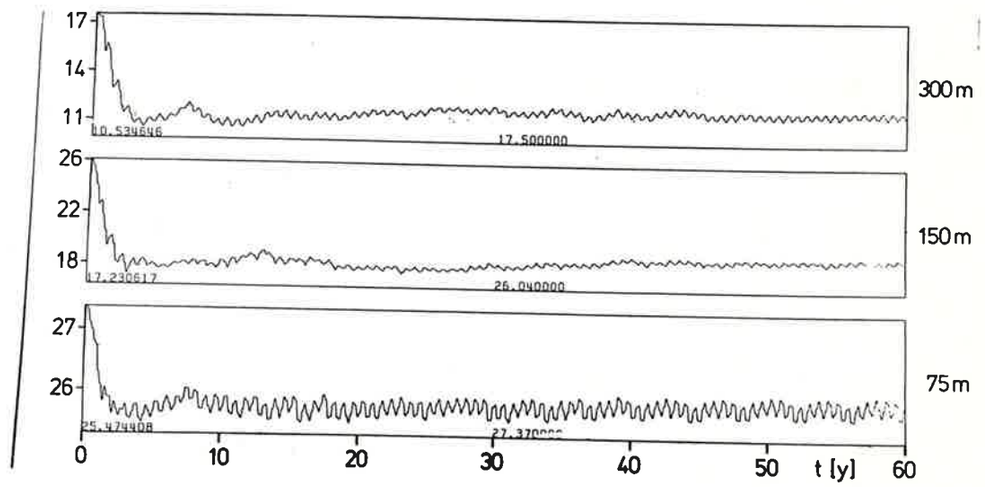

Fig. 5.15 Time series of temperature at 20° N on the section 1 for different levels.

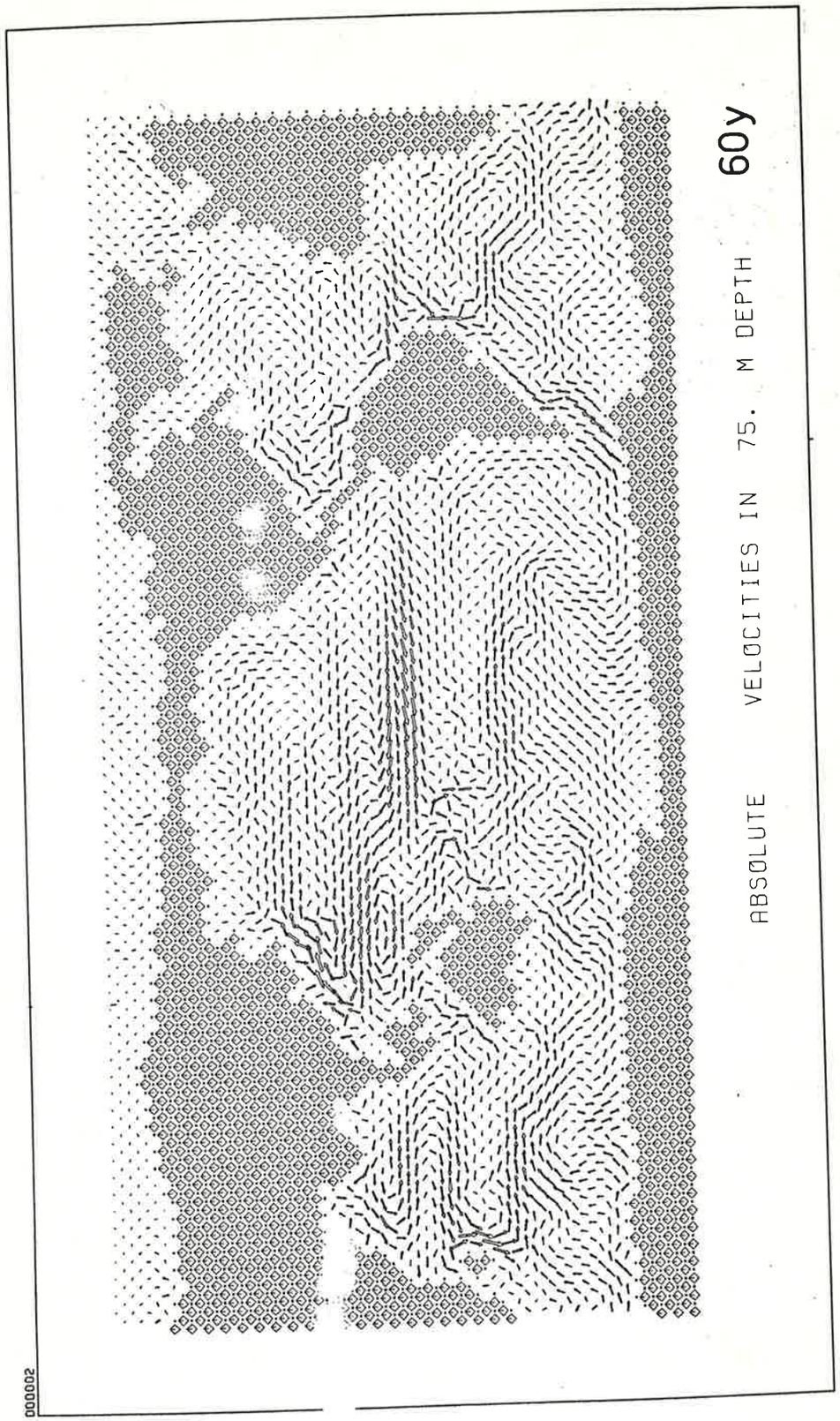

Fig. 5.16a Horizontal velocity at 75 m-level after 60 years of integration.

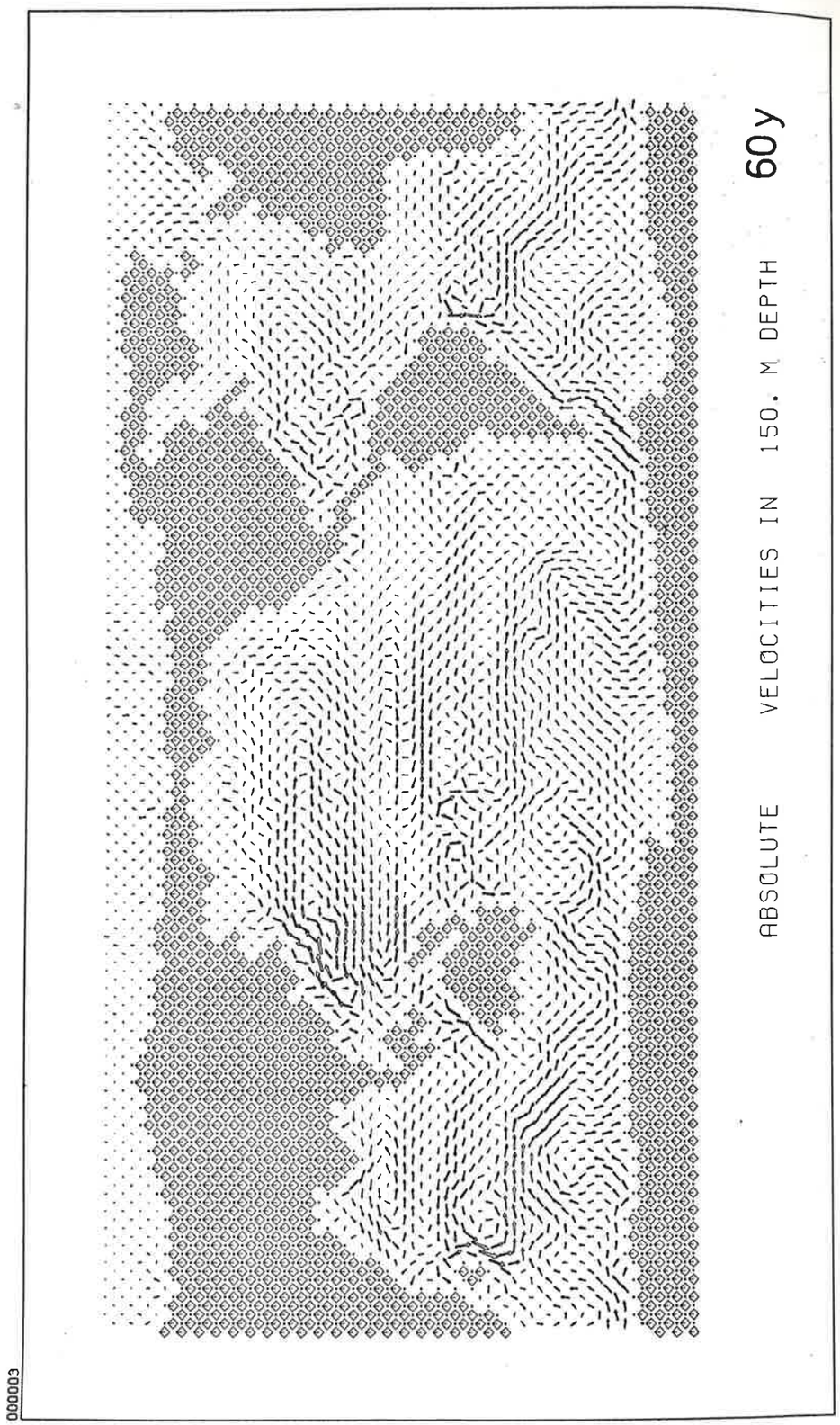

Fig. 5.16b Horizontal velocity at 150 m-level after 60 years of integration.

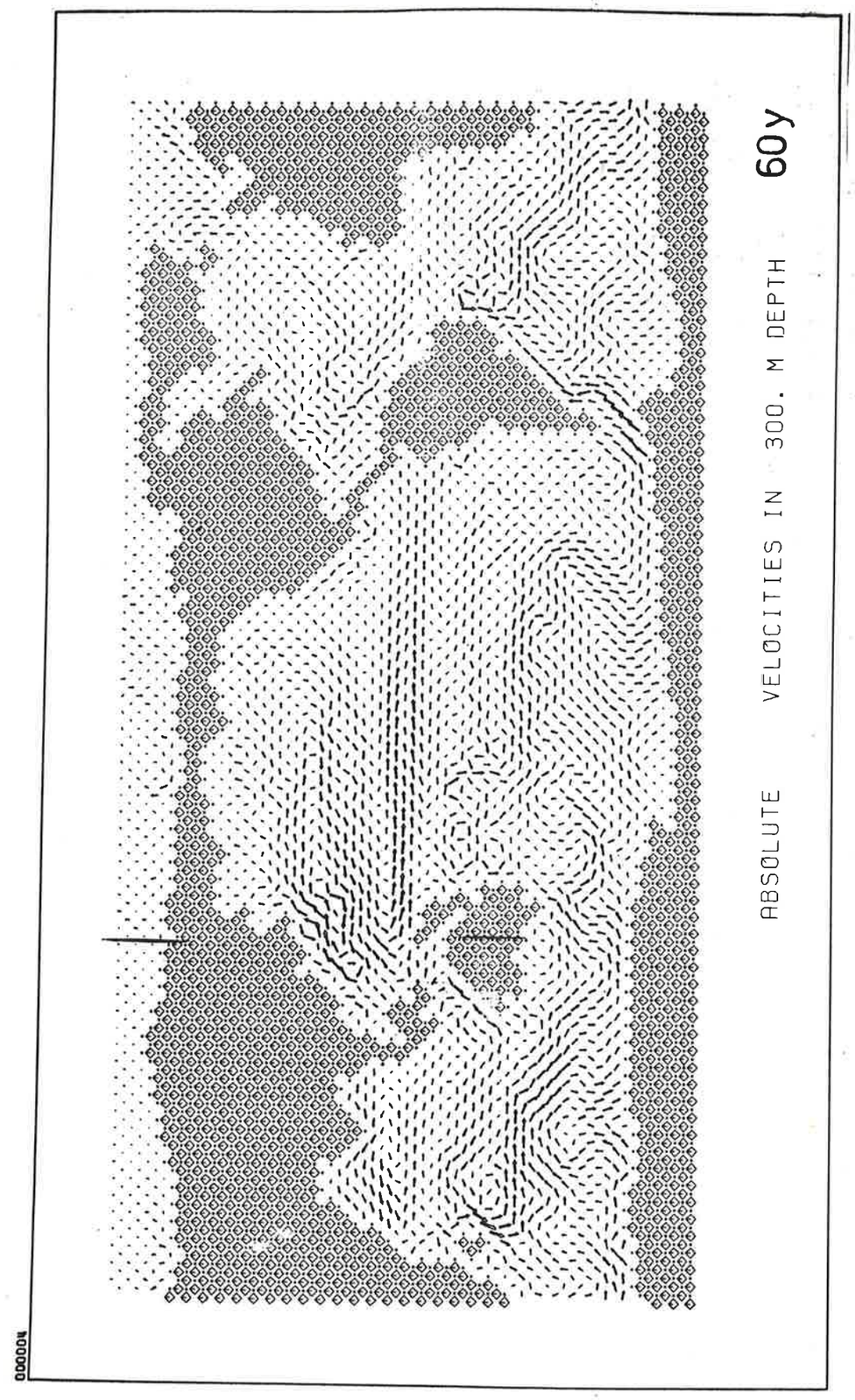

Fig. 5.16c Horizontal velocity at 300 m-level after 60 years of integration.

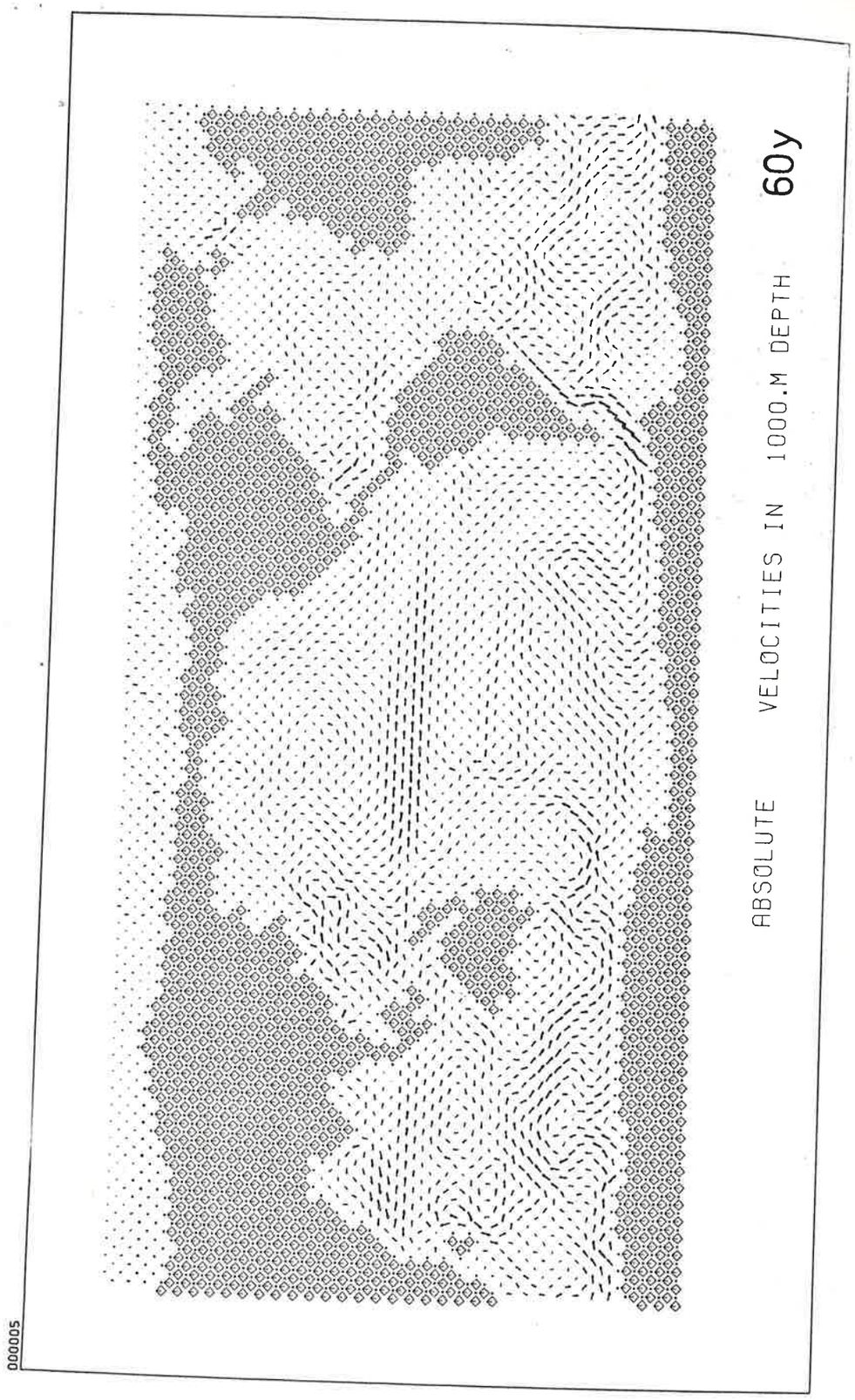

Fig. 5.16d Horizontal velocity at 1000 m-level after 60 years of integration.

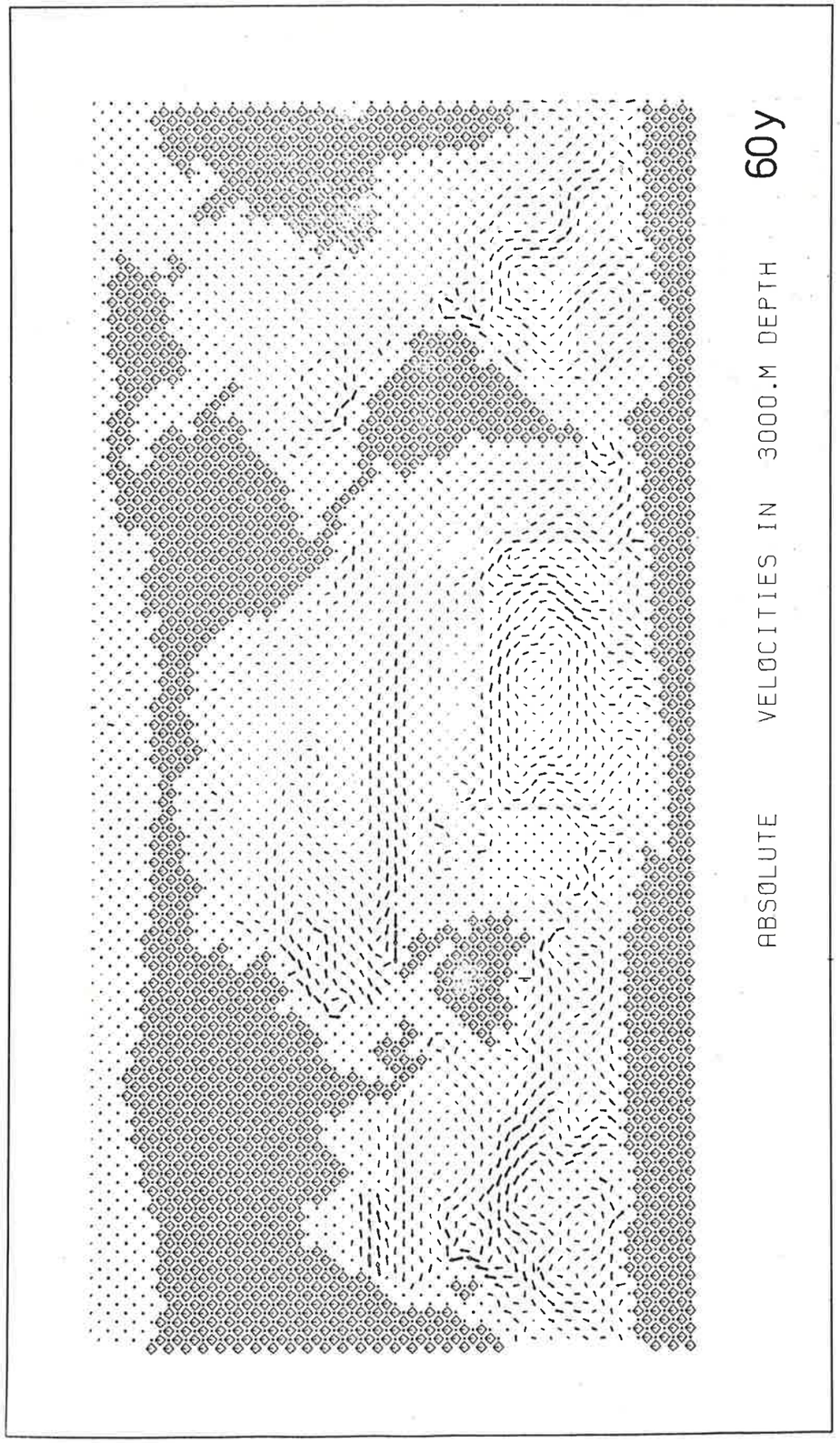

Fig. 5.16e Horizontal velocity at 3000 m-level after 60 years of integration.

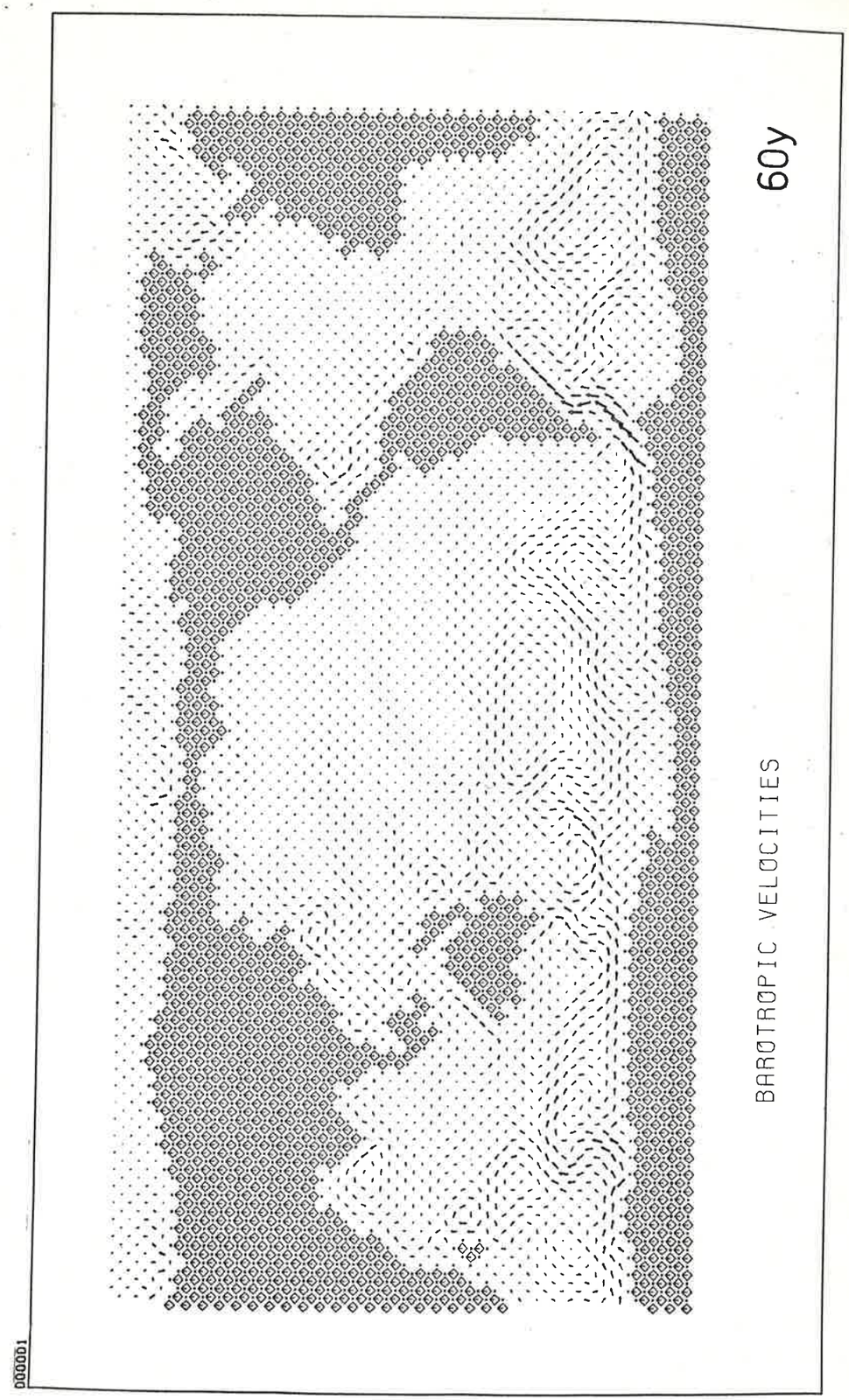

Fig. 5.16f Horizontal barotropic velocity after 60 years of integration.

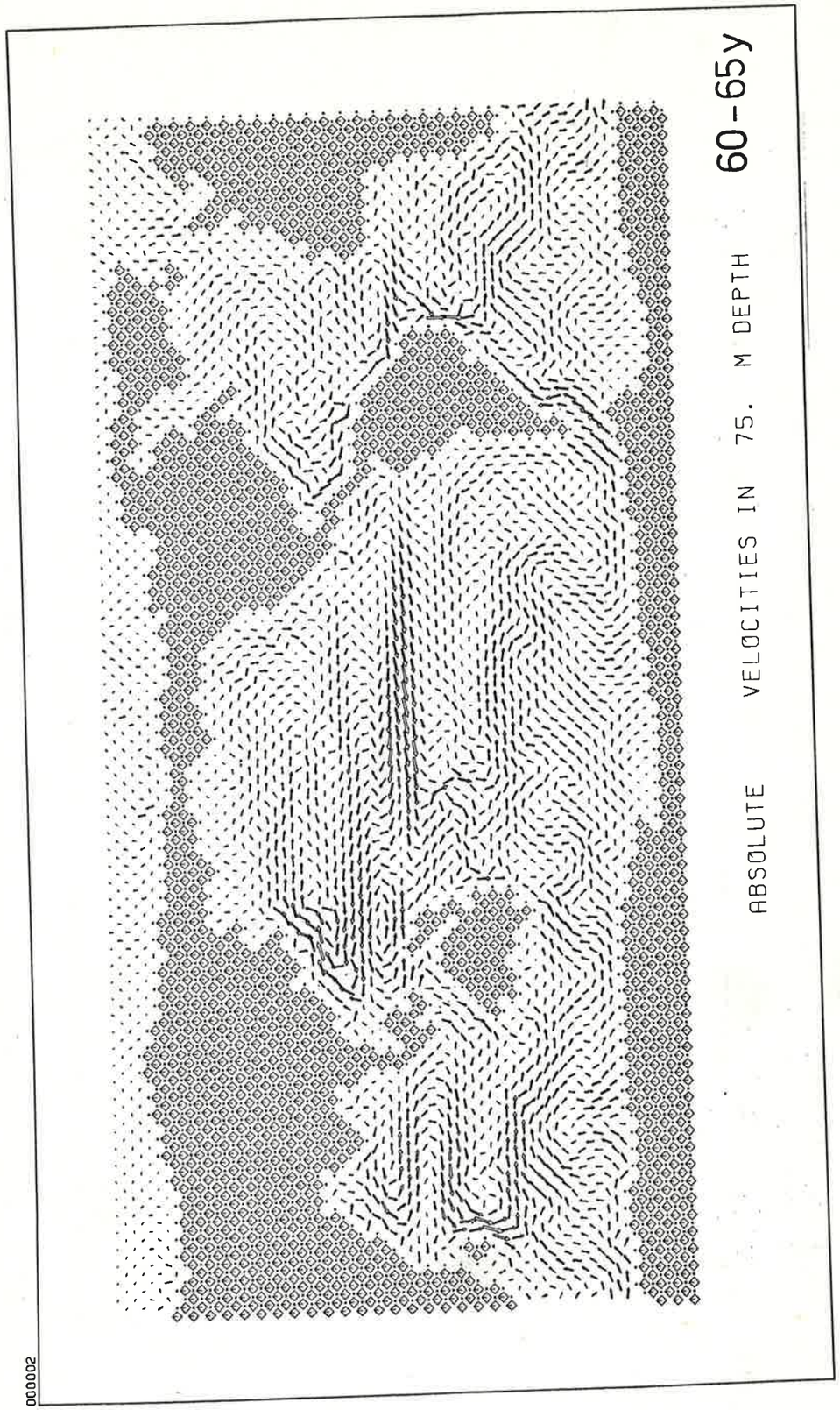

Fig. 5.17a Horizontal velocity at 75 m-level. Average over 60 years to 65 years integration period.

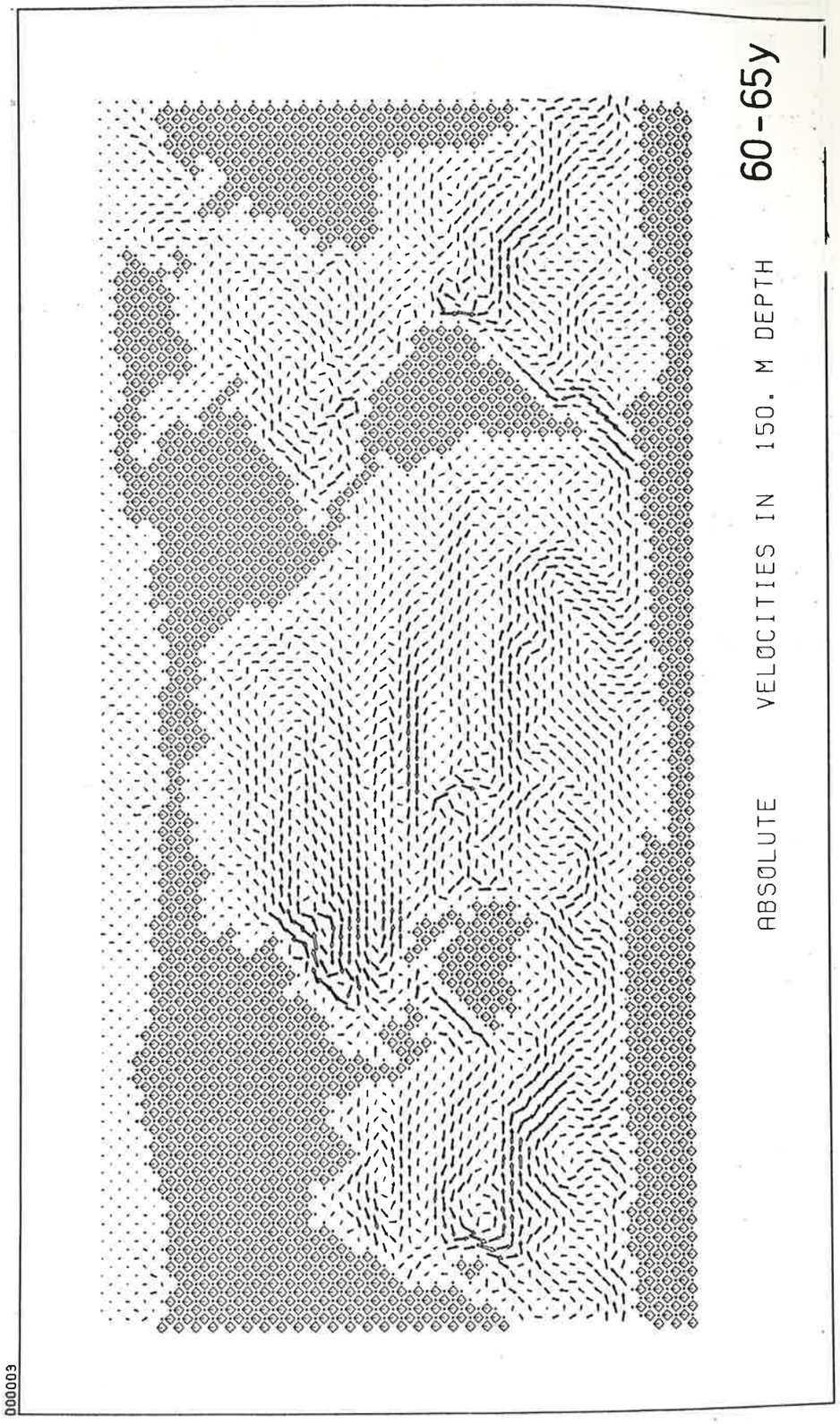

Fig. 5.17b Horizontal velocity at 150 m-level. Average over 60 years to 65 years integration period.

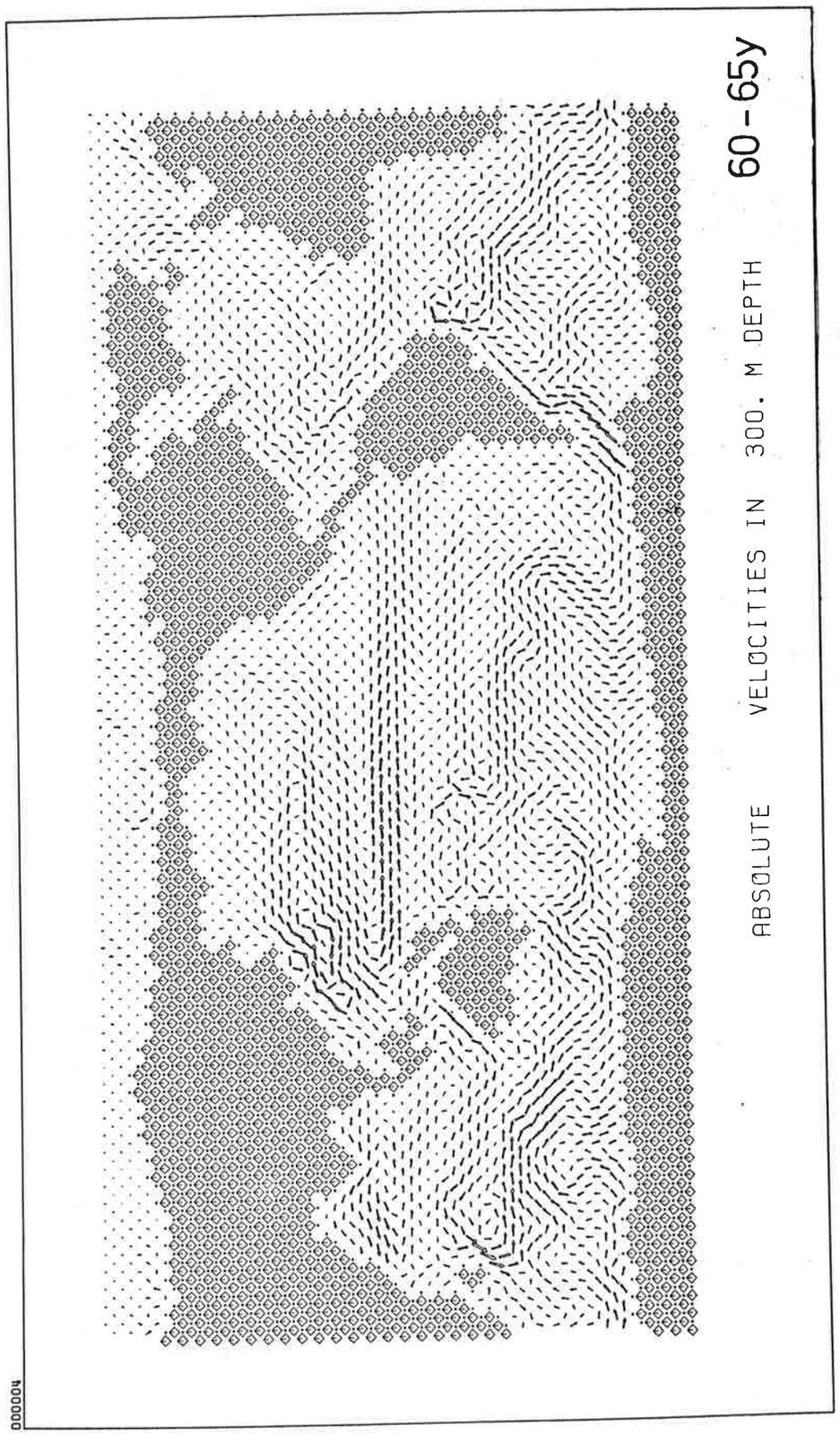

Fig. 5.17c Horizontal velocity at 300 m-level. Average over 60 years to 65 years integration period.

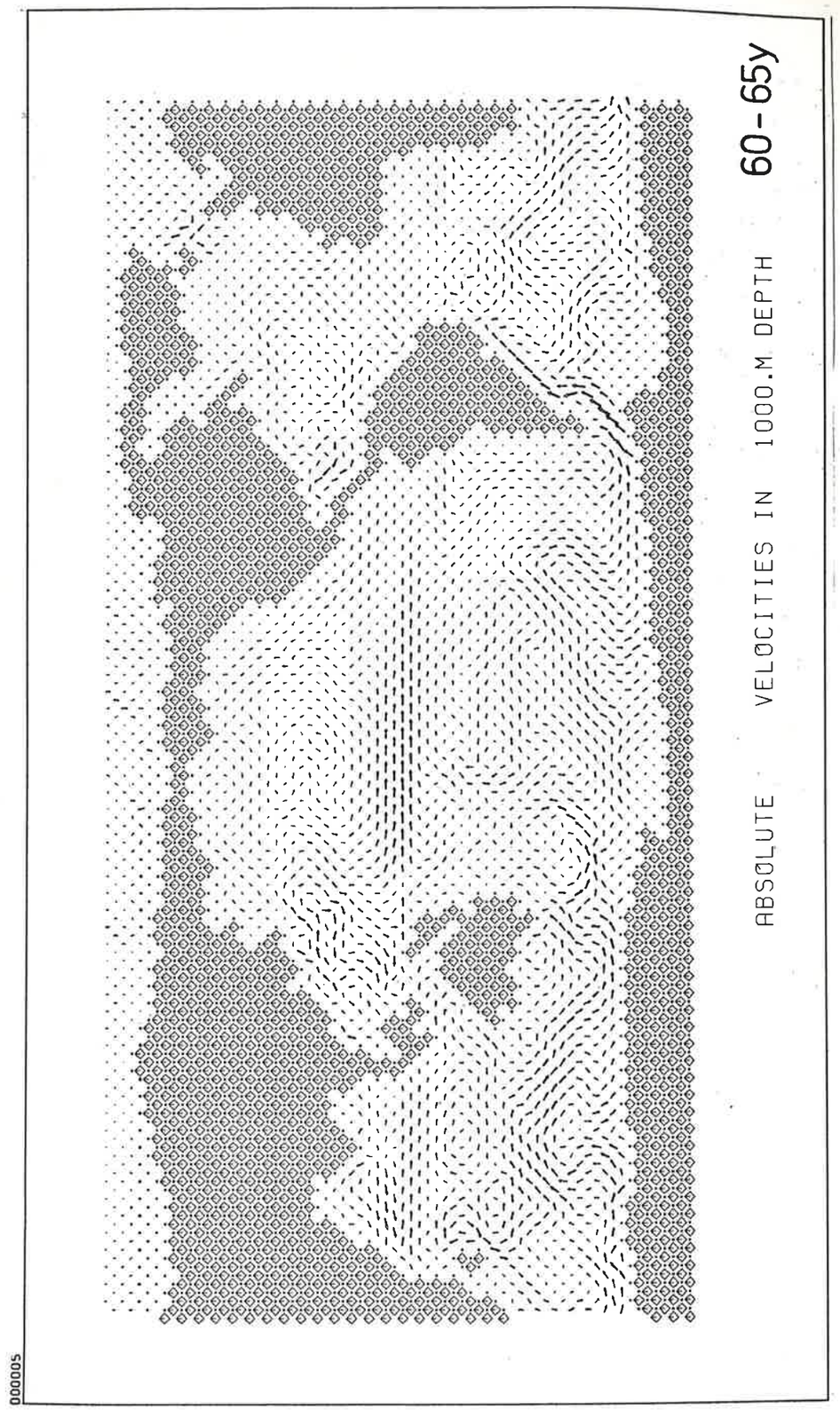

Fig. 5.17d Horizontal velocity at 1000 m-level. Average over 60 years to 65 years integration period.

Fig. 5.17e Horizontal velocity at 3000 m-level. Average over 60 years to 65 years integration period.

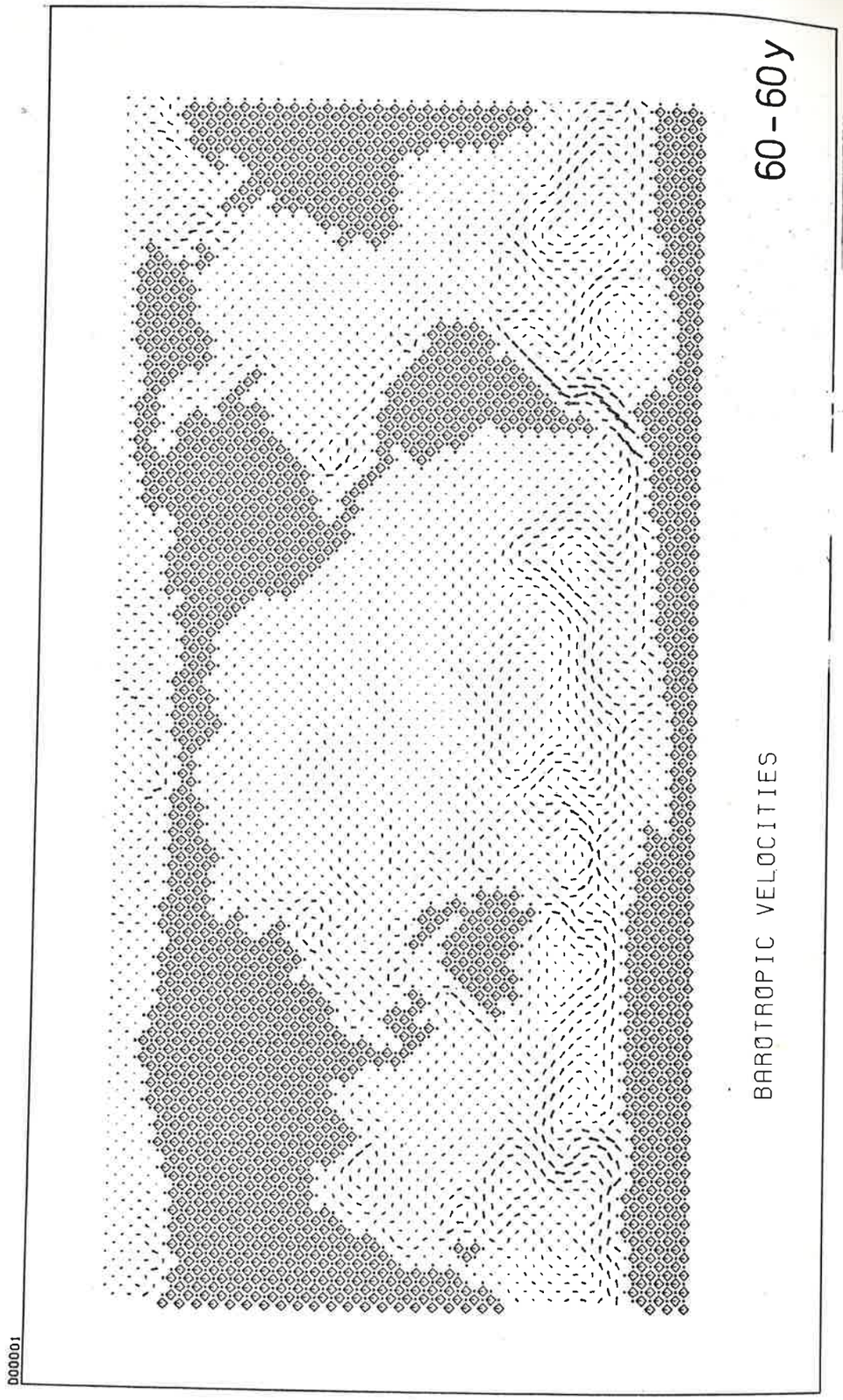

Fig. 5.17f Horizontal barotropic velocity. Average over 60 years to 65 years integration period.

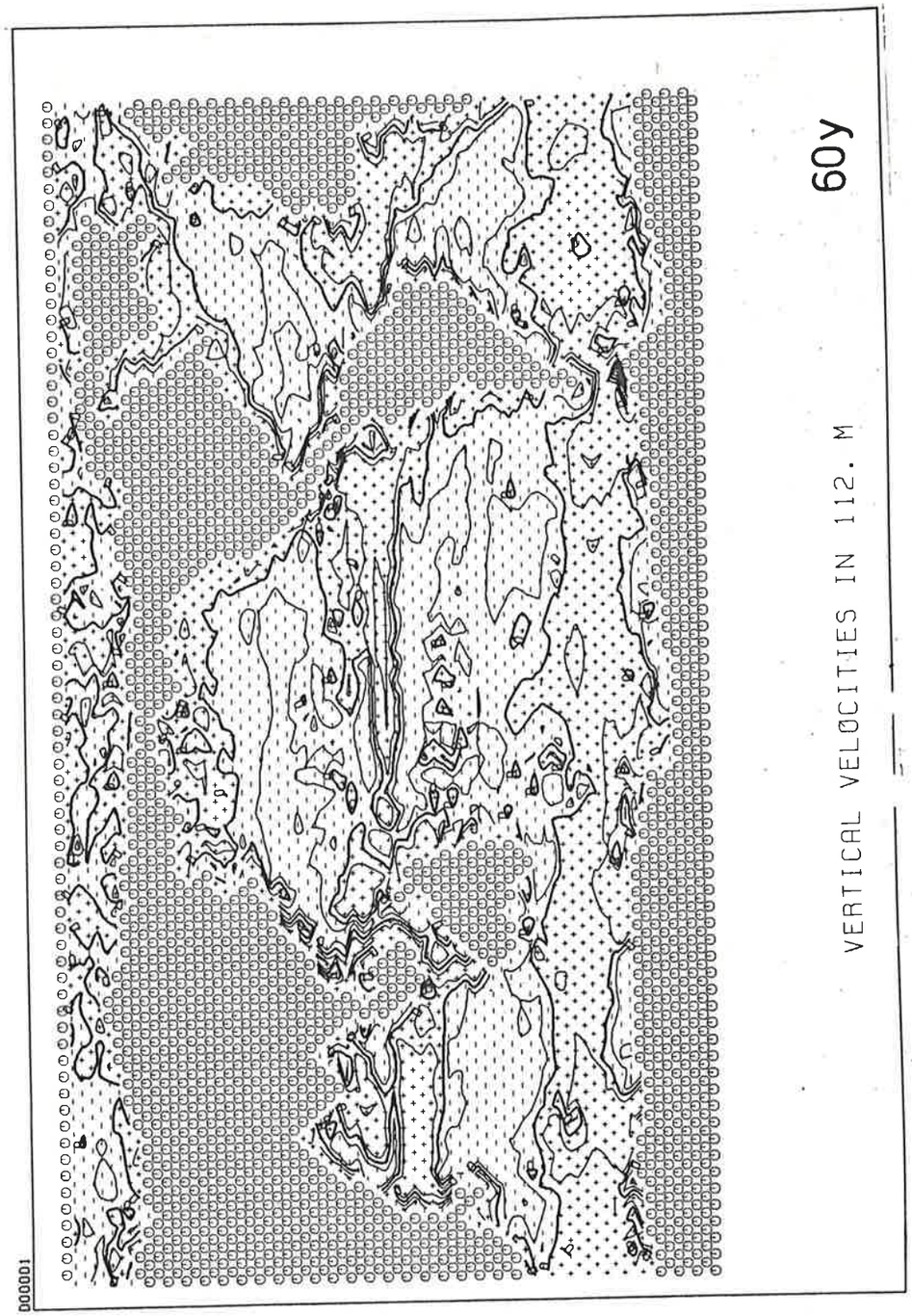

Fig. 5.18a Vertical velocity at 112 m-level after 60 years of integration.

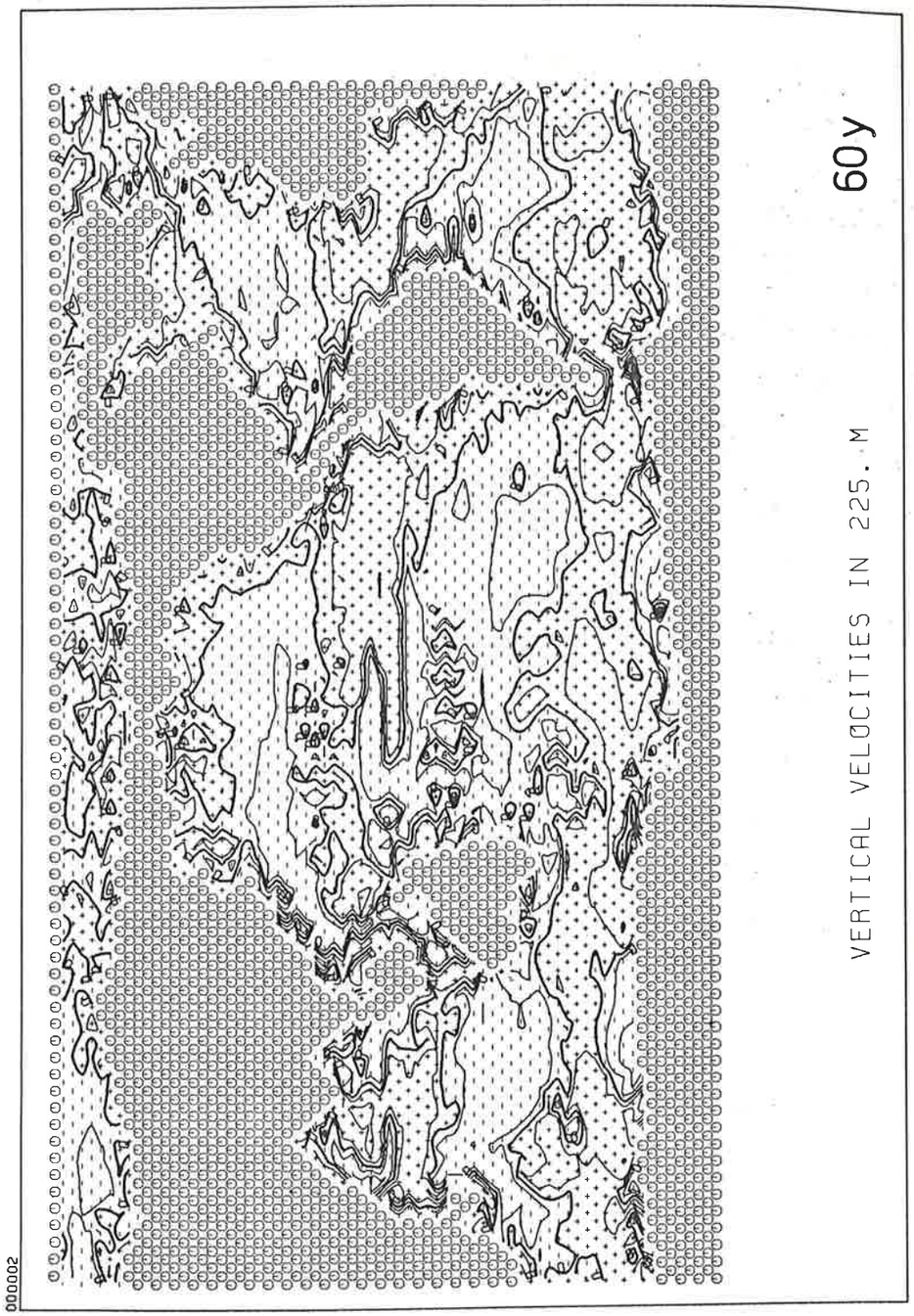

Fig. 5.18b Vertical velocity at 225 m-level after 60 years of integration.

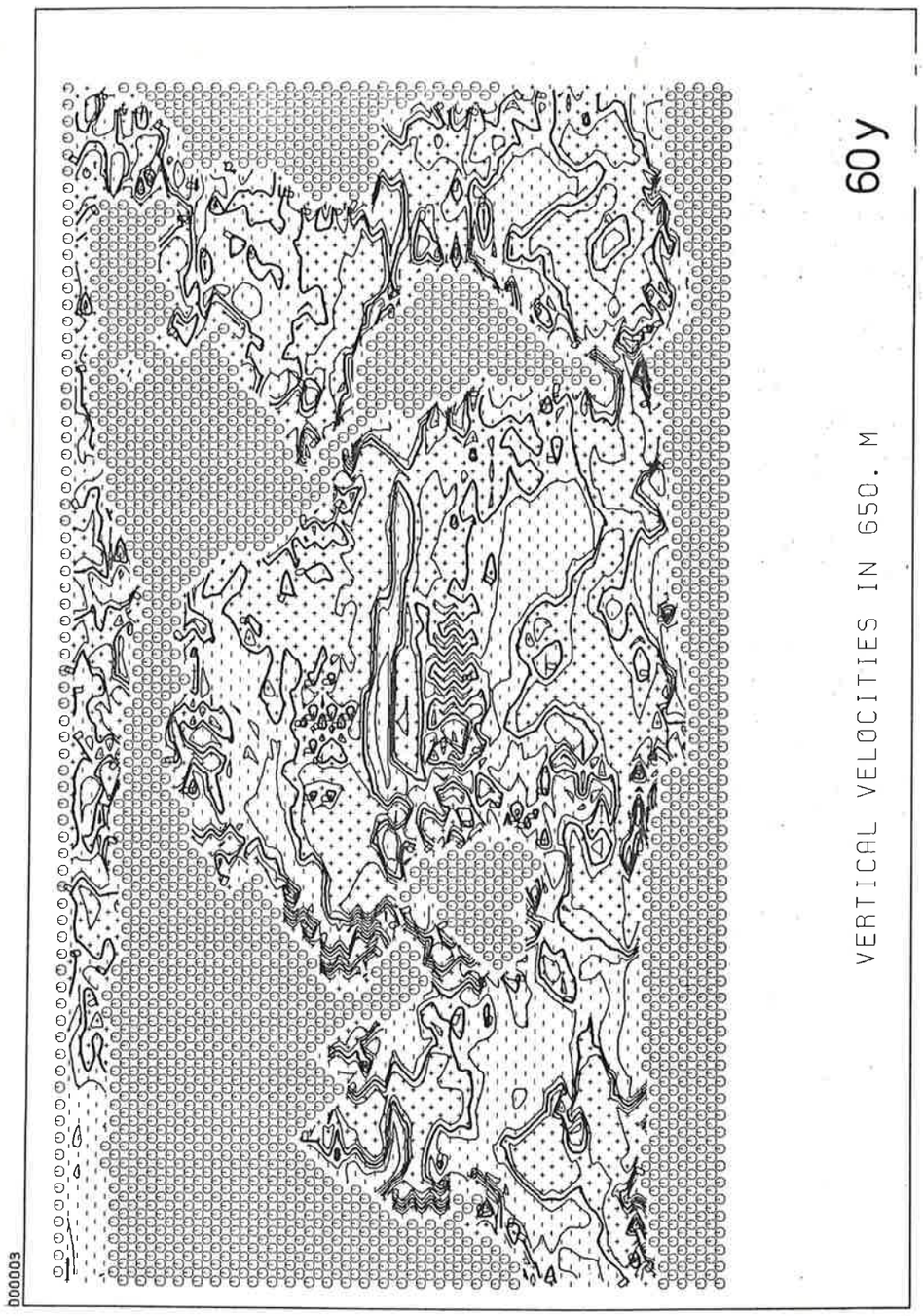

Fig. 5.18c Vertical velocity at 650 m-level after 60 years of integration.

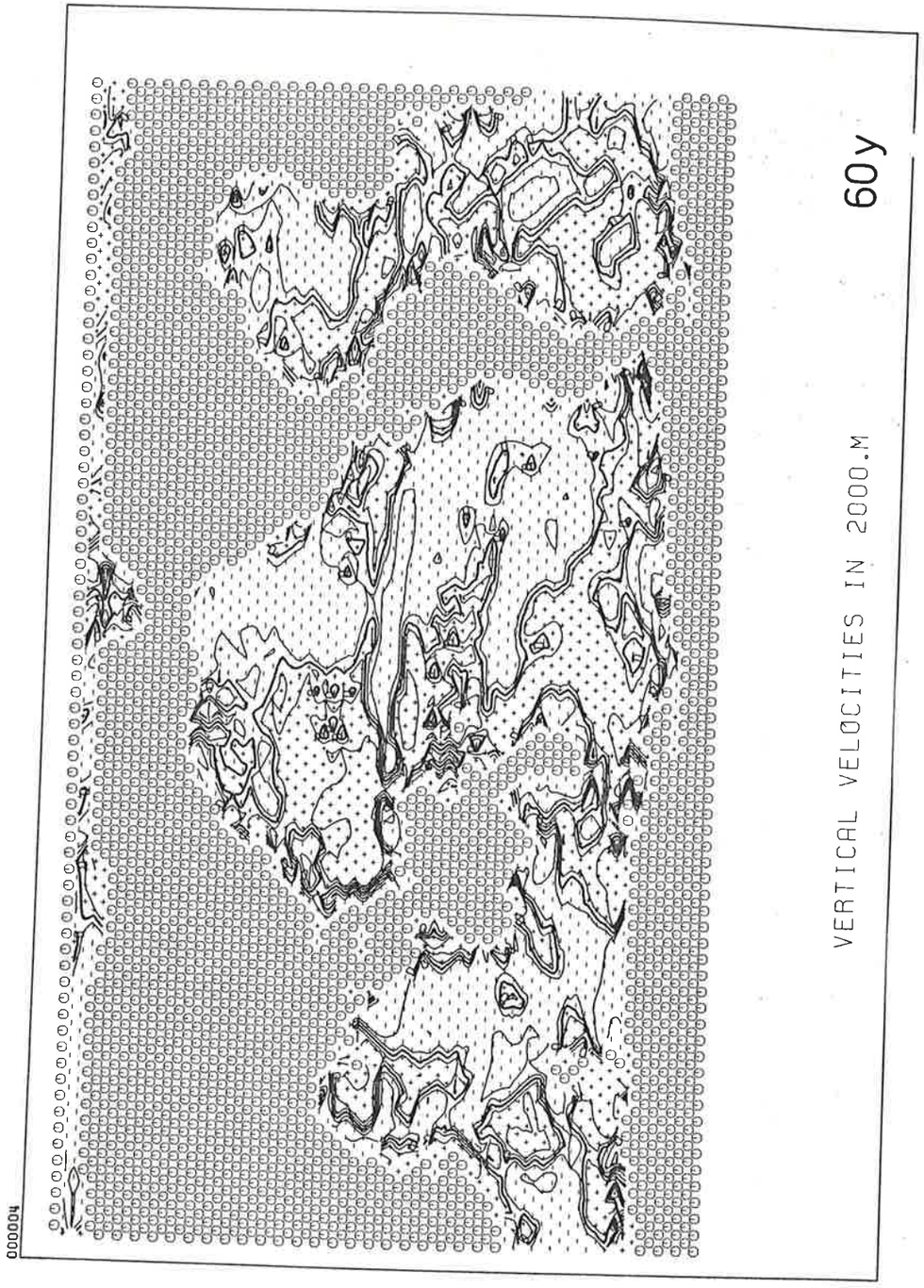

Fig. 5.18d Vertical velocity at 2000 m-level after 60 years of integration.

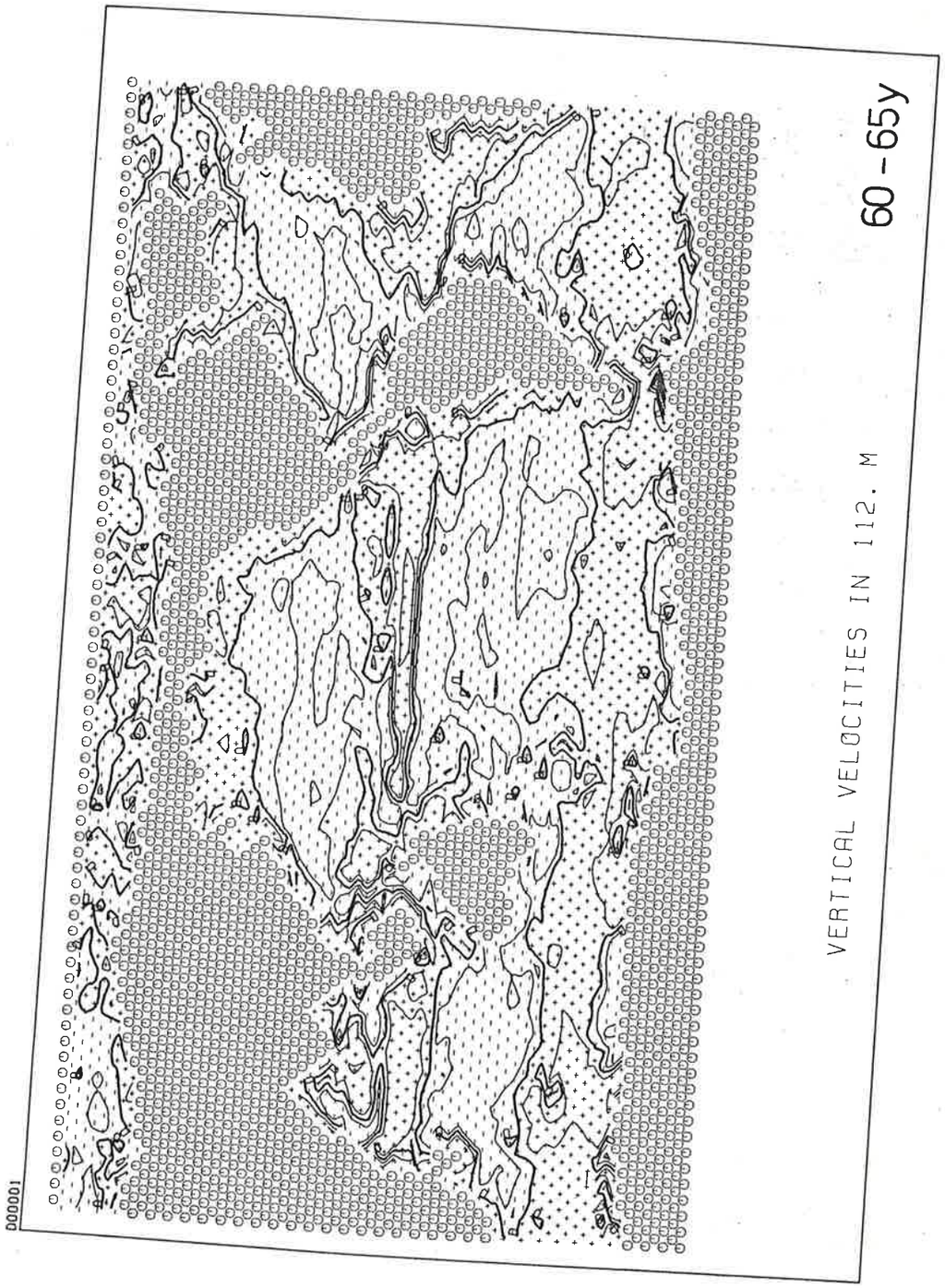

Fig. 5.19a Vertical velocity at 112 m-level. Average over 60 years to 65 years integration period.

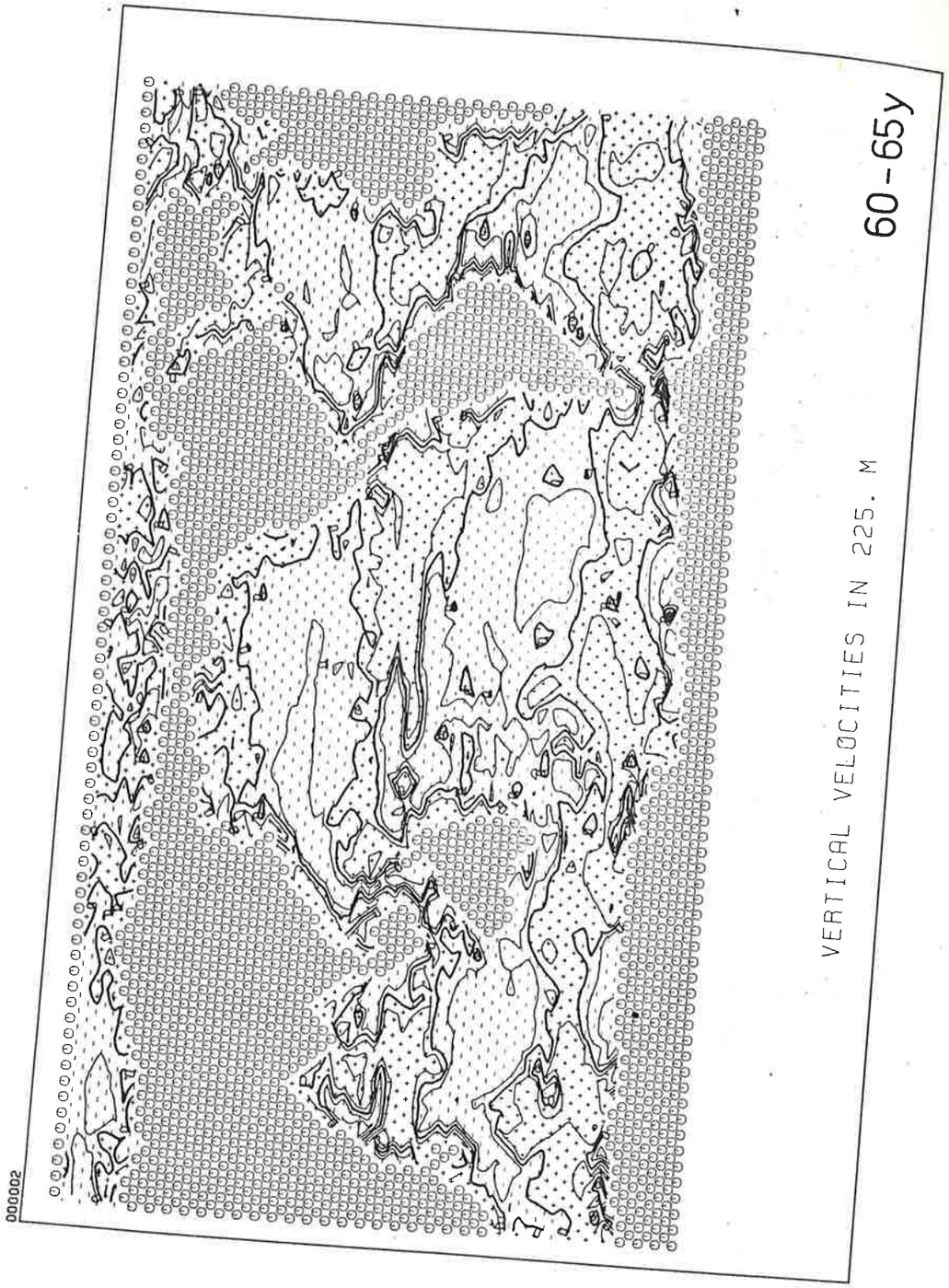

Fig. 5.19b Vertical velocity at 225 m-level. Average over 60 years to 65 years integration period.

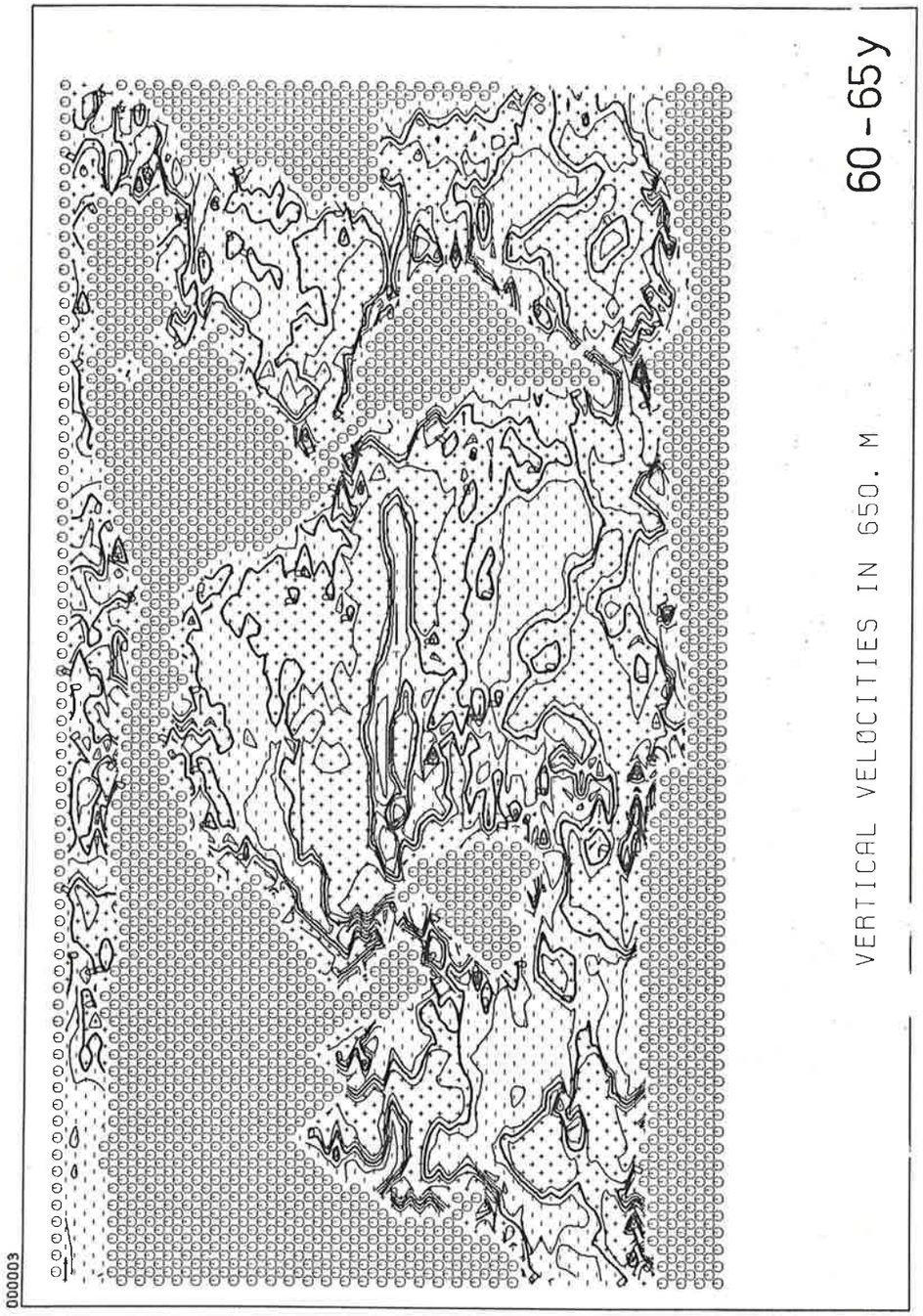

Fig. 5.19c Vertical velocity at 650 m-level. Average over 60 years to 65 years integration period.

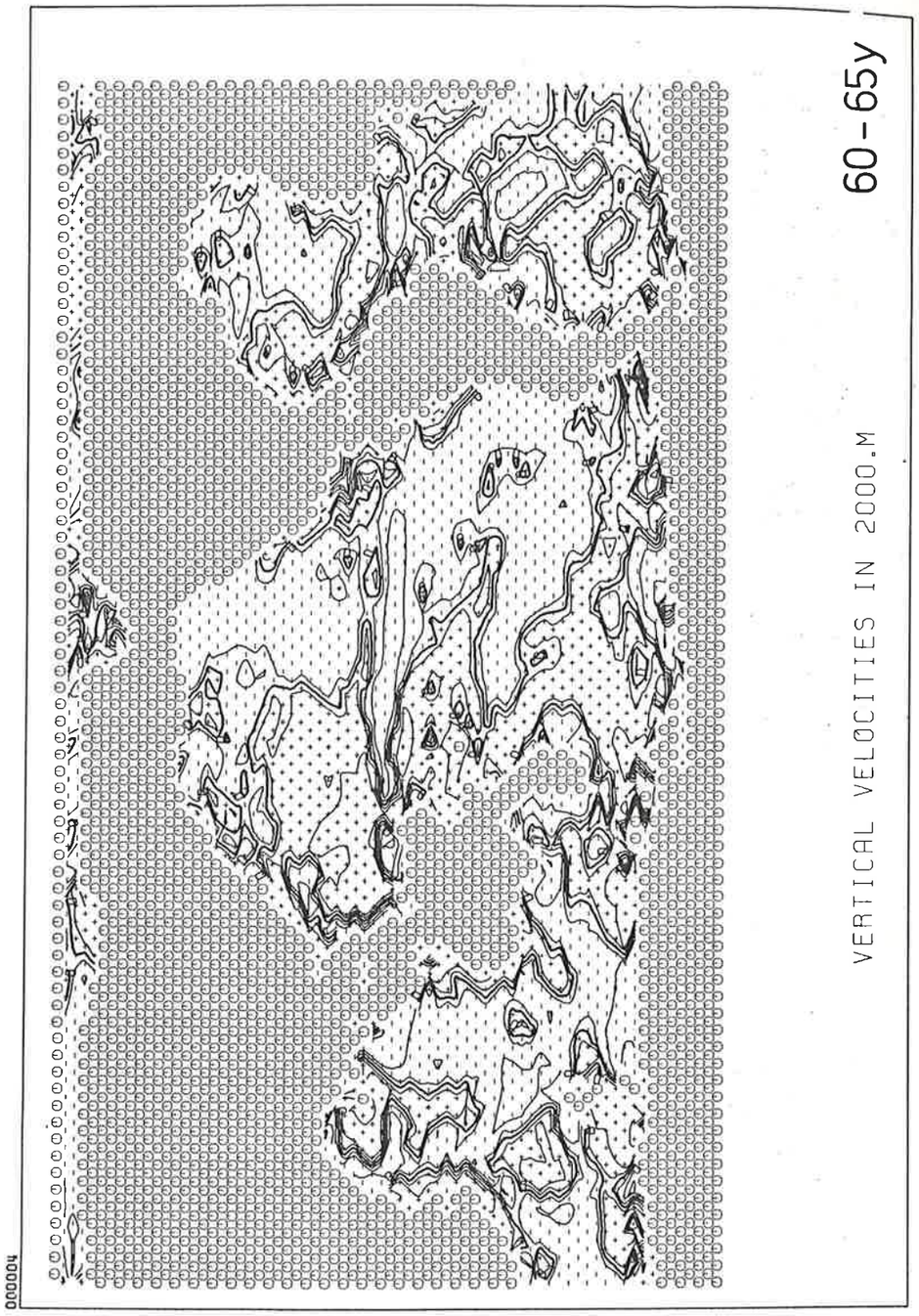

Fig. 5.19d Vertical velocity at 2000 m-level. Average over 60 years to 65 years integration period.

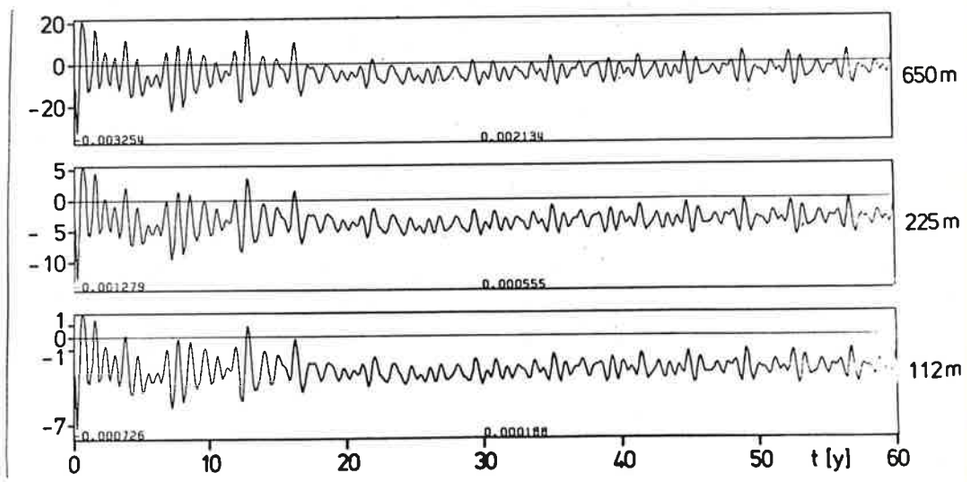

Fig. 5.20a Time series of vertical velocity at 20° N on section 1 for different levels.

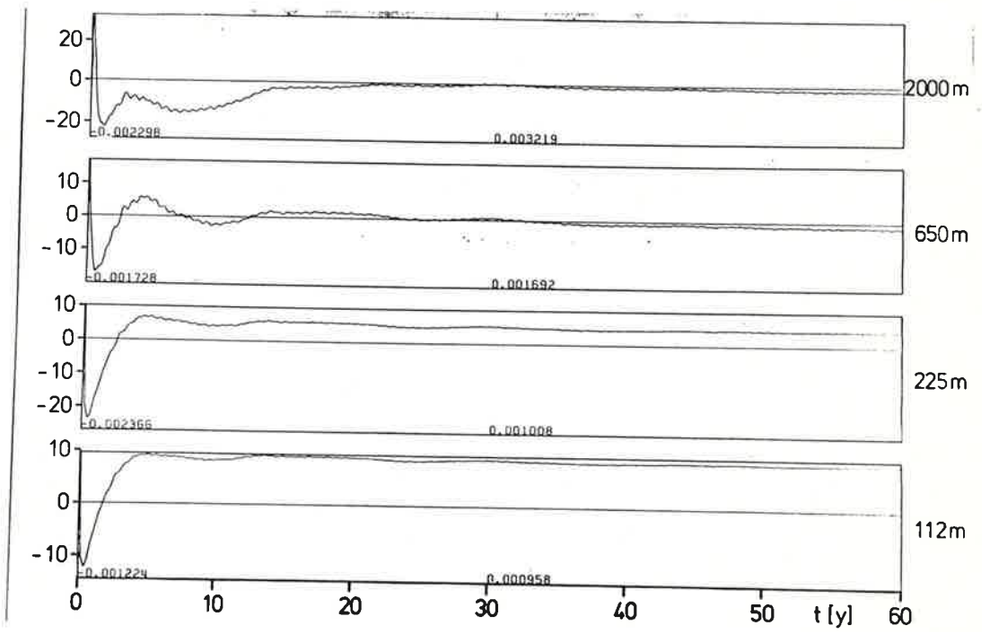

Fig. 5.20b Time series of vertical velocity at 1° N on section 1 for different levels.

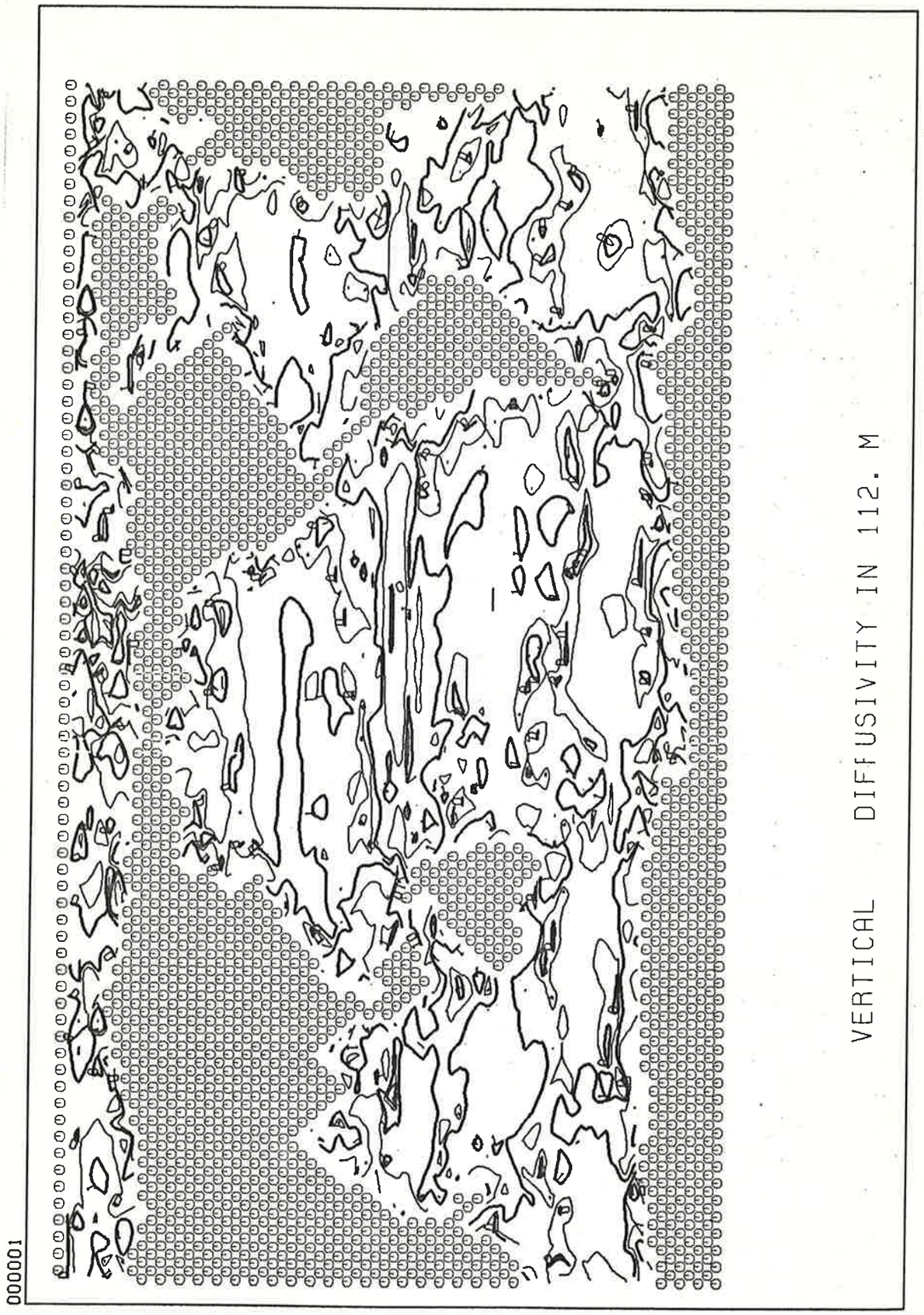

Fig. 5.21a Numerical vertical diffusivity at 112 m-level computed for the 60 years velocity field.

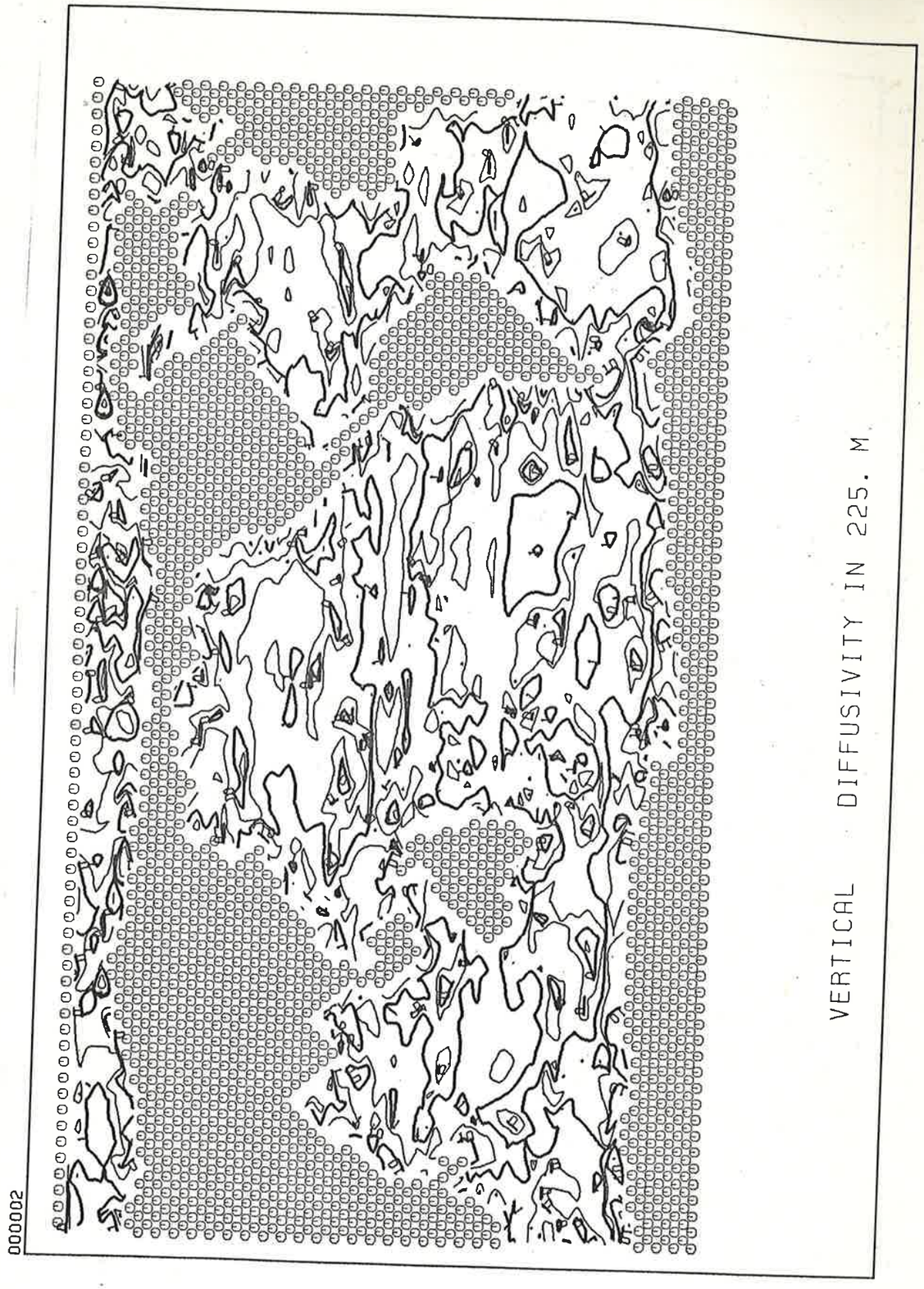

Fig. 5.21b Numerical vertical diffusivity at 225 m-level computed for the 60 years velocity field.

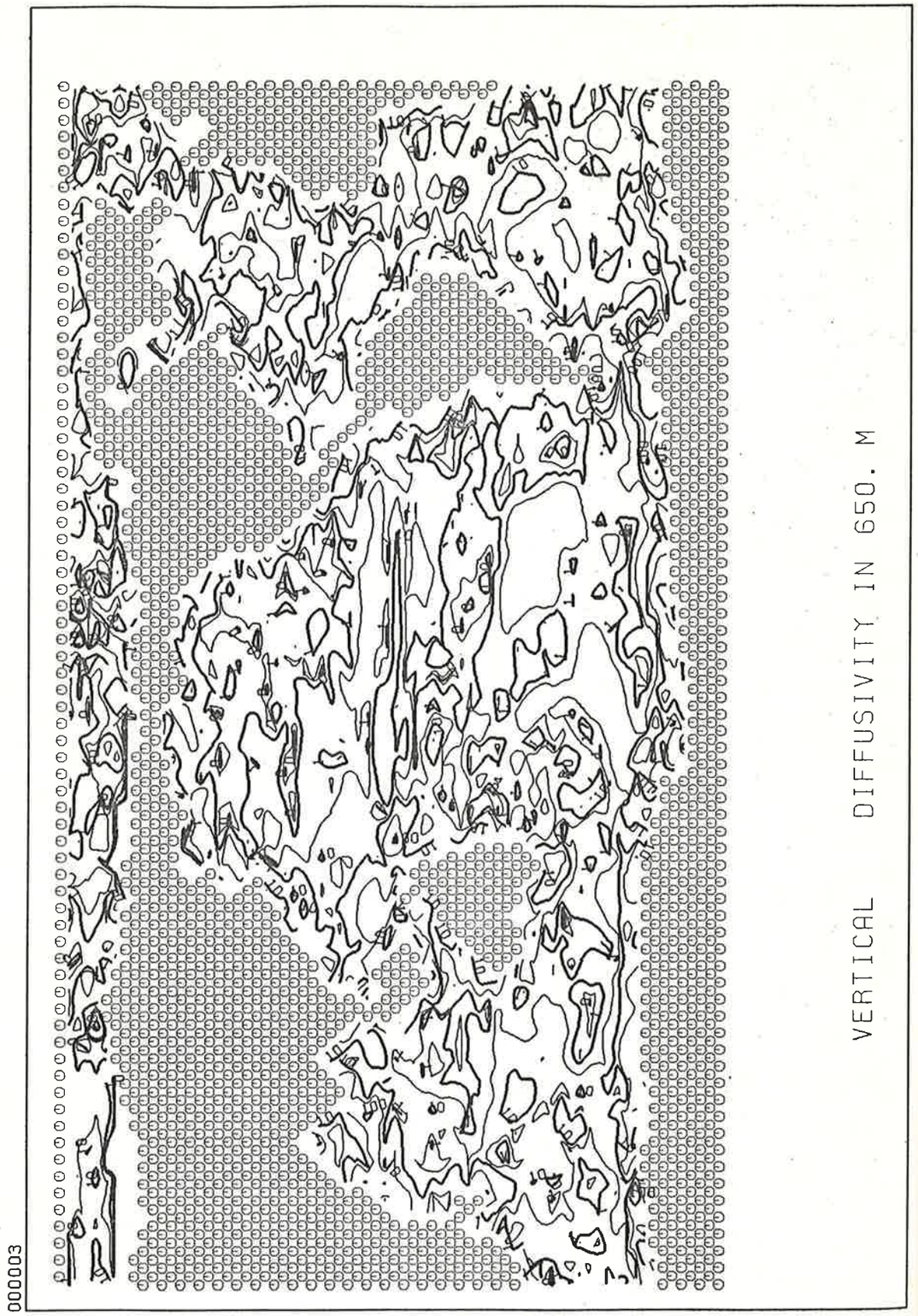

Fig. 5.21c Numerical vertical diffusivity at 650 m-level computed for the 60 years velocity field.

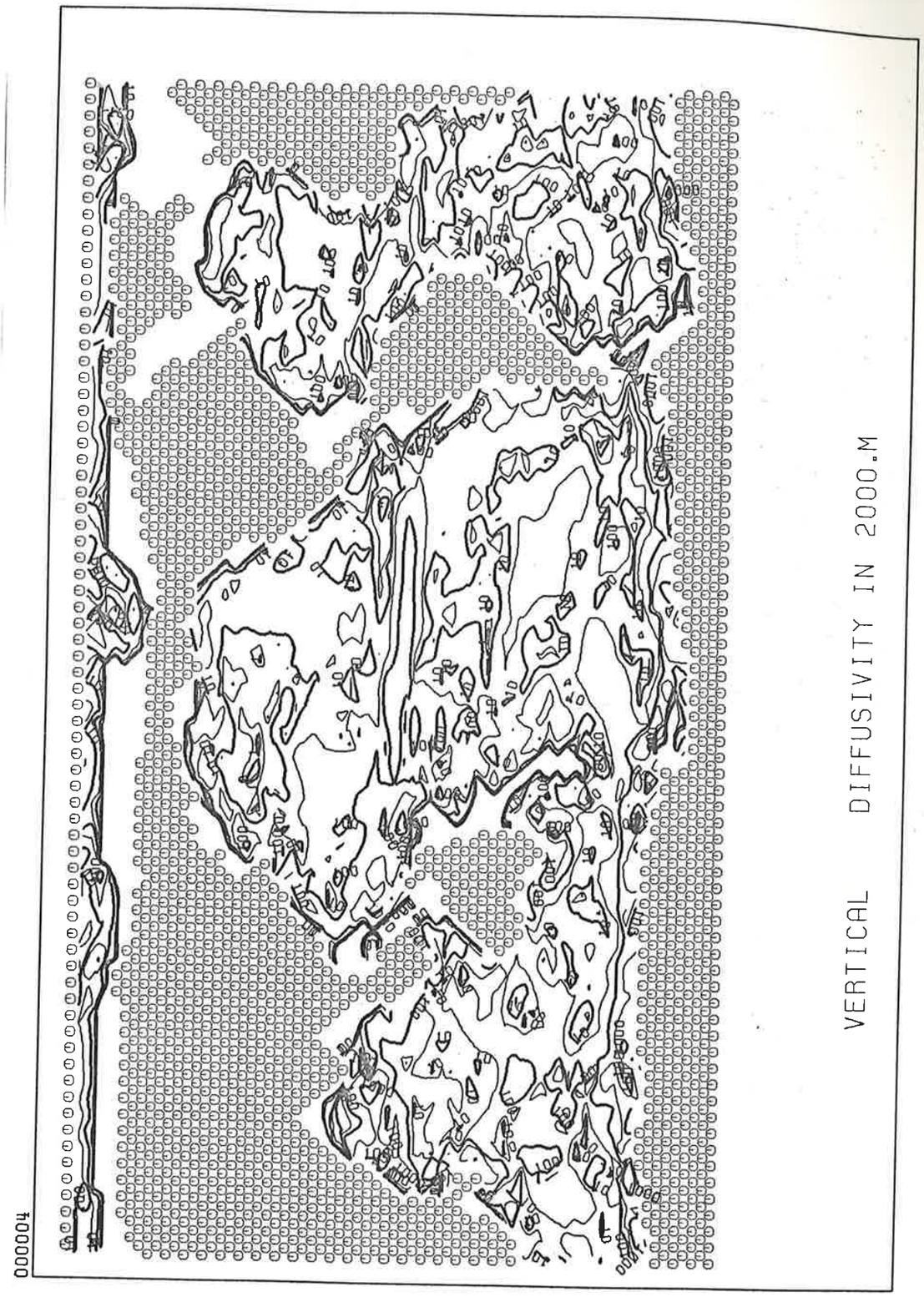

Fig. 5.21d Numerical vertical diffusivity at 2000 m-level computed for the 60 years velocity field.

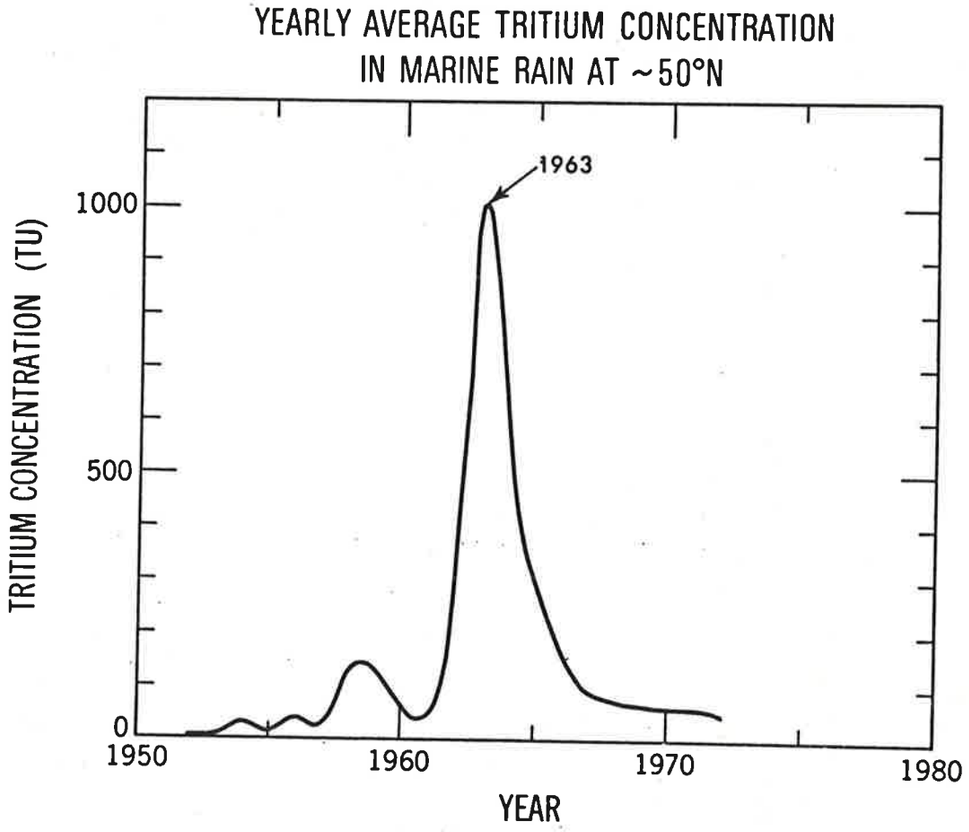

Fig. 6.1 Tritium in rainfall at ~ 50° N (Weiss et al., 1979). This illustrates the temporal pattern of the input to the oceans.

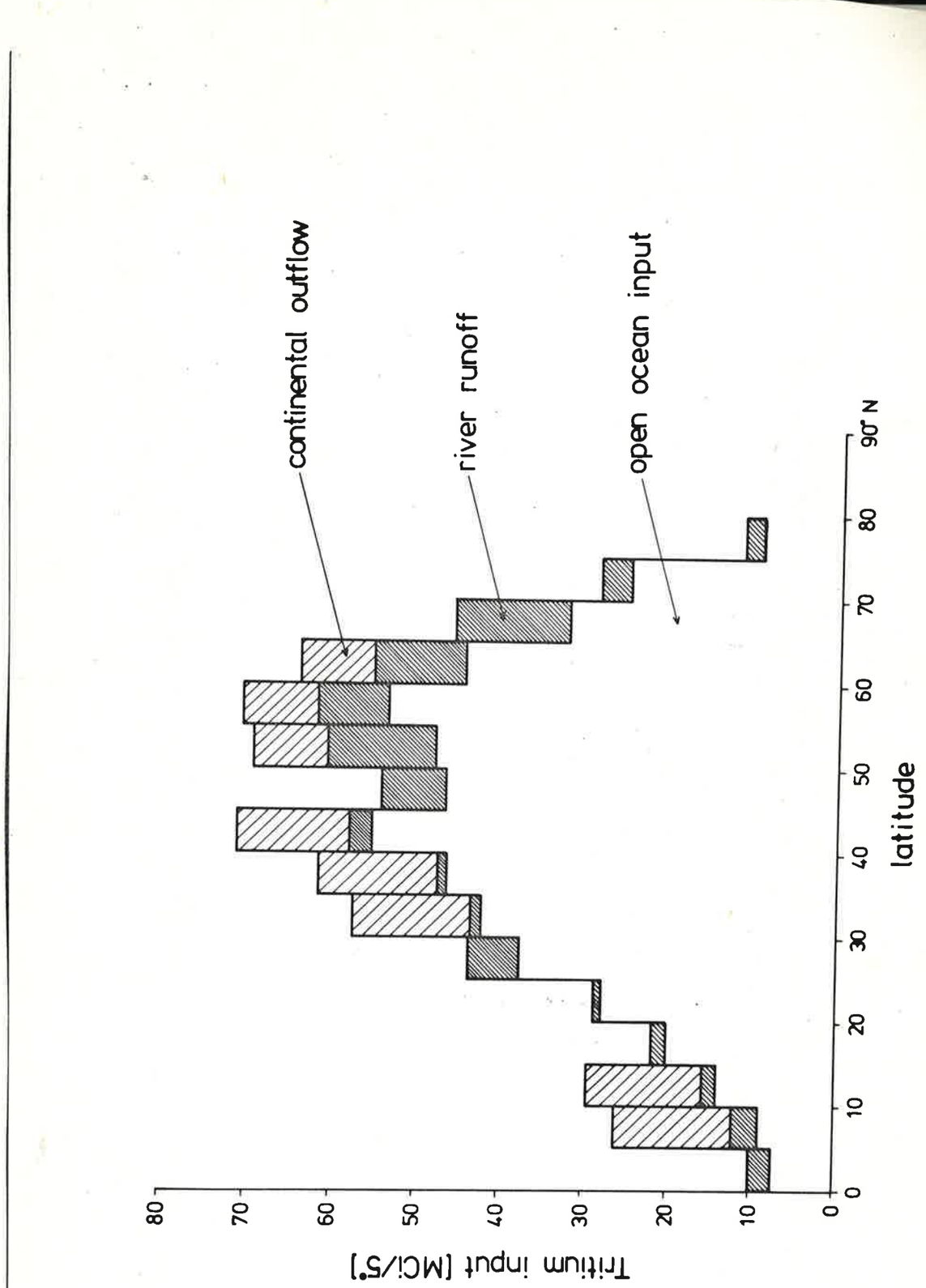

Fig. 6.2 Total input of tritium to the ocean up to 1972. The figure shows the contributions of open ocean input, river runoff, and water vapor transport from continents.

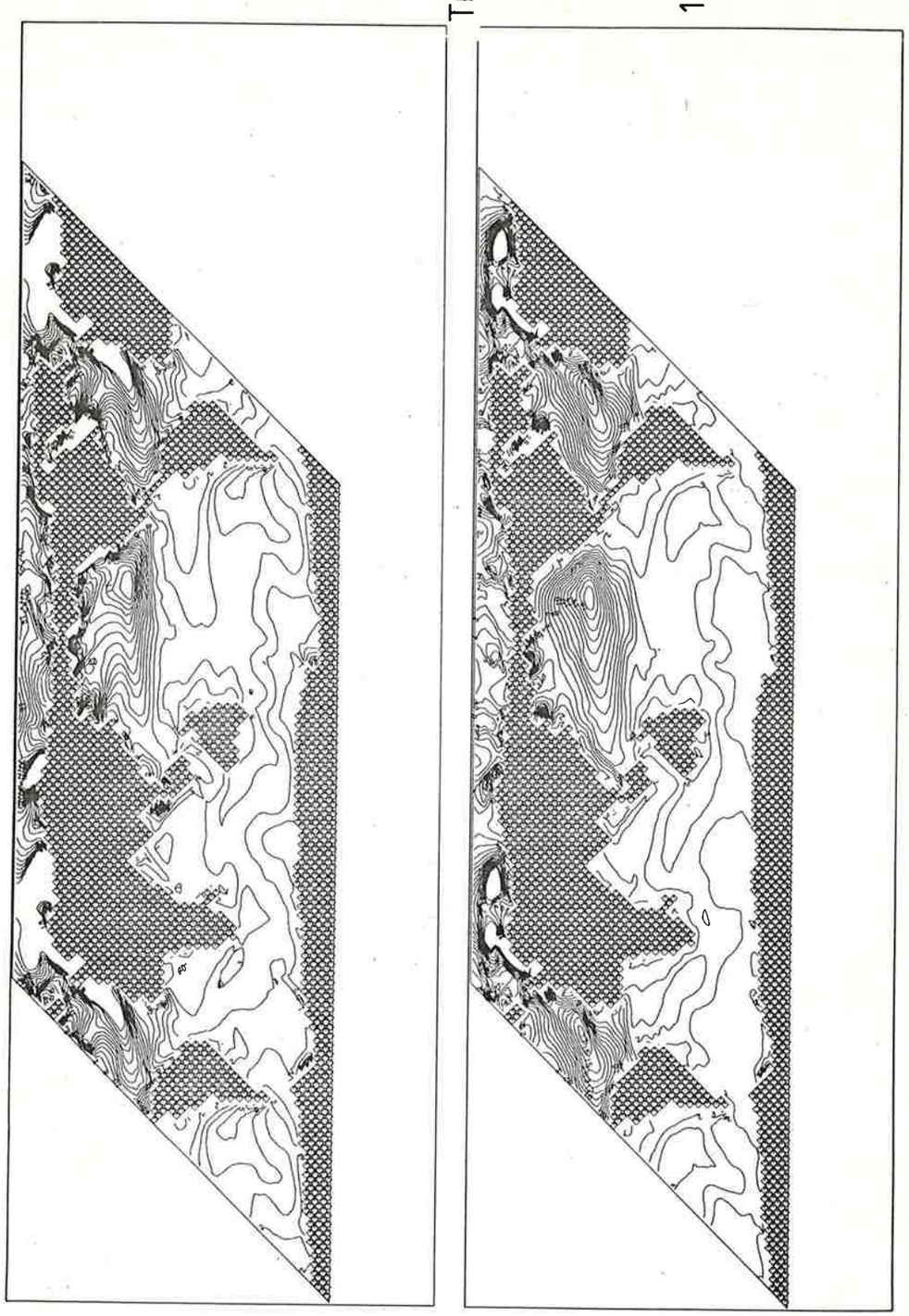

Fig. 6.3a Tritium at 75 m- and 150 m-level for 1972. Diffusive simulation.

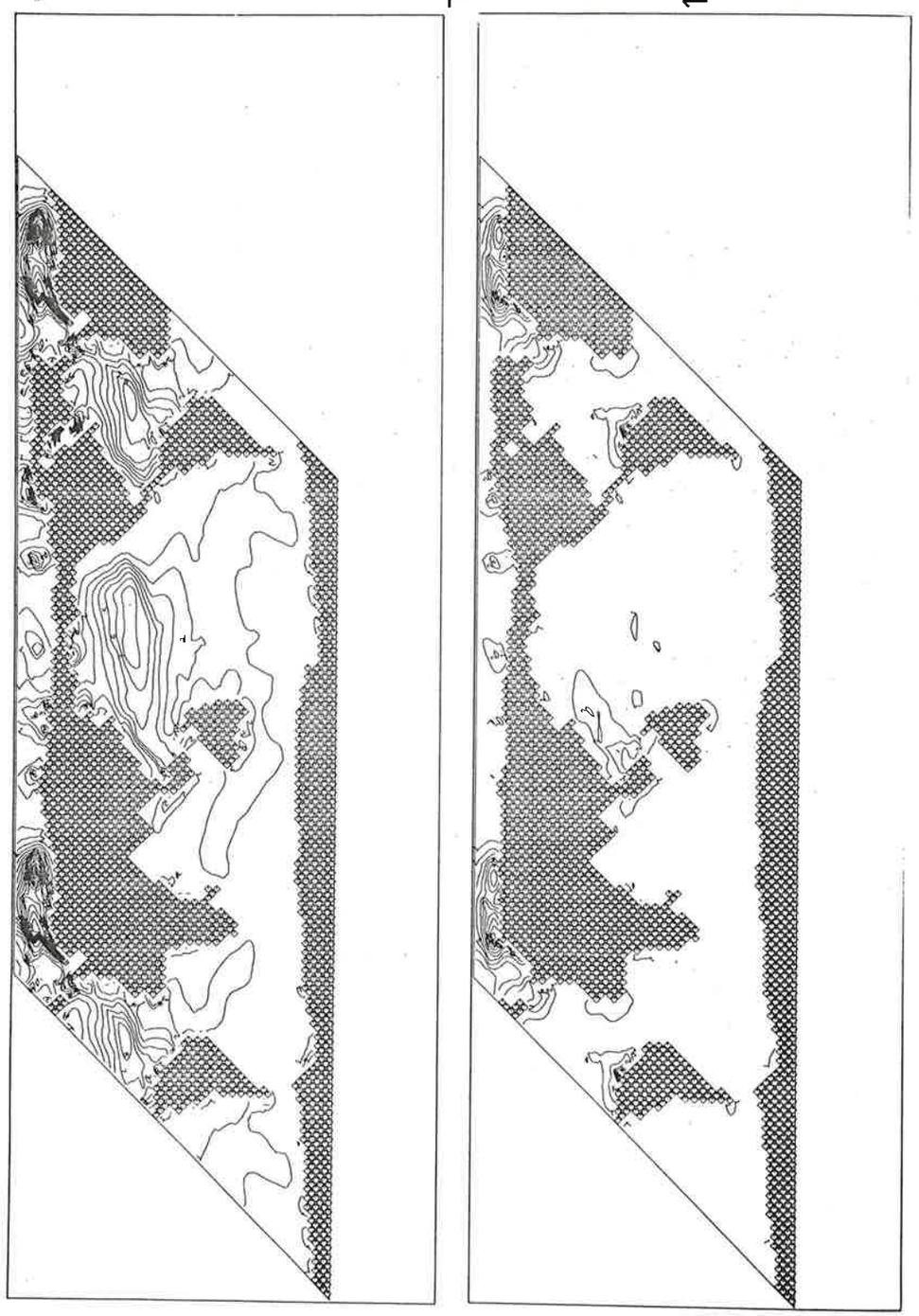

Fig. 6.3b Tritium at 300 m- and 1000 m-level for 1972. Diffusive simulation.

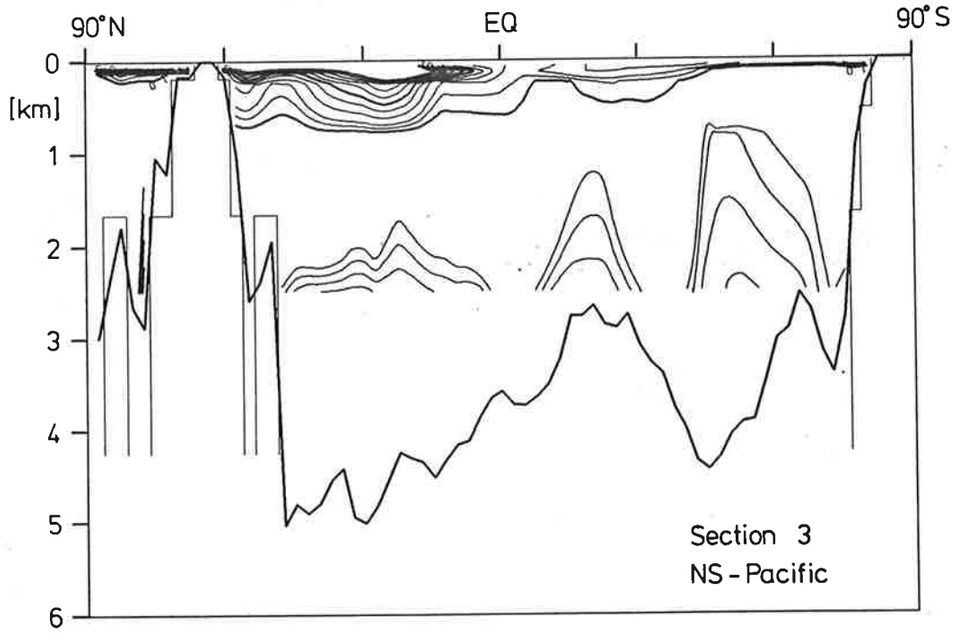

Fig. 6.4 Tritium along section 3 for 1972. Diffusive simulation.

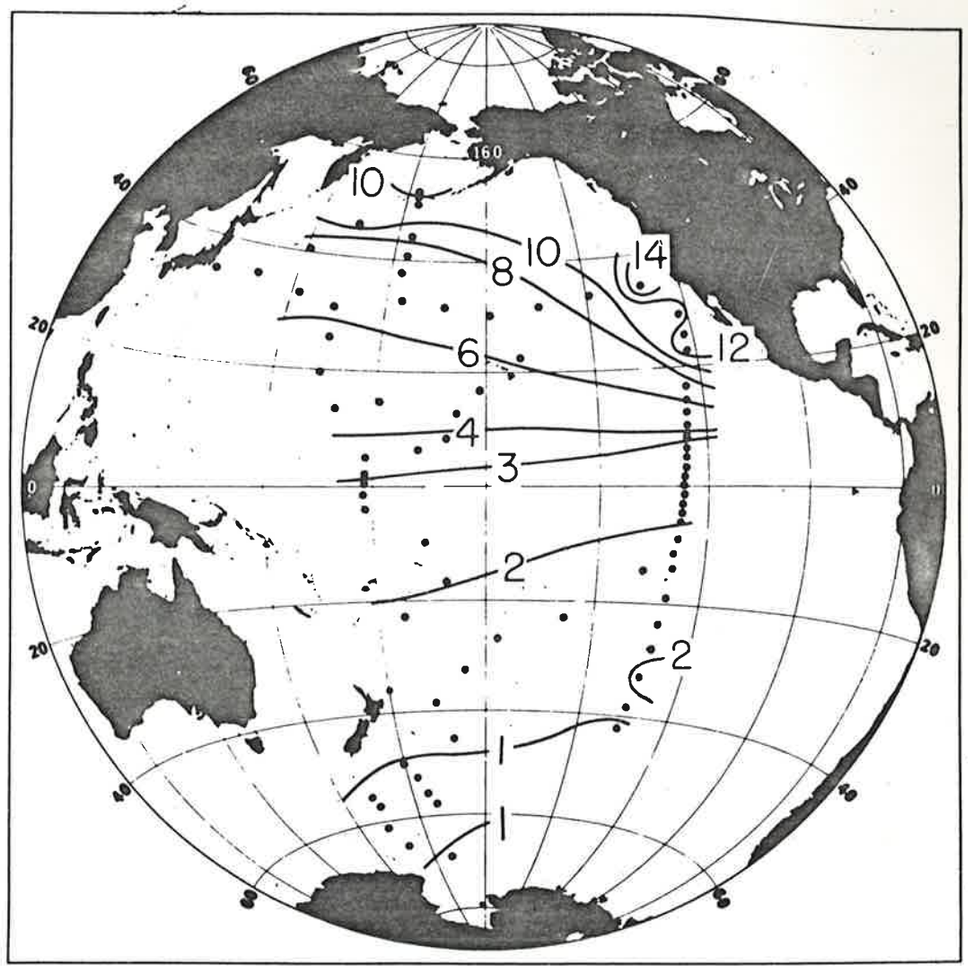

Fig. 6.5a Observed tritium concentration at the surface. (Fine et al., 1981).

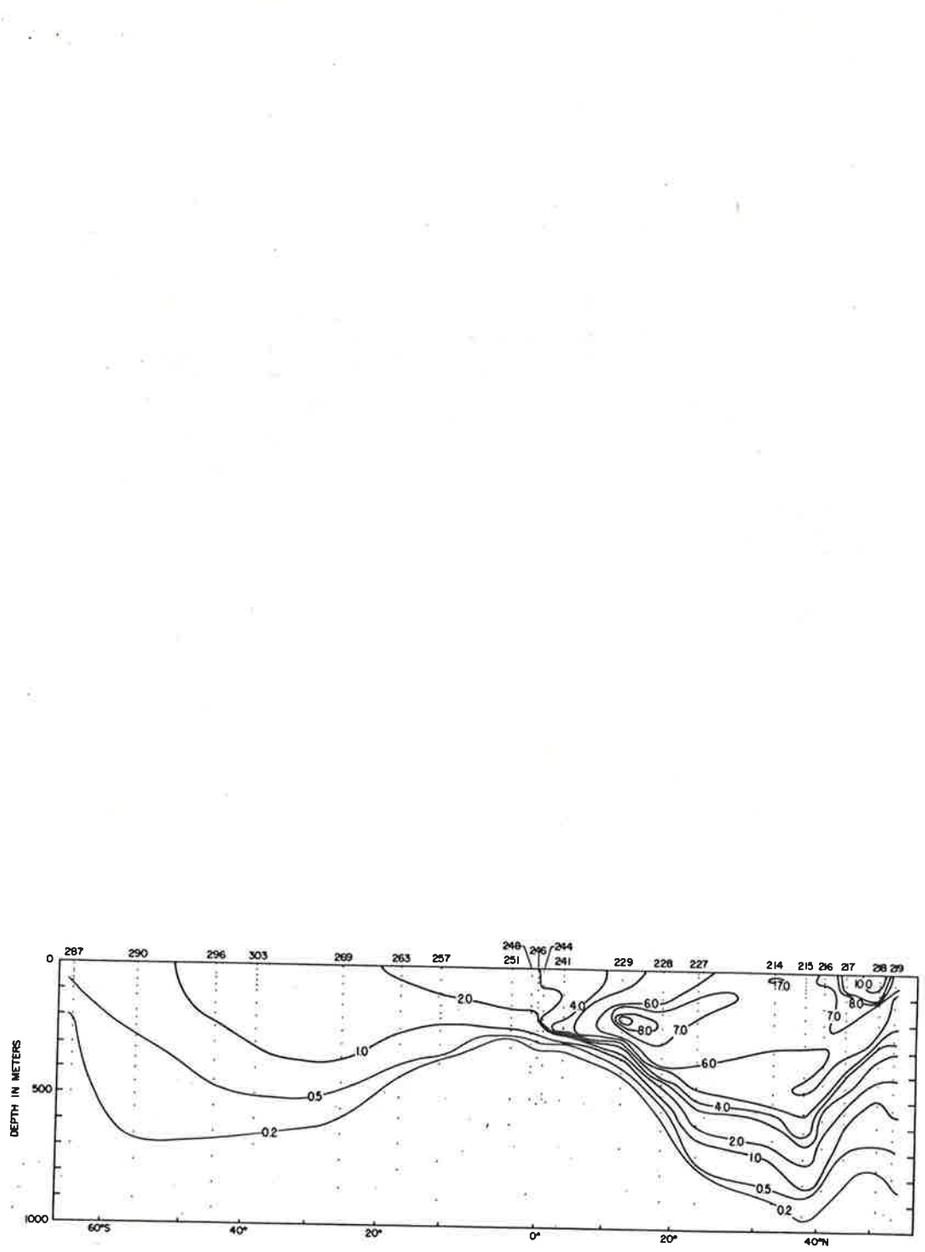

Fig. 6.5b North-south section of tritium in the western Pacific (Fine et al., 1981).

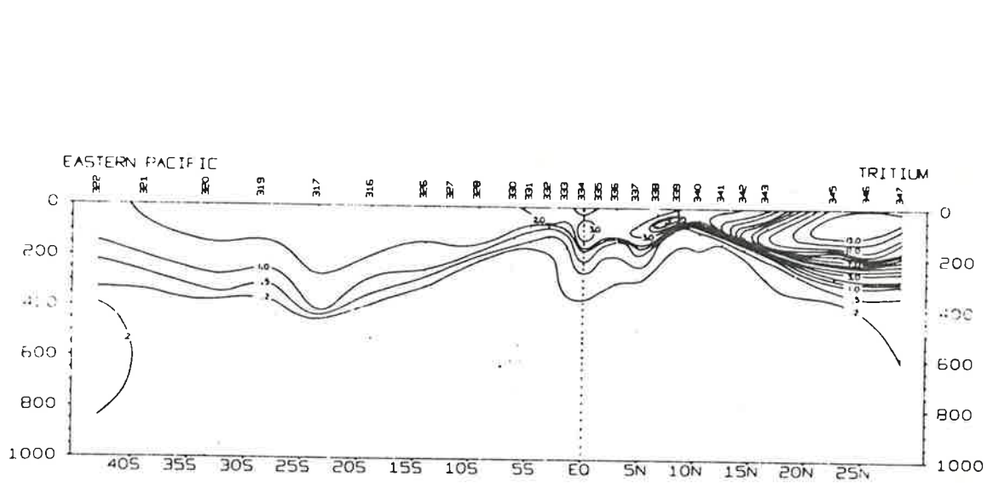

Fig. 6.5c North-south section of tritium in the eastern Pacific (Östlund and Fine, 1979).

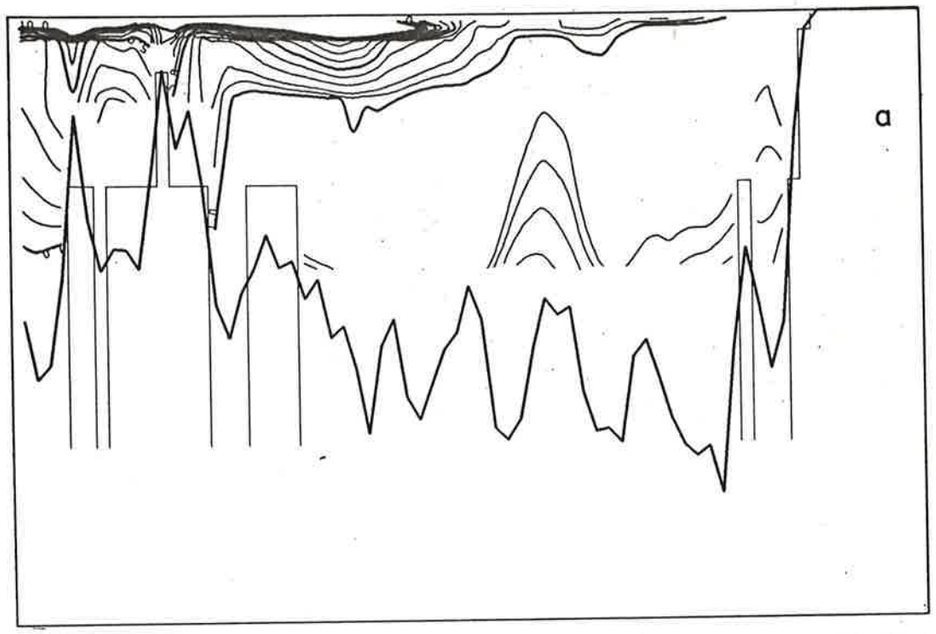

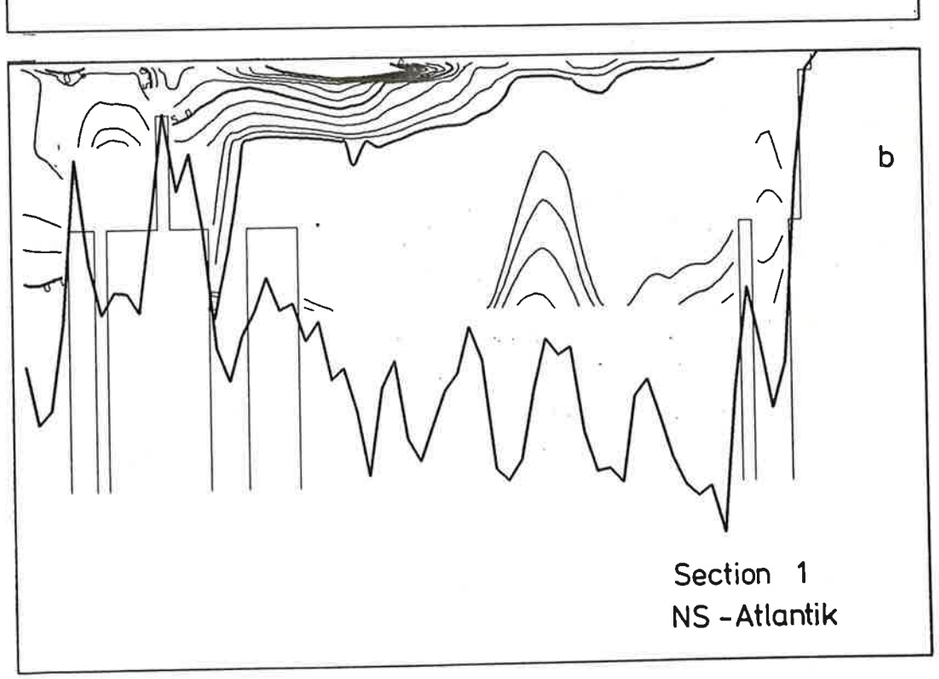

Fig. 6.6a Tritium along section 1 for 1972. Diffusive simulation.

Fig. 6.6b Tritium along section 1 for 1972. Convective simulation.

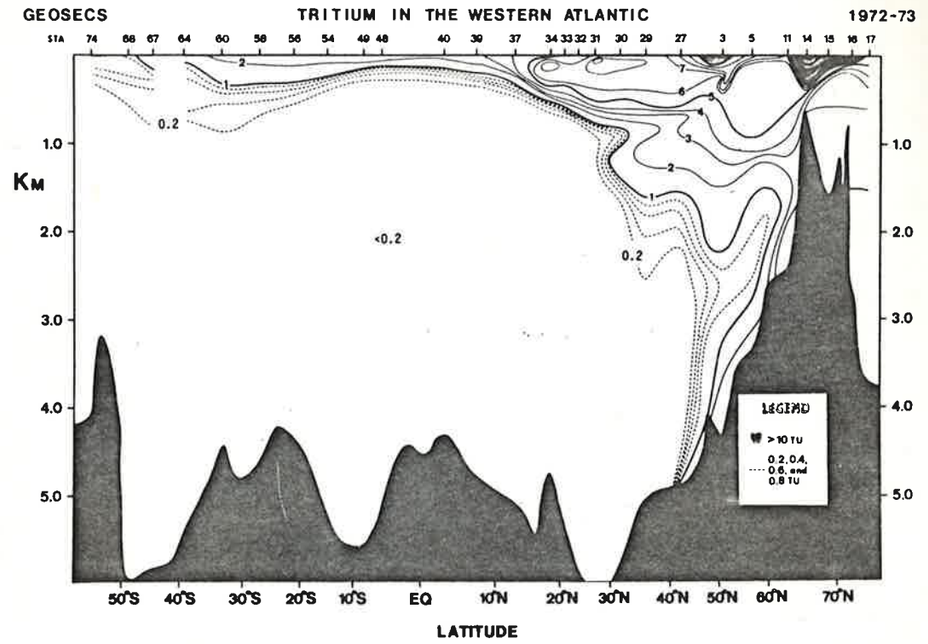

Fig. 6.6c North-south section of tritium in the western Atlantic (Östlund et al., 1976).

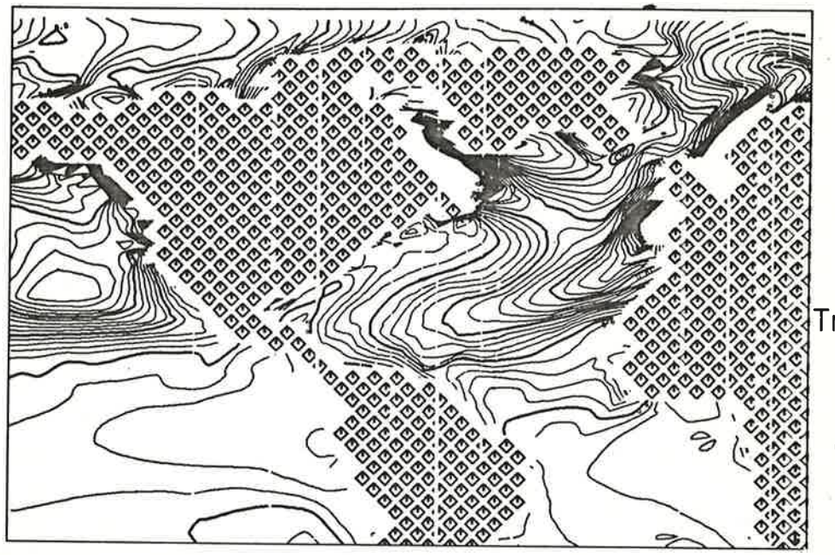

Tritium

75 m

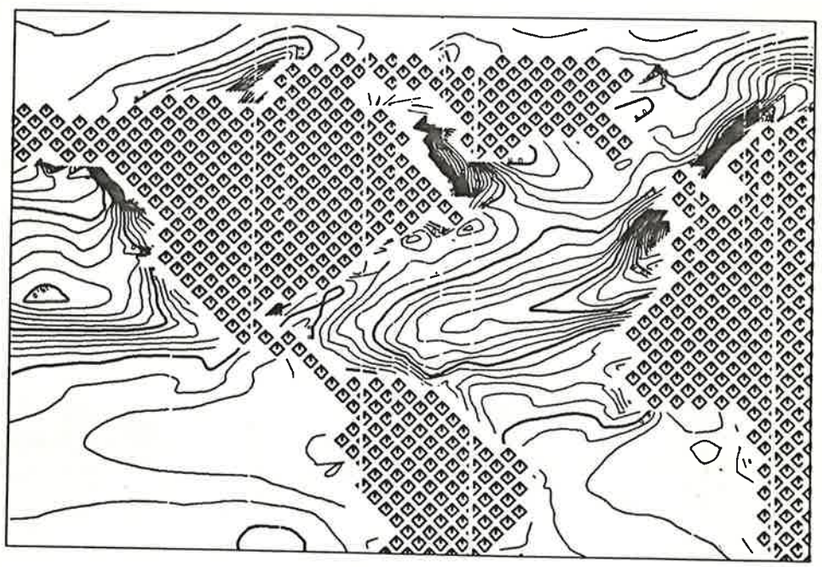

Fig. 6.7a Diffusive (upper panel) and convective (lower panel) simulations at 75 m.

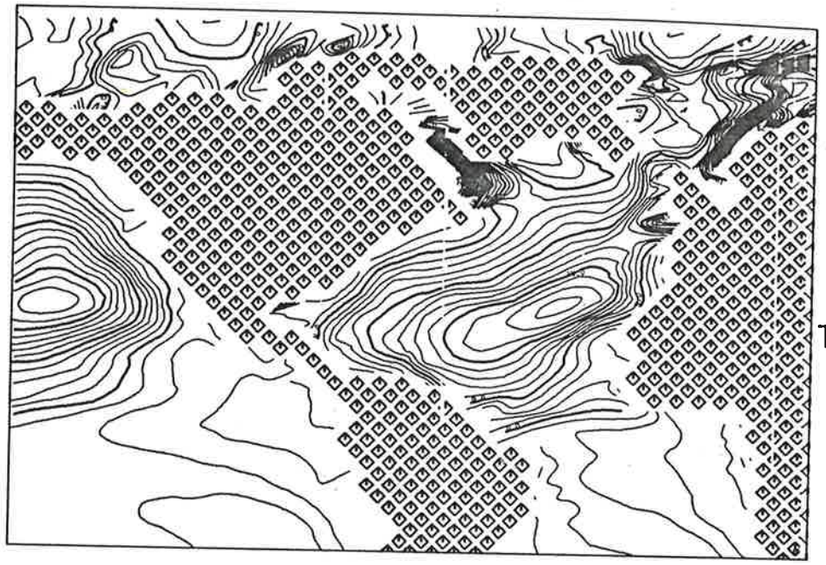

Tritium

150 m

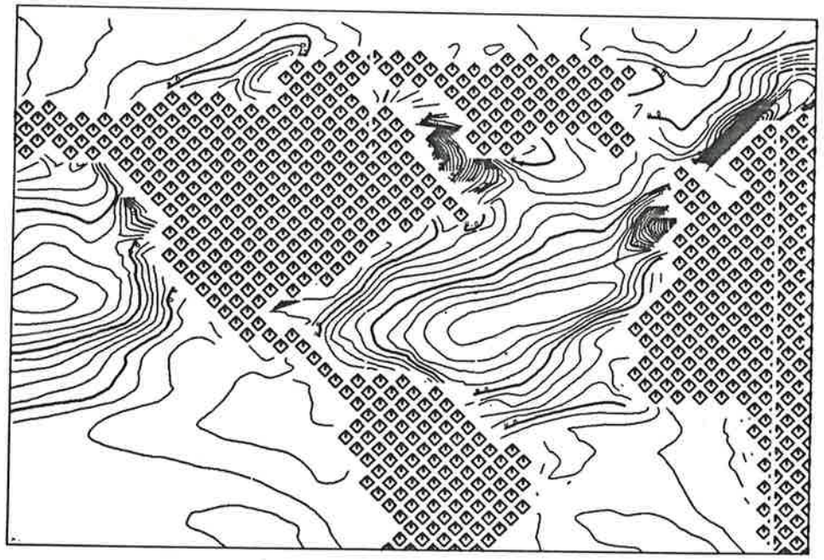

Fig. 6.7b Diffusive (upper panel) and convective (lower panel) simulations at 150 m.

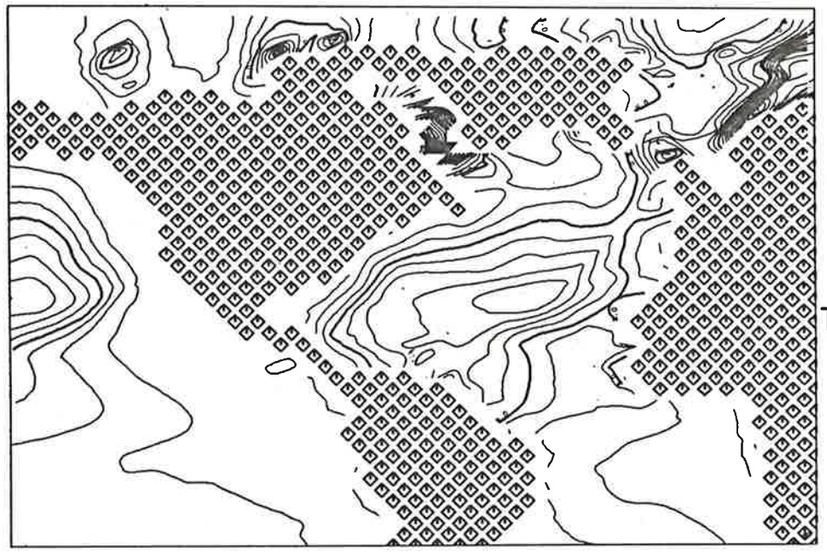

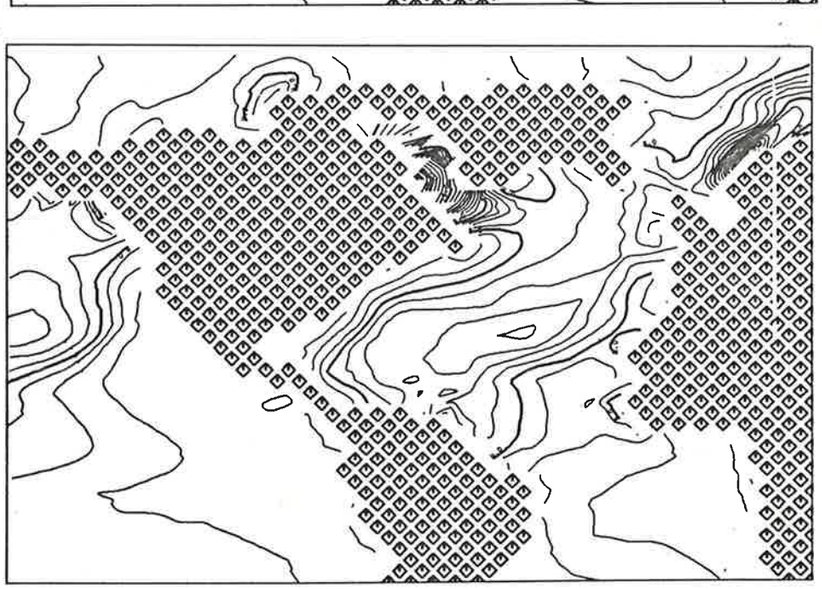

Fig. 6.7c Diffusive (upper panel) and convective (lower panel) simulations at 300 m.

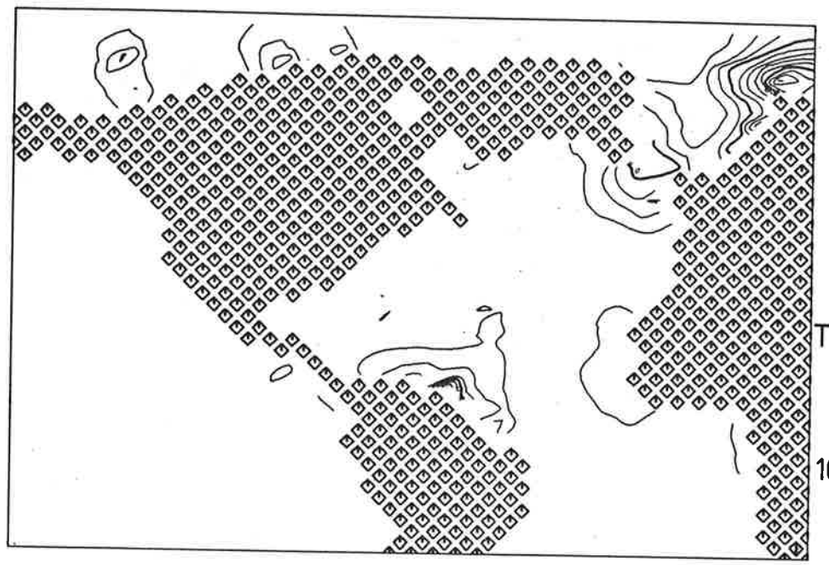

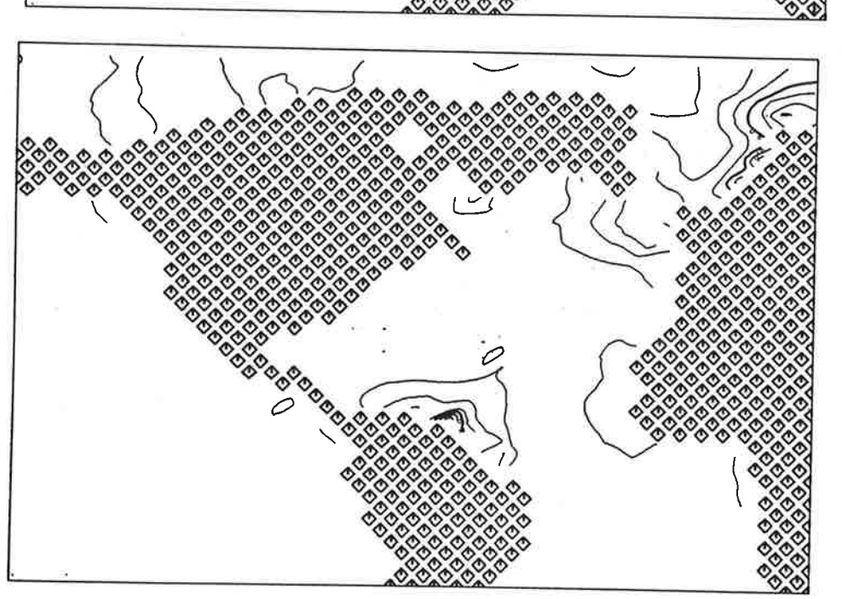

Fig. 6.7d Diffusive (upper panel) and convective (lower panel) simulations at 1000 m.

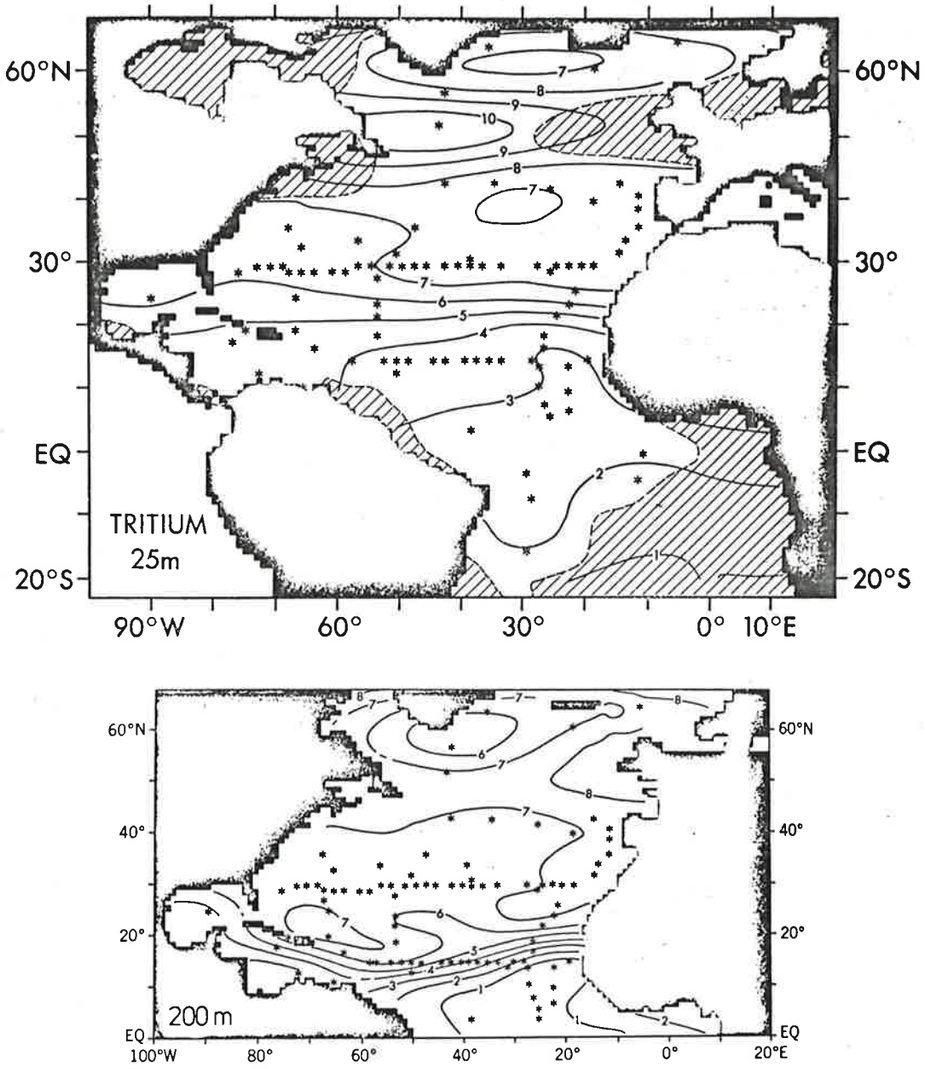

Fig. 6.8a Observed tritium in the North Atlantic at 25 m and 200 m depth (Sarmiento et al., 1982).

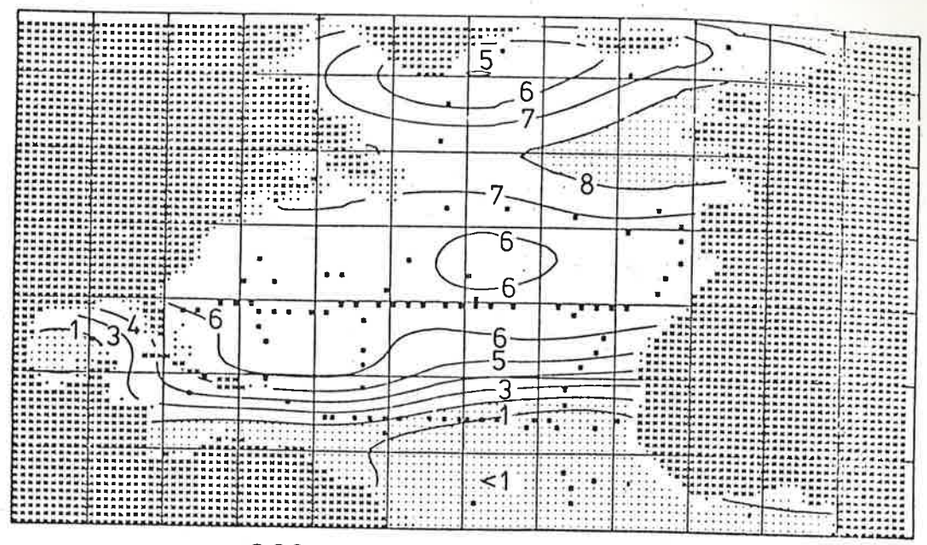

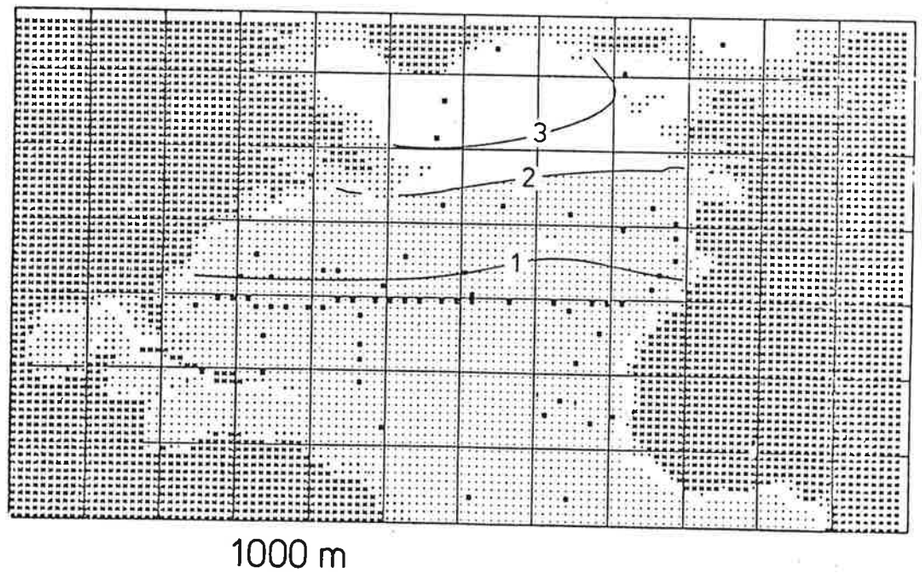

Fig. 6.8b Observed tritium in the North Atlantic at 300 m and 1000 m depth (Sarmiento et al., 1982).

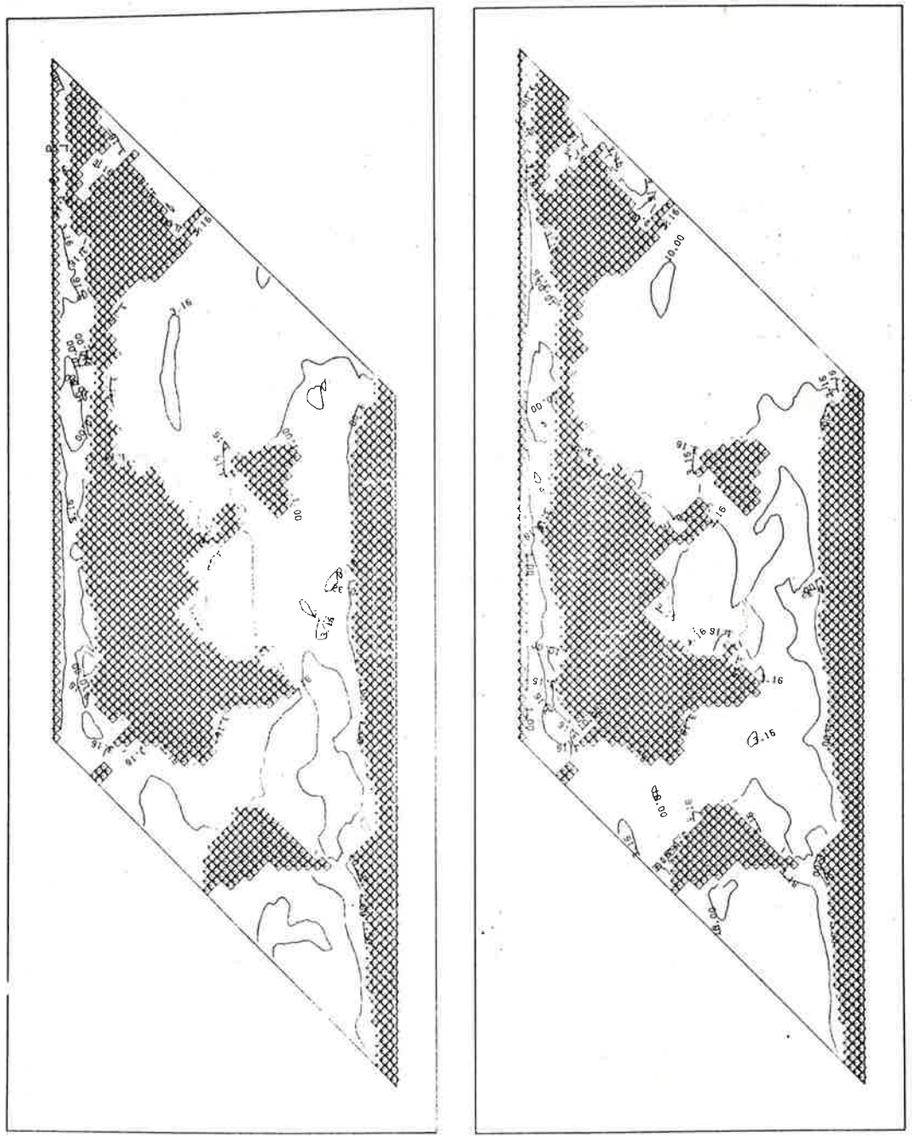

Fig. 6.9a Fraction of ^{14}C in per mille that has been lost due to decay (150 m- and 300 m- level).

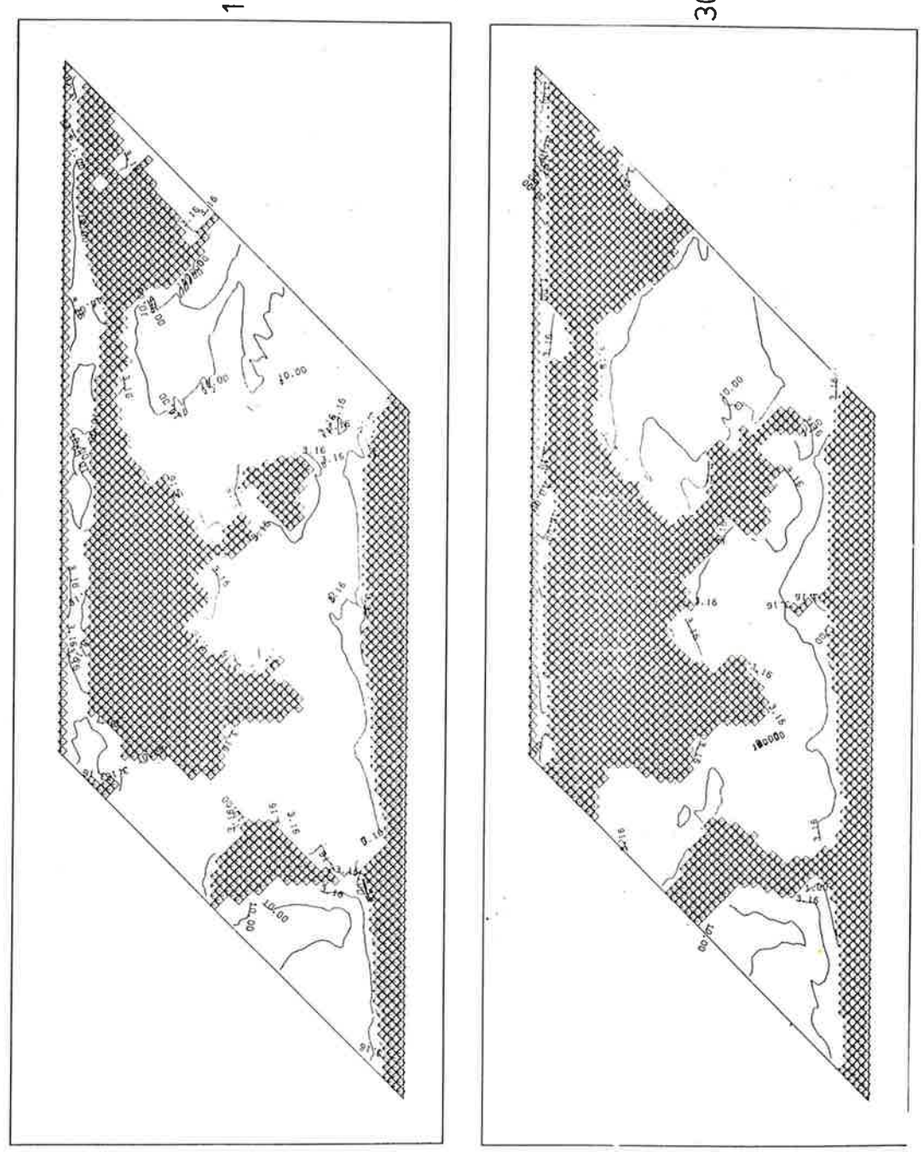

Fig. 6.9b Fraction of ^{14}C in per mille that has been lost due to decay (1000 m- and 3000 m- level).

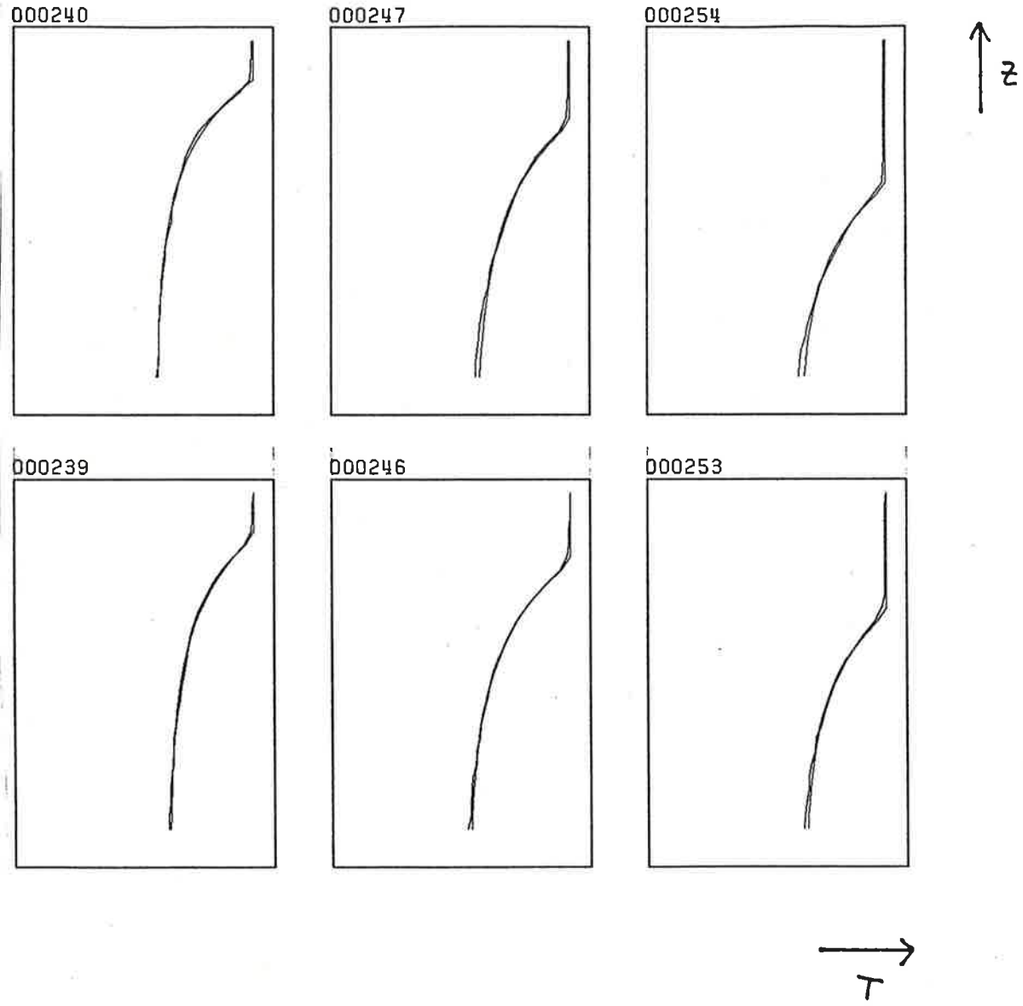

Fig. 7.1 Observed and parameterized temperature profiles from weather station E.

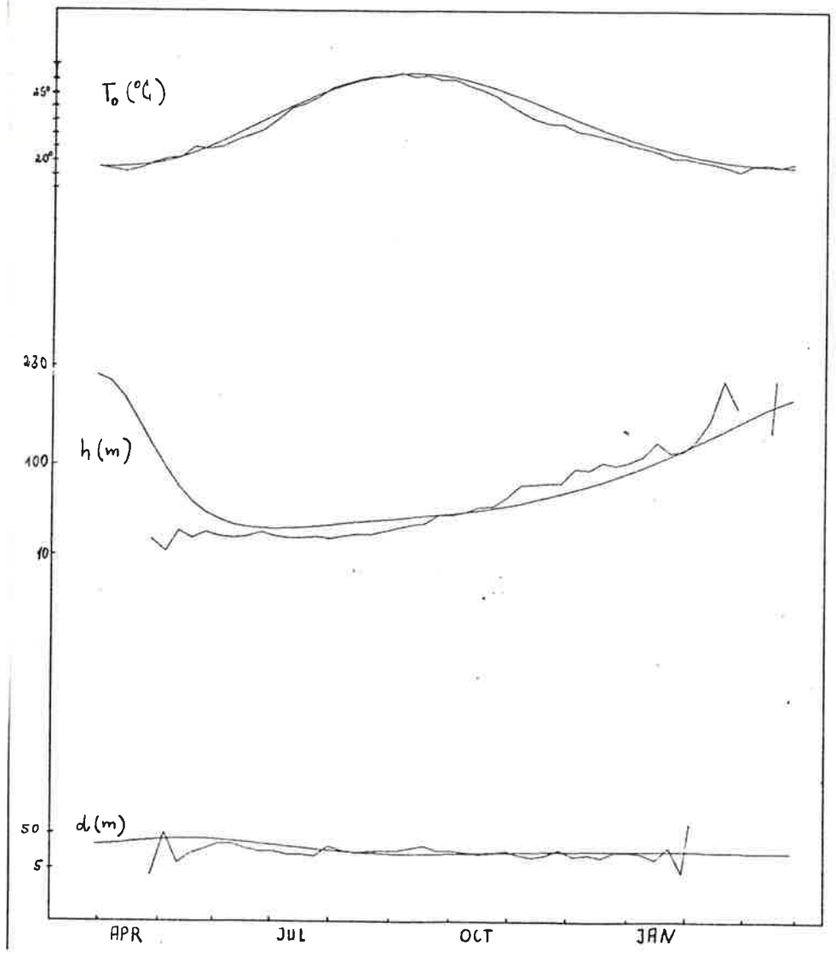

Fig. 7.2 Observed and calculated time series of profile parameters T_o, h and d at weather station E.

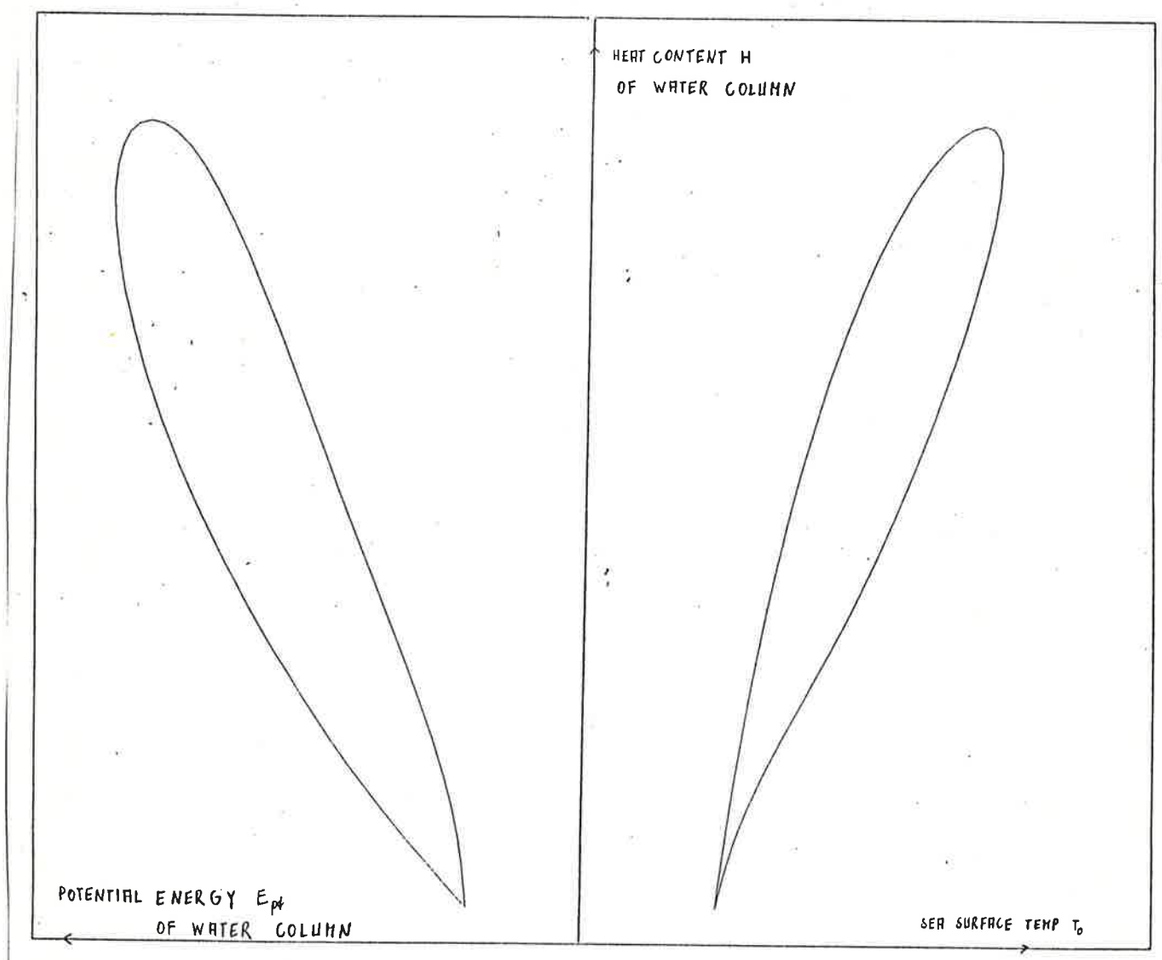

Fig. 7.3 Model heat content H vs. surface temperature T_o and potential energy E_{pt} for one annual cycle.